DISSERTATION

BIOGENIC NANOPARTICLES AND THEIR APPLICATION IN BIOLOGICAL ELECTRON MICROSCOPY

Submitted by

Richard S. Nemeth

Department of Chemistry

In partial fulfillment of the requirements

For the Degree of Doctor of Philosophy

Colorado State University

Fort Collins, Colorado

Summer 2018

Doctoral Committee:

Advisor: Christopher Ackerson

Tingting Yao
Louis Bjostad
Olve Peersen

ABSTRACT

BIOGENIC NANOPARTICLES AND THEIR APPLICATION TO BIOLOGICAL ELECTRON MICROSCOPY

Interest in nanomaterials has seen a dramatic increase over the past twenty years. In recent years many have turned toward proteins to aid in developing novel materials due to the mild reaction conditions, functionalization, and novel synthetic control of the resulting inorganic structures. Proteins have the ability to direct aggregation of inorganic nanostructures, while some enzymes are able to perform oxio/reductase activity to synthesize the materials as well. These two general properties are not always mutually exclusive and the dual function of certain proteins in nanoparticle synthesis is at the core of this work.

Of all the applications for biogenic nanoparticles, generating tools for biological electron microscopy is one of the most appealing. The contrast issue, specifically with *in vivo* biological sample in the electron microscope has drastically limited the information obtainable by this method. An ideal biogenic nanoparticle would operate analogously to GFP in optical microscopy and contain the dual function characteristics stated above. More specifically it would have to fulfill three criteria: i) reduction of a metal precursor, ii) product size control, iii) product retention. To discover such a clonable contrast tag we must deepen our understanding of biogenic nanoparticle formation in tandem with discovering and developing novel dual function enzymes.

This work encapsulates both aspects necessary for the development of a successful clonable nanoparticle for biological electron microscopy. Current biogenic synthetic methods produce nanomaterials with less desirable properties than their inorganic counterparts. Conducting fundamental research and establishing a set of rules and guidelines for biogenic methods will ultimately get us closer to mimicking the control nature has already developed.

This dissertation contains 3 chapters. Chapter 2 focuses on the use of protein crystals as scaffolds for nanomaterial synthesis. Herein porous protein crystals were used to control the gold nanocluster seeded growth of gold nanorods in an attempt to help establish guidelines for biogenic nucleation controlled nanomaterial synthesis. High aspect gold nanorod products were generated from within the crystal pores. Subsequent dissolving of the crystals allowed for release of these rods from their template.

The following two chapters focus on metalloid reductase nanoparticle synthesis in which we have discovered and characterized a novel selenophile bacteria. Through purification and mass spectrometry we found a glutathione reductase like enzyme to be responsible for Se nanoparticle formation. A commercially available glutathione reductase from yeast was used for Se nanoparticle formation *in vitro*. This mechanism was characterized and the system was assessed for potential use as a clonable tag. The native enzyme was sequenced and isolated, followed by its own characterization. Our kinetic findings suggest this enzyme is the first documented metalloid reductase due to its specificity for selenium substrates. The enzymes transportability to foreign organisms demonstrates its potential use as a clonable contrast tag for electron microscopy.

ACKNOWLEDGEMENTS

I have so many people to thank for helping me through this journey to a Ph.D. First and foremost I would like to thank my lovely fiancé Lauren for sticking by my side through this sometimes stressful and difficult time. Your support was so much more crucial for my success than I think you realize. We made it through years of long distance during this time, endured late nights and long shifts, and have been pushed to our limits. I may not know what the future holds, but if we can get through this we can get through anything. I love you.

I must also thank my family for all of the support. I wouldn't have been able to pull this off if you guys hadn't provided me with all of the opportunities through my life. You guys have been great in supporting everything I do and thank you guys for listening to my venting from time to time over the past 5 years.

The most obvious thank you I have is towards the boss man Chris Ackerson. Your hands-off mentorship is THE only reason I have finished out graduate school. I can honestly say I would not have made it through in another lab. I cannot express my appreciation for your patience with me through the years, and bending the lab rules for time with my long distance situation. I have learned how to be a diverse learner from you, how to be a critically thinker, how to actually write (although I still have no idea how you are so good at it), and most importantly how to not let go of the curiosity and excitement for projects when it is so easy to get caught up in getting results. Your mentor strategy has allowed me to think for myself and develop my own projects which will be so much more valuable than anything else in my career. And one last thing, thank you so much for paying my way through the last three years of graduate school. I wouldn't be writing this yet if it wasn't for that and I am extremely grateful.

Thank you to all of my labmates over the years. You guys made work way more manageable and I will miss the days goofing off instead of working. To Thomas Ni thank you for being my lab sensei during my first couple years. To Scott Compel, Marcus Tofanelli, Christain Collins, and Tim Drier you guys helped me learn my way around the lab and made the lab environment what it is today. I will never

forget our cabin adventures. I would also like to thank James, Phillip, Chris, Kanda, Collin, and Ian for helping me over the years, and for all of constructive discussions we have had together. I specifically want to thank Zach Butz for aiding me in my attempts to learn molecular biology and help with every bio based protocol, before you were in the lab and during. Lastly, thank you to my undergrad Mackenzie Neubert for all of the help with the lab tasks no one wants to do for almost half of my time at CSU.

Thank you to Chris Snow and Ann Kowalski for working as a team through one of the most frustrating projects in the history of ever. I can't believe it is almost published. The CSU faculty have been incredible helpful through the years. I would like to thank Patrick McCurdy for the training and help on the SEM. And a special thanks to Roy Geiss for mentoring me on the HRTEM, your skills on that machine are incredible, so thank you for letting me soak up as much as I could over the last two years.

I would like to give a shout out to all of the friends that I have come to know during this time in Colorado, and to those who made the move out here from Minnesota with me. The memories I have of our time together is one of my most priceless processions. Here is to those memories and the ones we have yet to make. And a special shout out to my partner in crime Weston Dockter, may our efforts come to fruition.

Lastly I want to thank my two kitties Toby and Suki for always cheering me up when I get home from a shitty day. And finally to quote a famous philosopher, "Automatic when we, Splatter data in the, 20 double bins up front, Cozza frenzy." I live by this everyday which I take to mean, "Work hard but play harder," and I think that's beautiful.

Richard S. Nemeth

TABLE OF CONTENTS

CHAPTER 1

An Introduction to Protein-Inorganic Materials and Their Application to Biological Electron Microscopy

Over the past two decades nanomaterial research has found an increasingly broad spectrum of applications. These diverse applications range from novel semiconductors[1–3] and catalysts,[4–6] to an array of biomedical tools.[7–9] Current nanomaterials have seen a difficult transfer from academic research to industrial application due to synthetic difficulties.[10,11] Most inorganic nanomaterials require high temperatures and harsh reaction conditions and suffer from poor yields. Such reactions are difficult to scale up past lab bench quantities. Since nanomaterials exist in a realm between bulk and molecular, small changes in their chemical properties tend to have large impacts on their physical characteristics. These properties include; chemical composition, crystal structure, size and surface functionality. Unfortunately controlling these properties is a major pitfall of nanomaterial fabrication since current methods in doing so are extremely limited. In recent years researchers have turned to proteins to aid in solving this dilemma.[10]

The 22 unique amino acids which constitute all proteins provide a diverse and unparalleled display of functional groups, making polypeptides an enticing biomolecule for nanomaterial development. Proteins generally consist of hundreds of amino acids leading to a seemingly endless amount of chemical compositions and properties. For example a protein made from 100 amino acids would have 22^{100} unique amino acid combinations. Proteins can further alter their chemical composition through post-translation modifications of which over 200 are known.[12] Such a vast potential chemical space allows proteins high binding specificity and reactivity, all of which are applicable to metals. Just because proteins have a large potential chemical composition available to them does not mean they are all easily accessible. Fortunately evolution has provided us with a plethora of interesting proteins for nanomaterial development, and we

are able to tailor those proteins to our specific needs using techniques such as mutagenesis,[13] random library generation,[14] and directed evolution.[15]

The idea to apply proteins to inorganic materials can be attributed to earlier research on biomineralization. Research on sea based organisms allowed critical breakthroughs in our understanding of the role that proteins can play in directing biomineralization of inorganic structures. More specifically species which possessed the ability to form SiO_2 structures at ambient conditions.[16] The most popular type of organisms studied are diatoms, a unicellular algae which produce cell walls composed of silica.[17] These organisms have developed the ability to not only conduct biomineralization in mild conditions but form extremely intricate designs from the nanoscale to microscale (Figure 1.1). It also became apparent that these networks were genetically controlled since the patterns and structural details was species specific.[18] Further studies uncovered the biomolecules responsible from biosilification consisted of long-chain polyamines (LCPAs) and proteins (silaffins and silacidins).[19,20] The discovery of these biomineralization pathways sparked interest in applying such avenues to inorganic material formation and an array of metal oxides were successfully templated.[21–23]

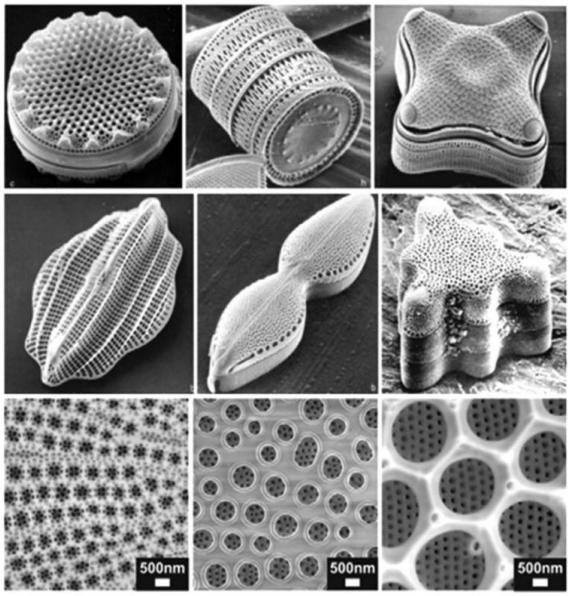

Figure 1.1. SEM images of cleaned diatom silica cell walls (frustules) from several different diatom species, depicting a variety of shapes and patterns created by these organisms.[24]

Proteins isolated from sea organisms initiated the research which evolved into the bio-nanomaterial field we know today, but a myriad of other proteins have been used in material fabrication. Proteins used in such system can serve two overarching functions, (i) templating or (ii) nanostructure synthesis. It should be noted that while it is clarifying to categorize these functions, they are not always exclusive. Templating, or biomineralization, involves the directed aggregation of metal precursors or the reduction of promiscuous salts followed by directed aggregation. Such methods can direct growth of nanostructures leading to more control during synthesis and generating more predictable properties as seen in Figure 1.2.

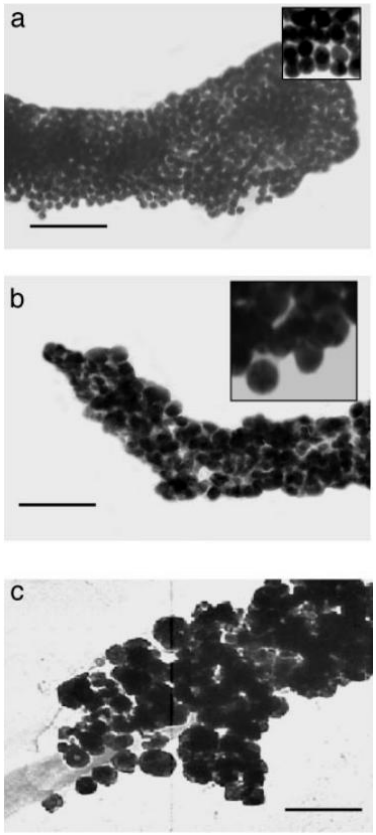

Figure 1.2. TEM images of Cu nanocrystals biomineralized on nanotubes displaying HG12 peptide at pH 6 (a) pH 8 (b) and without HG12 (c).[25]

Nucleation of gold nanoparticles has been controlled in this manner using lysozyme crystals,[26] by restricting gold nanoparticle growth to the crystal pores. Following a similar technique collagen can be formed into fibers structures *in vitro* and has successfully templated mesoporus alumina,[27] TiO_2, and

Fe_x/TiO_2 fibers.[28] Multimer viral capsids are responsible for transporting and protecting viral genomic material. These hollow protein systems have been used to direct nanoparticle formation on their surface with Pt, Ag, and Au.[29,30] Size control of inorganic nanostructures has been demonstrated with many systems and compositions. For example addition of the polypeptide pytochelatin as a surface passivating agent improved monodispersity in CdS quantum dot synthesis,[31] small modifications to a templating peptide altered gold sphere diameters,[32] and tuning peptide conformation conveyed size control over Cu nanocrystals.[25] Outside of size control crystal packing can be influenced by their templates due to the binding residues preference for certain crystal facets.[33]

Proteins that provide synthetic components for nanostructure formation tend to involve an oxio/reductase active site. Nature has provided many examples of this surrounding *in vivo* iron usage. Ferritin and DPS proteins moderate iron levels through enzymatic ferroxidase centers.[34,35] While a host of proteins in magnetotatic bacteria are involved in magnetosome moderation through redox sites.[36] The silicateins identified from sea sponges were found to use an active site serine to catalyst the formation of silica,[37] which was more recently shown to also be responsible for TiO_2 formation.[38] Outside of these native functioning natural proteins the pyridine nucleoside dependent oxioreductases have also shown the ability to enzymatically generate inorganic nanoparticles. The most notably of these enzymes is mercuric reductase,[39] but also includes glutathione reductase, nitrate reductase, and thiodoxin reductase to name a few. This family of enzymes has shown the ability to form a collection of inorganic nanoparticles outside of their designed function.[40–43] These secondary functions have provided an alternate route for catalytic nanomaterial generation.

As stated before proteins involved in these nanomaterial systems have the ability to both generated reactive components, and act as a template for the nanomaterial. Enzymes with this dual function provide an alluring starting point for potential applications such as bio-imaging, and more specifically biological electron microscopy. Biological electron microscopy suffers from what is commonly known as the contrast issue. Electron microscopy (EM) methods generate images based on the samples interactions with the electron beam. As your sample increases in atomic weight the more it will

interact with the beam. Unfortunately biological samples are all made of the same "light" elements and all details are completely lost. Such low sample signal can be overcome by extended measurement times or increased beam intensity, but beam damage to biological samples happens almost immediately with 15 to 40% of sample massing being lost in the first 30 seconds.[44] This lack of contrast limited results from biological EM to only resolving cellular super structures such as cell walls. More recent advancements in cryo sample preparation has increased biological sample stability.[45] This, paired with technological advancements, has drastically increased the efficacy of biological EM. This is clearly seen with the explosion of the single particle cryo EM field. Such techniques have been used to solve thousands of biological structures *in vitro*.[46] Even with all of the recent advancements, the field is still limited to resolving *in vitro* samples. To this day the contrast issue still plagues *in vivo* samples.[47]

Over the years a large effort has been put toward solving this issue with limited success. Heavy metal staining is a common practice to help elucidate major ultrastructures but has limited specificity (Figure 1.3).[48] Another common technique was developed using gold labeled antibodies. This is known as immunolabeling and has shown success in the literature for a range of proteins.[49–51] Unfortunately there are a limited number of antibody targets known and their size only allows binding on the sample surface.[52]

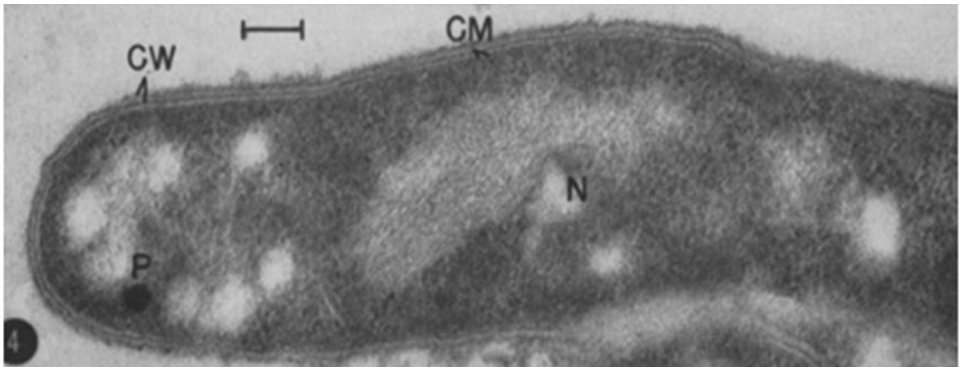

Figure 1.3. Thin section of *Mycobacterium* Jucho strain stained with osmium tetroxide, fixed and treated with unranyl-acetate, and embedded in araldite. The cell wall (CW), cytoplasmic membrane (CM), polyphosphate granuale (P), and nuclear apparatus (N) are highlited.[48]

A proposed improvement to these techniques and a solution to the contrast issue as a whole would involve an *in situ* clonable tag analogous to the green fluorescent protein (GFP) used in optical microscopy. Various polypeptides have been assessed for this task including ferritin, metallothionein, and proteins from magnetotatic bacteria. Ferritin has shown some success as a clonable tag,[34] but only functions as a 24mer totaling around .45 MDa which has severely limited its usefulness.[53] Metallothionein requires stoichiometric amounts of gold salts which again lead to a very large tag and high background noise.[54] Studies have shown that genes from magnetotatic bacteria must work synergistically to form iron oxide particles and membrane encapsulation is inevitable with products averaging 100 nm.[55] It is apparent that all of the current *in situ* clonable tags are much too large to be successful in biological EM.

Such a tag must fulfill 3 main requirements: i) reduction of a metal precursor, ii) product size control, iii) product retention. All assessed systems to this point have failed at least one of these criteria. Collectively these specifications are the culmination of the current protein-nanomaterial field. The ideal tag must have controlled biomineralization and must harness the ability to synthesize the nanoparticle.

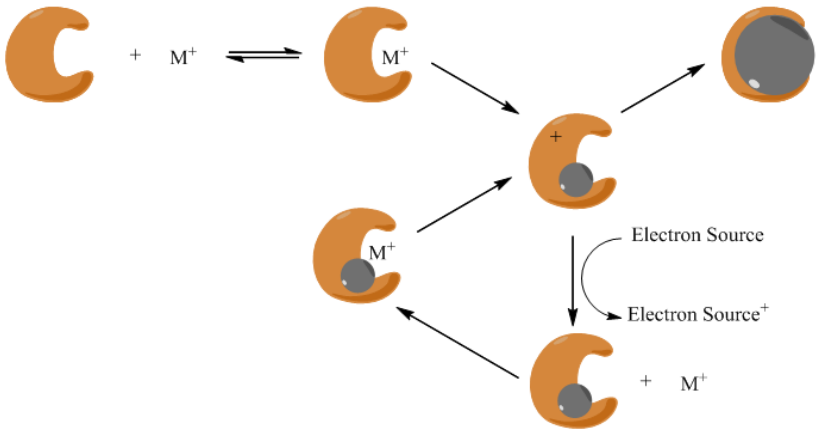

Figure 1.4. Schematic for an ideal clonable tag for biological electron microscopy.

At its current state, the biogenic nanomaterial field has provided alternative synthesis strategies for nanomaterials under mild conditions which could eventually be scaled to an industrial setting.[10] But at this time strictly inorganic routes allow for increased synthetic control leading to higher quality products with more desirable properties than their biogenic counterparts. Proteins provide an unprecedented chemical space which can supply endless surface functionalities and 3D structures, while providing tunable specificity and reactivity. Synthetic control of any regime of nano science remains a challenge and the current methodologies regarding protein-inorganic hybrids are severely limited. Furthering our understanding of how proteins manipulate nanostructure formation is crucial for the development of nanoscale applications. With minor alterations at the atomic level causing such major transformations on the macro scale our control must be more precise than ever before. A deepened understating of this field may provide a solution to the underlying problems with biological electron microscopy. There have been many attempts to solve the contrast issue but it is apparent that our lack of control in biogenic nanoparticle formation is limiting our success. Apart from furthering our understanding of biogenic controlled nanoparticle formation we must also search for novel proteins which can fulfill the three criteria necessary for a functioning clonable nanoparticle. A successful clonable tag will most likely be derived from a naturally occurring protein. Thus we must begin to understand what makes a polypeptide advantageous through the characterization and analysis of any potential candidates.

REFERENCES

1. Nie, Z., Petukhova, A. & Kumacheva, E. *Nat. Nanotechnol.* **2010,** *5,* 15–25.

2. Whaley, S. R., English, D. S., Hu, E. L., Barbara, P. F. & Belcher, A. M. *Nature* **2000,** *405,* 665–668.

3. Li, L.-L., Cui, Y.-H., Chen, J.-J. & Yu, H.-Q. *Front. Environ. Sci. Eng.* **2017,** *11,* 7.

4. Hrapovic, S., Liu, Y., Male, K. B. & Luong, J. H. T. *Anal. Chem.* **2004,** *76,* 1083–1088.

5. Mauter, M. S. & Elimelech, M. *Environ. Sci. Technol.* **2008,** *42,* 5843–5859.

6. Gopidas, K. R., Whitesell, J. K. & Fox, M. A. *Nano Lett.* **2003,** *3,* 1757–1760.

7. Cheng, Y. *et al*. *J. Am. Chem. Soc.* **2008,** *130,* 10643–10647.

8. Souza, G. R. *et al. Proc. Natl. Acad. Sci.* **2006,** *103,* 1215–1220.

9. Luo, Z., Zheng, K. & Xie, J. *Chem. Commun.* **2014,** *50,* 5143–5155.

10. Krajina, B. A., Proctor, A. C., Schoen, A. P., Spakowitz, A. J. & Heilshorn, S. C. *Prog. Mater. Sci.* **2018,** *91,* 1–23.

11. Yoon Hyeonseok & Jang Jyongsik. *Adv. Funct. Mater.* **2009,** *19,* 1567–1576.

12. Duan, G. & Walther, D. *PLOS Comput. Biol.* **2015,** *11,* e1004049.

13. Liu, H. & Naismith, J. H. *BMC Biotechnol.* **2008,** *8,* 91.

14. Wilson David S. & Keefe Anthony D. *Curr. Protoc. Mol. Biol.* **2001,** *51,* 8.3.1-8.3.9.

15. Troll, C., Alexander, D., Allen, J., Marquette, J. & Camps, M. *J. Vis. Exp. JoVE* **2011,** *49,* e2505.

16. Brandstadt, K. F. *Curr. Opin. Biotechnol.* **2005,** *16,* 393–397.

17. Bauerlein, E. Biomineralization: Progress in Biology, Molecular Biology and Application, 2nd, Completely Revised and Extended Edition. **2006**

18. Bauerlein, E. Handbook of Biomineralization: Biological Aspects and Structure Formation. **2008.**

19. Sumper, M. & Kröger, N. *J. Mater. Chem.* **2005,** *14,* 2059–2065.

20. Hildebrand, M. *Chem. Rev.* **2008,** *108,* 4855–4874.

21. Sumerel, J. L. *et al. Chem. Mater.* **2003,** *15,* 4804–4809.

22. Kisailus, D., Truong, Q., Amemiya, Y., Weaver, J. C. & Morse, D. E. *Proc. Natl. Acad. Sci.* **2006,** *103,* 5652–5657.

23. Dai, H. *et al. J. Am. Chem. Soc.* **2005,** *127,* 15637–15643.

24. Kröger, N. *Curr. Opin. Chem. Biol.* **2007,** *11,* 662–669.

25. Banerjee, I. A., Yu, L. & Matsui, H. *Proc. Natl. Acad. Sci.* **2003,** *100,* 14678–14682.

26. Wei, H. *et al. Nat. Nanotechnol.* **2011,** *6,* 93–97.

27. Deng, D., Tang, R., Liao, X. & Shi, B. *Langmuir* **2008,** *24,* 368–370.

28. Cai, L., Liao, X. & Shi, B. *Ind. Eng. Chem. Res.* **2010,** *49,* 3194–3199.

29. Dujardin, E., Peet, C., Stubbs, G., Culver, J. N. & Mann, S. *Nano Lett.* **2003,** *3***,** 413–417.

30. Slocik, J. M., Naik, R. R., Stone, M. O. & Wright, D. W. *J. Mater. Chem.* **2005,** *15,* 749–753.

31. Bae, W. & Mehra, R. K. *J. Inorg. Biochem.* **1998,** *69,* 33–43.

32. Hwang Leekyoung, Zhao Gongpu, Zhang Peijun & Rosi Nathaniel L. *Small* **2011,** *7,* 1938–1938.

33. Kim, J. K. *et al. Chem. Commun.* **2014,** *50,* 12392–12395.

34. Wang, Q., Mercogliano, C. P. & Löwe, J. *Struct. Lond. Engl.* **2011,** *19,* 147–154.

35. Castruita, M. *et al. Appl. Environ. Microbiol.* **2006,** *72,* 2918–2924.

36. Raschdorf Oliver, Müller Frank D., Pósfai Mihály, Plitzko Jürgen M. & Schüler Dirk. *Mol. Microbiol.* **2013,** *89,* 872–886.

37. Brutchey, R. L. & Morse, D. E. *Chem. Rev.* **2008,** *108,* 4915–4934.

38. P. Smith, G., J. Baustian, K., J. Ackerson, C. & L. Feldheim, D. *J. Mater. Chem.* **2009,** *19,* 8299–8306.

39. Lian, P. *et al. Biochemistry (Mosc.)* **2014,** *53,* 7211–7222.

40. Li, X. & Krumholz, L. R. *J. Bacteriol.* **2009,** *191,* 4924–4933.

41. Freedman, Z., Zhu, C. & Barkay, T. *Appl. Environ. Microbiol.* **2012,** *78,* 6568–6575.

42. Pugin, B. *et al. Appl. Environ. Microbiol.***2014,** *80,* 7061–7070.

43. Otwell, A. E. *et al. Environ. Microbiol.* **2015,** *17,* 1977–1990.

44. Thach, R. E. & Thach, S. S. *Biophys. J.* **1971,** *11,* 204–210.

45. Ruiz, T., Erk, I. & Lepault, J. *Biol. Cell* **1994,** *80,* 203–210.

46. Doerr, A. Single-particle cryo-electron microscopy. *Nature Methods*. **2016,** *13,* 23.

47. Wang, H. *Sci. China Life Sci.* **2015,** *58,* 750–756.

48. Koike, M. & Takeya, K. *J. Biophys. Biochem. Cytol.* **1961,** *9,* 597–608.

49. Hayat, M. A. *Micron Microsc. Acta* **1992,** *23,* 1–16.

50. Romano, E. L. & Romano, M. *Immunochemistry* **1977,** *14,* 711–715.

51. Pettitt, J. M. & Humphris, D. C. *Histochem. J.* **1991,** *23,* 29–37.

52. McIntosh, R., Nicastro, D. & Mastronarde, D. *Trends Cell Biol.* **2005,** *15,* 43–51.

53. Theil, E. C. *Annu. Rev. Biochem.* **1987,** *56,* 289–315.

54. Diestra, E., Fontana, J., Guichard, P., Marco, S. & Risco, C. *J. Struct. Biol.* **2009,** *165,* 157–168.

55. Kolinko, I. *et al. Nat. Nanotechnol.* **2014,** *9,* 193–197.

CHAPTER 2

Protein Crystals as Molds for Seeded Gold Nanorod Growth*

2.1 Synopsis

Precise and programmable bottom-up synthesis of inorganic nanoparticles represents a grand challenge of inorganic materials synthesis. Such structures applied to nanomedicine, electronics, photonics, imaging, and sensing. Here we show that a protein crystal can serve as a scaffold to direct the growth of high aspect ratio gold nanorods. Nanorod growth is further controlled by the presence of pre-defined nucleation points within the crystal. The resulting structures can be released from the protein matrix.

2.2 Introduction

A grand challenge in inorganic nanoparticle synthesis is the production of asymmetric 3D nanoparticles.[1] These particles have many applications in sensors, solar cells, biological imaging, electronics, energy storage devices, and cancer therapies.[2–7] High-aspect ratio nanorods and other low-symmetry particles attract interest for their anisotropic optical properties.[7,8] However, these particles are more difficult to synthesize homogenously, economically, and in bulk.[9] Solution phase synthesis can produce a variety of nanoparticle shapes[10] and nanorods with aspect ratios up to ~50.[11,12] Still, solution phase synthesis often requires trial and error searches for reaction conditions that produce the desired nanoparticle shape, and product polydispersity is a challenge.[13–15] Lithographic approaches can fabricate arbitrary shapes in 2D and in a limited way in 3D, but 'top-down' approaches are limited in the quantity of material that can be produced when compared to 'bottom-up' approaches.[16,17]

The work presented herein is to be published in ACS NANO. Richard S. Nemeth's contributions to this work include experimental design, data analysis, synthetic development and characterization of gold nanorods used in this study.

Templated synthesis is a promising approach to retain more control over nanoparticle shapes in three dimensions. Proteins in particular are an attractive template for the growth and placement of nanoparticles.[18,19] Recently researchers have synthesized nanoparticles within a variety of scaffolds. For example, several groups have grown gold nanoparticles within lysozyme crystals[20–22], while others have used viruses[23] and functionalized protein cages[24–26] to produce a variety of nanostructures.[27] As researchers gain the ability to control protein assembly topology,[28–31] limitless programmed or designed template morphologies can be imagined. Protein crystals can be highly solvent accessible and contain hundreds of millions of identical pores, allowing for extremely parallel growth of anisotropic nanostructures.

Here we show that protein crystals can serve as scaffolds to grow high aspect ratio gold nanorods. We have previously immobilized 25-atom gold clusters within the pores of a protein crystal.[32] Now, these clusters serve as nucleation sites for the controlled growth of gold nanorods. We show that, under certain conditions, growth can be dependent on the presence of seeds, and that the method can be expanded to other scaffolds. By nucleating growth on pre-defined seeds, we separate nucleation and growth, allowing greater control over the growth of metal nanostructures.

2.3 Results and Discussion

The scaffold protein crystal was selected in a systematic, automated screen of the Protein Data Bank for protein crystals with large solvent channels. The crystal selected from the database is composed of a single protein, CJ0 (Fig. 1) (Genebank ID: cj0420, Protein Data Bank code: 2fgs). CJ0 is a putative periplasmic polyisoprenoid-binding protein from *Campylobacter jejuni*. The vector encoding CJ0 was obtained from the Protein Structure Initiative's Biology-Materials Repository.

The protein was expressed and purified as described previously.[32] Crystals were grown in ammonium sulfate buffer at pH 6.5 and subsequently crosslinked by direct addition of 100 mM 1-Ethyl-3- (3-dimethylaminopropyl) carbodiimide (EDC) and 50 mM imidazole. The crosslinking reaction was quenched after 1 hour via addition of 50 mM sodium borate at pH 10.0.

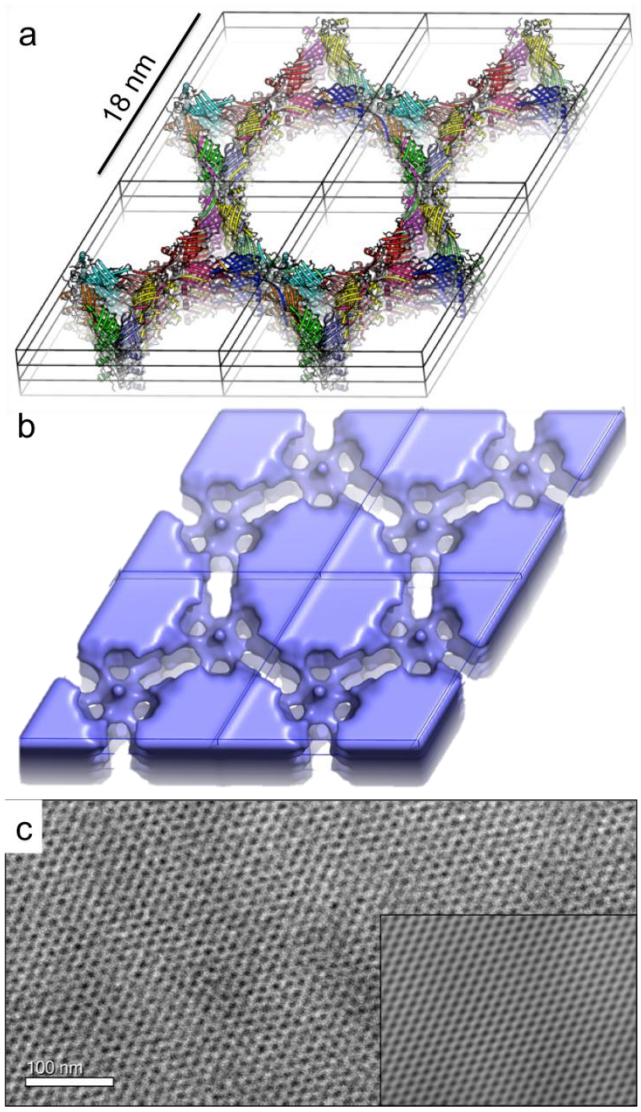

Figure 2.1. (a) Top-view Pymol schematic of several unit cells of CJ protein crystal, showing ~13 nm diameter cylindrical pores. **(b)** Solvent channels (Chapter 5.1.36- 5.1.37). **(c)** TEM micrograph of a thin section of a CJ crystal reveals repeating axial pore structure depicted in (a). Inset: FFT-simulated image obtained from the micrograph in (c).

Crosslinked CJ crystals absorb Au_{25} clusters with glutathione and nitrilotriacetic acid ligands ($Au_{25}(GSH)_{17}(NTA)$) by a shared affinity for Ni(II) between the NTA and scaffold Histidine tag, as described previously.[32] These gold clusters then serve as nucleation sites for controlled gold growth once the crystal is placed in a growth solution consisting of polyvinylpyrrolidone (PVP), potassium iodide (KI), chloroauric acid ($HAuCl_4$), and ascorbic acid. As previously shown,[33] KI and PVP can act as coordinating and capping ligands, respectively. PVP and KI limit the auto-nucleation of particles, a well-known issue for $HAuCl_4$ in the presence of protein.[34,35] Growth occurs over 10 minutes (Fig. 2).

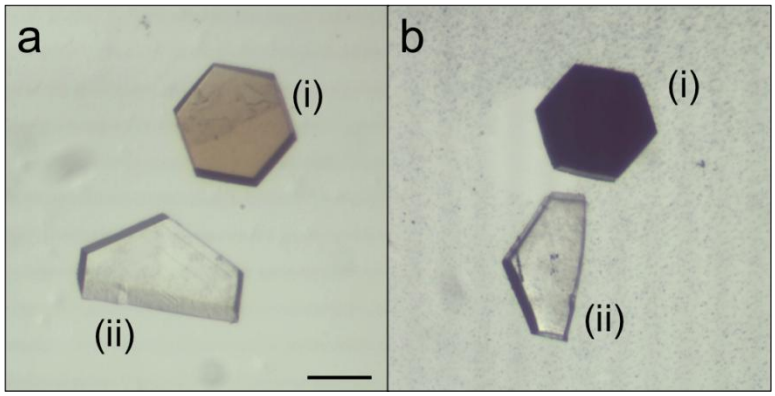

Figure 2.2. CJ crystals with (i) and without (ii) $Au_{25}(GSH)_{17}NTA$ seeds, in the gold growth solution consisting of PVP, KI, $HAuCl_4$, and ascorbic acid at (a) t = 0 and (b) t = 10 mins. Scale bar is 100 um.

The resulting gold structures could be released from crystals for downstream applications and analysis. Crystals were dissolved in 0.5 M NaOH at 35^{o}C overnight (Chapter 5.1). Transmission electron microscopy (TEM) images of the dissolved crystals from Figure 2.1 show the gold structures present in the sample (Chapter 5.1.14).

Gold growth also occurred within the crystals using a variety of alternative gold precursors and reducing agents (Chapter 5.1.1-5.1.13 and Chapter 5.1.16). The protocol that resulted in synthesis (and recovery) of the highest aspect ratio gold nanorods, shown in Fig. 3, was to soak seeded crystals in 10 mM $HAuCl_4$ for 10 mins, then transfer the crystals to a drop of 10 mM ascorbic acid for 1 hr, at which point the crystals were black by eye (Figure 5.1.1). Notably, this protocol did not require the presence of seed particles; the high reduction potential of $HAuCl_4$ causes self-nucleation, aided by ascorbic acid and the reducing amino acids in the crystal.[36–38] However, we determined by TEM and elemental analysis that allowing gold nanoparticle seeds to adsorb within the crystal before growing the rods led to significantly higher overall growth within the pores (~700 versus ~200 gold atoms per unit cell of the crystal, as determined by ICP-MS elemental analysis). Still, with the seeded growth method, elemental analysis indicated about 10% gold content with respect to the theoretical maximum.[32]

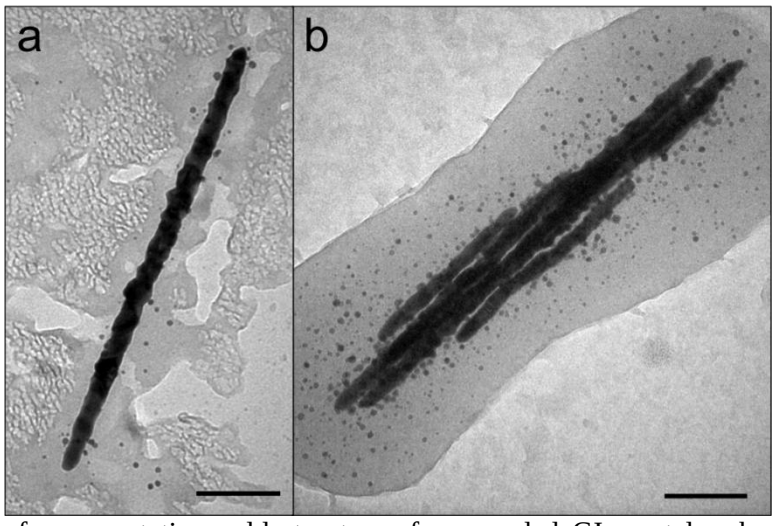

Figure 2.3. TEM of representative gold structures from seeded CJ crystals when grown in 10 mM $HAuCl_4$ for 10 mins, transferred to a drop of 10 mM ascorbic acid for 1 hr, and then dissolved. Scale bars are 100 nm. See Chapter 5.1.1-5.1.16 for additional examples of structures resulting from this and alternative growth methods.

To further demonstrate scaffold-limited gold growth, we recapitulated crystal growth experiments using a pyridine nucleotide-disulfide family oxidoreductase from *E. faecalis* (PDB entry 3oc4). These later crystals have 5 and 9 nm cylindrical pores (Figure 5.1.20).

To confirm growth occurred within the crystal, we attempted to image the gold structures while still encapsulated within the protein (Chapter 5.1.30-5.1.32). Figure 2.4 suggests gold structures embedded within partially dissolved or crushed 3oc4 and CJ crystals. In Figure 2.4 (a) and (c) we see parallel streaks of high electron density embedded within a lower electron density matrix indicative of the presence of anisotropic gold structures within partially dissolved crystals. In Figure 2.4 (b), the arrow indicates a 20 nm diameter nanorod of high electron density, which has been sheared radially at the exposed end, potentially during the liquid N_2 freezing and crushing process.

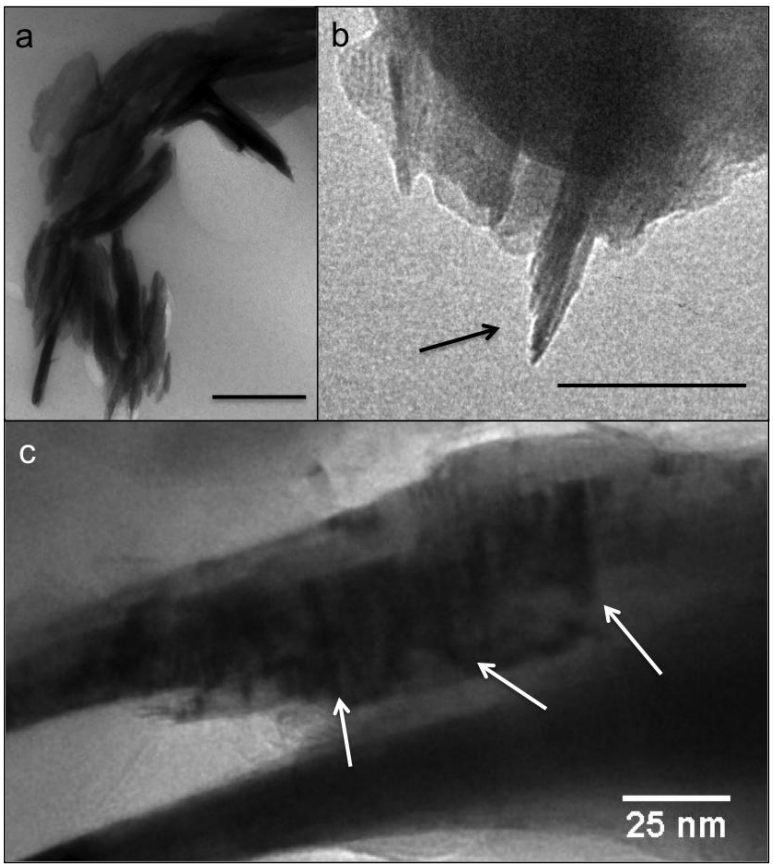

Figure 2.4. TEM of *in situ* rods embedded within (a) partially dissolved CJ crystals, (b) liquid N_2 shattered CJ crystals and (c) partially dissolved 3oc4 crystals. Top scale bars are 100 nm.

Somewhat surprisingly, typical nanorods (Fig. 3) grown within CJ crystals had an average diameter of 20.2 ± 4.7 nm. The maximum length of rods recovered from dissolved crystals was 870 nm (Chapter 5.1.21-5.1.23). Rods from 3oc4 crystals were typically ~5nm in diameter. We hypothesize that typical rods were slightly larger in diameter than the pores of the crystal, because the protein could be displaced outward during rod growth (Chapter 5.1.21-5.1.23).

Rods released from crystals were further analyzed by high-resolution transmission electron microscopy and by 3-D electron tomography. High-resolution electron microscopy revealed atomic columns of Au within the nanorods, as well as the size, shape and orientation of crystallites within the nanorods (Fig. 5). Systematic analysis of the crystallite size, orientation and periodicity within rods did not reveal any clear patterns. For instance, we did not observe periodicity conforming to the 5 nm height of the crystal unit-cell or lattices that may extend the icosahedral core of the seed particles. Electron

diffraction (Fig. 5) revealed only the presence of fcc (bulk-phase) Au. Lack of extended periodic patterns within the rods (seen in the electron diffraction data in Fig. 5) is in accord with these results.

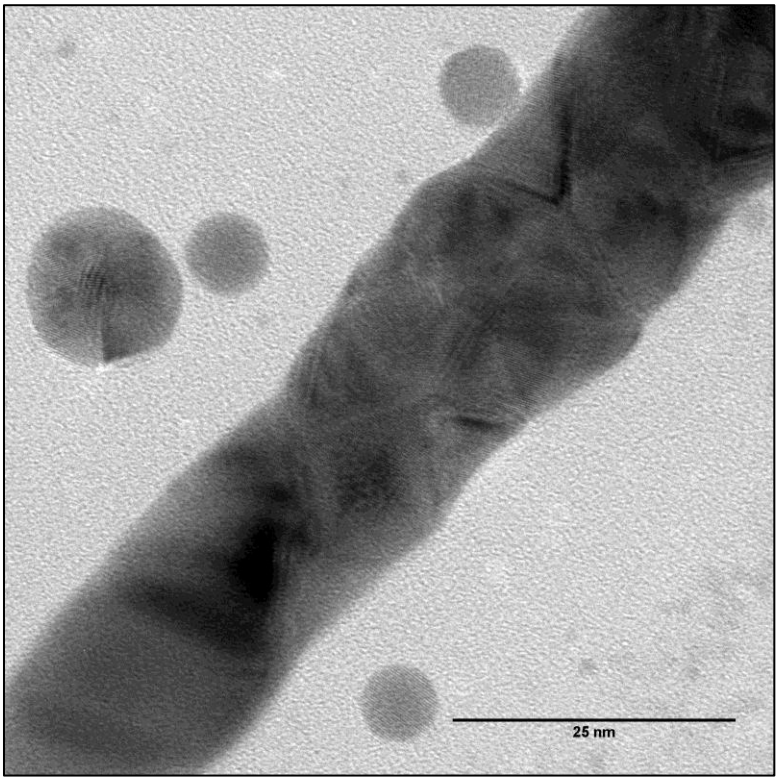

Figure 2.5. HR-TEM of gold nanorod released from CJ crystal scaffold. Scale bar is 25 nm.

We observed in some cases discrete rods and in other cases bundles of rods. In cases where we observe bundles of rods, the rods appeared to be connected by short bridging segments. These may arise from the smaller lateral solvent channels in the crystals. We collected tilt-series of rod bundles to produce tomographic reconstructions assembled in IMOD / 3DEM[39] to generate 3D models of the rod bundles (Fig. 6, Fig. 5.1.29). The 3-D models confirmed that the observed rod interconnects between rods arose from lateral junctions consistent with the lateral solvent channels found in the template crystal (Fig. 1b), and not, for instance, from superimposed perpendicular rods.

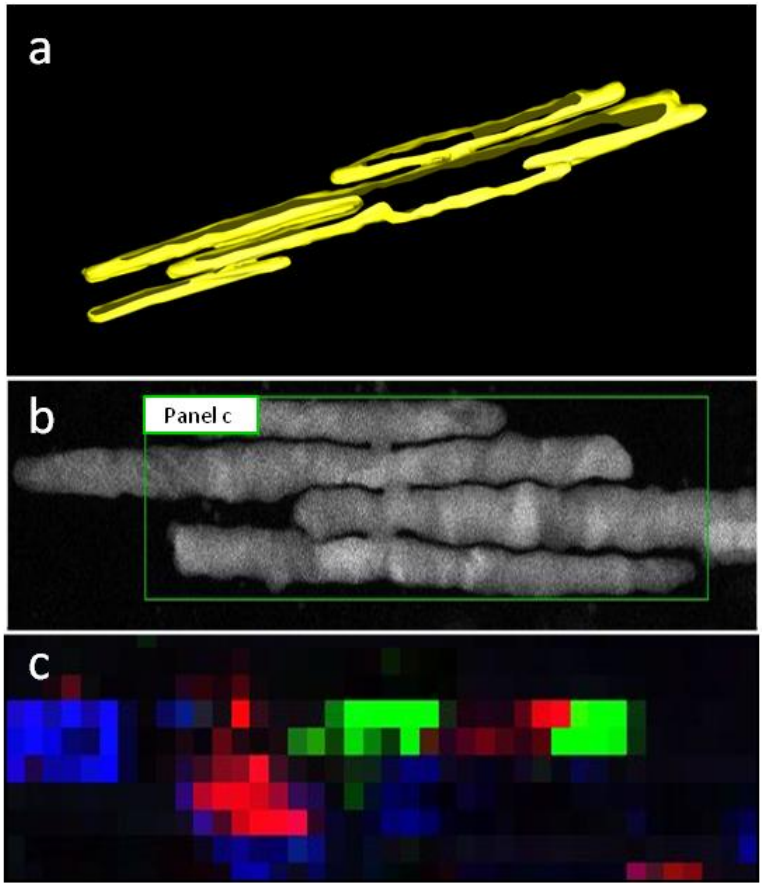

Figure 2.6. (a) Tomographic reconstruction of nanorod bundle resulting from dissolved CJ crystals. **(c)** Electron diffraction heat map crystallographic orientation analysis of **(b),** HAADF STEM of rods released from CJ crystal. Red, blue, and green in (c) correspond to 3 distinct crystal orientations. Other crystal orientations were not included in the analysis and will correspond to black space in (c).

2.4 Conclusions

By growing gold nanorods on pre-defined nuclei, we were able to separate nucleation and growth steps of nanorod synthesis. Seeded growth facilitated the synthesis of high aspect ratio gold nanorods within protein crystal molds. Such crystals provide a designable matrix for the synthesis of guest nanomaterials. We identified conditions such that the growth of rods depended on the presence of a seed and the resulting shape depended on the crystal scaffold used. Furthermore, the surrounding scaffold could be dissolved, releasing the rods for downstream use. This is a promising new paradigm for the scalable production of designable gold nanostructures.

REFERENCES

1. He, J. *et al. Nanoscale* **2013,** 5, 5151–5166.

2. Hao, R. *et al. Adv. Mater.* **2010,** 22, 2729–2742.

3. Pérez-Juste, J., Pastoriza-Santos, I., Liz-Marzán, L. M. & Mulvaney, P. *Coord. Chem. Rev.* **2005,** 249, 1870–1901.

4. Bukasov, R., Ali, T. A., Nordlander, P. & Shumaker-Parry, J. S. *ACS Nano* **2010,** 4, 6639–6650.

5. Kubo, S. *et al.* Tunability *Nano Lett.* **2007,** 7, 3418–3423.

6. Rosi, N. L. & Mirkin, C. A. *Chem. Rev.* **2005,** 105, 1547–1562.

7. Huang, X., Jain, P. K., El-Sayed, I. H. & El-Sayed, M. A. *Nanomed.* **2007,** 2, 681–693.

8. Jiang, X. C., Brioude, A. & Pileni, M. P. Gold Nanorods: *Colloids Surf. Physicochem. Eng. Asp.* **2006,** 277, 201–206.

9. Arvizo, R., Bhattacharya, R. & Mukherjee, P. *Expert Opin. Drug Deliv.* **2010,** 7, 753–763.

10. Watt, J., Cheong, S. & Tilley, R. D. *Nano Today* **2013,** 8, 198–215.

11. Chernak, D., Sisco, P., Goldsmith, E., Baxter, S. & Murphy, C. *NanoBiotechnology Protocols* (eds. Rosenthal, S. J. & Wright, D. W.) **2013,** 1–20, doi:10.1007/978-1-62703-468-5_1

12. Takenaka, Y. & Kitahata, H. *Chem. Phys. Lett.* **2009,** 467, 327–330.

13. Scarabelli, L., Sánchez-Iglesias, A., Pérez-Juste, J. & Liz-Marzán, L. M. *J. Phys. Chem. Lett.* **2015,** 6, 4270–4279.

14. Vigderman, L., Khanal, B. P. & Zubarev, E. R. *Adv. Mater.* **2012,** 24, 4811–4841.

15. Vigderman, L. High-Yield Synthesis and Applications of Anisotropic Gold Nanoparticles. (Rice University, **2013**).

16. Chen, Y. *Microelectron. Eng.* **2015,** 135, 57–72.

17. Kooy, N., Mohamed, K., Pin, L. & Guan, O. *Nanoscale Res. Lett.* **2014,** 9, 320.

18. Cohen-Hadar, N. *et al. Biotechnol. Bioeng.* **2006,** 94, 1005–1011.

19. Lagziel-Simis, S., Cohen-Hadar, N., Moscovich-Dagan, H., Wine, Y. & Freeman, A. Biotemplating. *Curr. Opin. Biotechnol.* **2006,** 17, 569–573.

20. Wei, H. *et al. Nat. Nanotechnol.* **2011,** 6, 93–97.

21. Guli, M., Lambert, E. M., Li, M. & Mann, S. *Angew. Chem. Int. Ed Engl.* **2010,** 49, 520–523.

22. Muskens, O. L., England, M. W., Danos, L., Li, M. & Mann, S. *Adv. Funct. Mater.* **2012,** doi:10.1002/adfm.201201718

23. Huang, Y. *et al. Nano Lett.* **2005,** 5, 1429–1434.

24. Okuda, M. *et al. Nanotechnology* **2012,** 23, 415601.

25. Kostiainen, M. A. *et al. Nat. Nanotechnol.* **2013,** 8, 52–56.

26. Ceci, P. *et al. Advanced Topics in Biomineralization* (ed. Seto, J.) **2012**.

27. Maity, B., Abe, S. & Ueno, T. *Nat. Commun.* **2017,** 8, 14820.

28. Lanci, C. J. *et al. Proc. Natl. Acad. Sci. U. S. A.* **2012,** 109, 7304–7309.

29. King, N. P. *et al. Science* **2012,** 336, 1171–1174.

30. King, N. P. *et al. Nature* **2014,** 510, 103–108.

31. Gradišar, H. *et al. Nat. Chem. Biol*. **2013,** 9, 362–366.

32. Kowalski, A. E. *et al. Nanoscale* **2016,** 8, 12693–12696.

33. Gao, C., Zhang, Q., Lu, Z. & Yin, Y. *J. Am. Chem. Soc.* **2011,** 133, 19706–19709.

34. Baksi, A. *et al. Nanoscale* **2013,** 5, 2009–2016.

35. Chaudhari, K., Xavier, P. L. & Pradeep, T. *ACS Nano* **2011,** 5, 8816–8827.

36. Xie, J., Zheng, Y. & Ying, J. Y. *J. Am. Chem. Soc.* **2009,** 131, 888–889.

37. Basu, N., Bhattacharya, R. & Mukherjee, P. *Biomed. Mater.* **2008,** 3, 34105.

38. Bhargava, S. K., Booth, J. M., Agrawal, S., Coloe, P. & Kar, G. *Langmuir* **2005,** 21, 5949–5956.

39. Computer Visualization of Three-Dimensional Image Data Using IMOD. Available at: http://bio3d.colorado.edu/imod/paper/. (Accessed: 18th September **2017**)

CHAPTER 3

Progress Towards Clonable Nanoparticles*

3.1 Synopsis

Pseudomonas moraviensis stanleyae was recently isolated from the roots of the Selenium (Se) hyperaccumulator plant Stanleya pinnata. This bacterium tolerates normally lethal concentrations of SeO_3^{2-} (selenite) in liquid culture, where it also produces Se nanoparticles. Structure and cellular ultrastructure of the Se nanoparticles as determined by cellular electron tomography shows the nanoparticles as intracellular, of narrow dispersity, symmetrically irregular and without any observable membrane or structured protein shell. Protein mass spectrometry of a fractionated soluble cytosolic material with selenite reducing capability identified nitrite reductase and glutathione reductase homologues as NADPH dependent candidate enzymes for the reduction of selenite to zerovalent Se nanoparticles. In vitro experiments with commercially sourced glutathione reductase revealed that the enzyme can reduce SeO_3^{2-} to Se nanoparticles in an NADPH- dependent process. The disappearance of the enzyme as determined by protein assay during nanoparticle formation suggests that glutathione reductase is associated with or possibly entombed in the nanoparticles whose formation it catalyzes. Chemically dissolving the nanoparticles releases the enzyme. The size of the nanoparticles varies with SeO_3^{2-} concentration, varying in size form 5nm diameter when formed at 1.0 μM [SeO_3^{2-}] to 50nm maximum diameter when formed at 100 μM [SeO_3^{2-}]. In aggregate, we suggest that glutathione reductase possesses the key attributes of a clonable nanoparticle system: ion reduction, nanoparticle retention and size control of the nanoparticle at the enzyme site.

**The work presented herein is published in Nanoscale. Richard S. Nemeth's contributions to this work include experimental design, data analysis, synthetic development and characterization of enzymatically made selenium nanoparticles used in this study. ©The Royal Society of Chemistry 2015. Nanoscale, 7, 17320-17327, 2015.*

3.2. Introduction

A *grand challenge* in biogenic inorganic nanoparticle synthesis is a clonable nanoparticle. That is, specifically, a *single* clonable polypeptide sequence that mediates the self-contained formation of an inorganic nanoparticle from inorganic salt precursors. Just as the clonable fluorophore, green fluorescent protein (GFP), is widely used for clonable contrast in biological optical microscopies,[1] a clonable inorganic and electron-dense nanoparticle is expected to find widespread use for cellular contrast in biological electron microscopy. In each case facile genetic methods for concatenating DNA encoding a protein sequence to the DNA sequence of a native cellular protein underlie the utility of clonable microscopy contrast. Expression of the resulting chimeric protein places a contrast marker alongside every instance of the native protein, enabling localization of the protein chimera in micrographs.

A clonable nanoparticle requires a polypeptide that integrates three distinct chemical activities. One activity is inorganic ion reduction or oxidation, converting soluble (ideally bioavailable and nontoxic) inorganic ions to insoluble (nanoparticulate) species. Second, the resulting inorganic nanoparticle must be retained by the polypeptide. Third, the size of the resulting nanoparticle must be large enough to identify unambiguously in a micrograph that includes biological structure, while also being small enough to minimize perturbation of cell biology and to reduce the shadow-casting that obscures biological information. An ideal size is suggested as 5 nm diameter. So far, there is no widely adopted clonable contrast marker in biological electron microscopy.

Both naturally occurring proteins as well as peptides isolated from libraries are investigated as candidate clonable nanoparticles. Naturally occurring proteins investigated include most prominently ferritin and metallothionein. In the case of the iron-storage capsule protein ferritin,[2] the requirement of 24 subunits with a total mass of nearly 0.45 MDa[3] may limit its use. Metallothionein coordination of Au(I) or Au(III) based ions is also proposed,[4–6] but these methods are not widely adopted in biological electron microscopy. This is perhaps because the Au(I) precursors are sparingly soluble in water and Au(III)-based

coordination compound precursors are easily reduced by proteins,[7–9] buffers,[10,11] and other biomolecules encountered in a cellular environment.[12–15]

Proteins associated with magnetosomes such as mms6 are also initially attractive for forming clonable iron oxides.[16] However, a recent study shows that cloning of a minimal set of magnetosome-associated genes into a new host cell results in membrane-encapsulated iron oxide nanoparticles.[17] Such a membrane would clearly disrupt the function of a clonable nanoparticle, by adding size and possibly membrane sequestering proteins tagged for study.

Another investigated source of a polypeptide satisfying the clonable nanoparticle criteria is directed evolution. Directed evolution methods have already identified several DNAs,[18–20] RNAs,[21,22] and peptides[23–25] that mediate inorganic nanoparticle formation. In fact, early reports suggested that some library-derived peptides possessed the three desired activities of reduction, retention and size control.[23,26] Subsequent studies revealed that the buffers such as HEPES[11] or other Good's Buffers,[10] in which the selections were executed, reduced the inorganic precursors.[27] The role of the evolved biomolecules is to cap the nanoparticles resulting from buffer reduction of metal ions, enforcing size and shape control. One of the best studied systems, the A3 peptide,[26,28–31] shows a preference for a size where the radius of curvature of the nanoparticle matches the curvature naturally adopted by the peptide.[28] Thus, while inorganic nanoparticle binding (retention) and size control are now well-established for peptides and polynucleotides, there are no well-established examples of peptides that catalytically or stoichiometrically reduce metal ions for the production of particles large enough to find use in biological electron microscopy.

Enzymes that reduce or oxidize metal ions into insoluble forms represent another class of biomolecule candidate for a clonable nanoparticle, and are the least extensively investigated. Such enzymes include silicateins,[32,33] silicatein homologous proteases,[34] and metal[35,36] and metalloid[37–39] reductases implicated in detoxification processes. Resulting nanoparticle size is regulated when the product is retained, by encapsulating proteins such as DPS[40] or ferritin.[40] Alternatively, enzymes release or turn over their products, allowing them to diffuse from the site of synthesis.[34,41] Notably, there are no

well-established examples of intracellular particles wherein the inorganic portion of the particle is exposed to cytosol.

In the present work, we investigate the formation, enzymology, structure, and cellular ultrastructure of biogenic selenium nanoparticles (SeNPs) made by a strain of *Pseudomonas fluoroscens, P.moraviensis* Stanleyae, recently isolated from a seleniferous environment, inside Se hyperaccumulator plant *Stanleyae pinnata*. While Se is an essential element for many organisms, the range between essentiality and toxicity is very narrow.[42] The conversion of comparatively toxic Se oxyanions, SeO_3^{2-} (selenite) and SeO_4^{2-}, (selenate) to zerovalent SeNPs by selenospecialist bacteria has be previously established.[38,39,43,44] Depending on the species, the resulting SeNPs may be extra- or intra-cellular.[45] Enzymes including nitrite reductase are identified by proteomic mass spectroscopy on purified nanoparticles or in fractionated cell extracts assayed for Se oxyanion reductase activity.[37-39] Very little is known about the mechanism of particle synthesis, the relationship between enzymes that synthesize the nanoparticles and the nanoparticles, and the physical interface between nanoparticles and the cytosol. For instance, most intracellular nanoparticles are coated by a membrane or a structured protein coat. There is also little investigation of the means of size control for biogenic and/or enzymatically produced Se nanoparticles.

In the present work, we report the first 3D electron tomographic reconstruction of cells containing SeNPs, and infer unprecedented aspects of the nanoparticle and nanoparticle/cytosol interface that may be unique to SeNPs, and especially relevant for the application of SeNPs as clonable nanoparticles. We show the possibility of size control of the nanoparticles, and show that a large fraction of enzymesare physically associated with nanoparticles. Overall, our results present the first report of a polypeptide that possesses the three coincident activities required for a clonable nanoparticle useful in cellular electron microscopy: precursor reduction, product retention, and product size-control.

3.3 Results

In order to further investigate other clonable biomolecules that may be capable of forming inorganic nanoparticles we turned to an endophyte brought to our attention by a visiting scholar. *Pseudomonas moraviensis* stanleyae was isolated from the roots of *Stanleya pinnata*, a Se hyperaccumulator plant native to western USA,[46] and observed to tolerate unusually high concentrations of SeO_3^{2-}. When grown in Luria Broth supplemented with 10 mM Na_2SeO_3, the cultures become notably pink in color during early log-phase. This color change (Figure 3.1) is associated with the formation of zerovalent (red) Se. The conversion of selenite oxyanions to zerovalent Se is a common detoxification process for bacteria that tolerate high concentrations of Se oxyanions.[47]

Figure 3.1. Photographs of *P. moraviensis* stanleyae liquid LB cultures. The culture on the left is supplemented with 10 mM SeO_3^{2-}. Upon initial growth, both cultures appear as the no-selenite control culture shown on the right. We attribute the red color of the culture, to which selenite is added, to the reduction of selenite and zerovalent red selenium.

Initial characterization of the SeNPs produced by *P. moraviensis* stanleyae was performed by transmission electron microscopy (TEM), scanning electron microscopy (SEM) with energy dispersive X-ray spectroscopy (EDS) elemental mapping, and 3-D cellular electron tomography.

An initial TEM examination of glutaraldehyde-fixed concentrated cell culture of *P. moraviensis* stanleyae, dry mounted on a carbon-coated TEM grid (Figure 3.2, panel A) revealed relatively uniform (107 ± 35 nm) high-contrast circular morphology spots both inside (or superimposed on) and outside of the bacterial cells. Scanning transmission electron microscopy of the same sampled allowed EDS mapping of elemental composition. The EDS mapping confirms that the high-contrast spots are Se-rich. (Figure 3.2, panel B) This suggests that the high-contrast spots are Se nanoparticles that account for the red color of the bacterial cultures. Similar spots were not observed in control cultures that were not supplemented with SeO_3^{2-}. At least 50 were examined in the control observation, high density spots were observed only with one cell, and in that instance the morphology was notably irregular compared to the putative SeNPs (Figure 3.3).

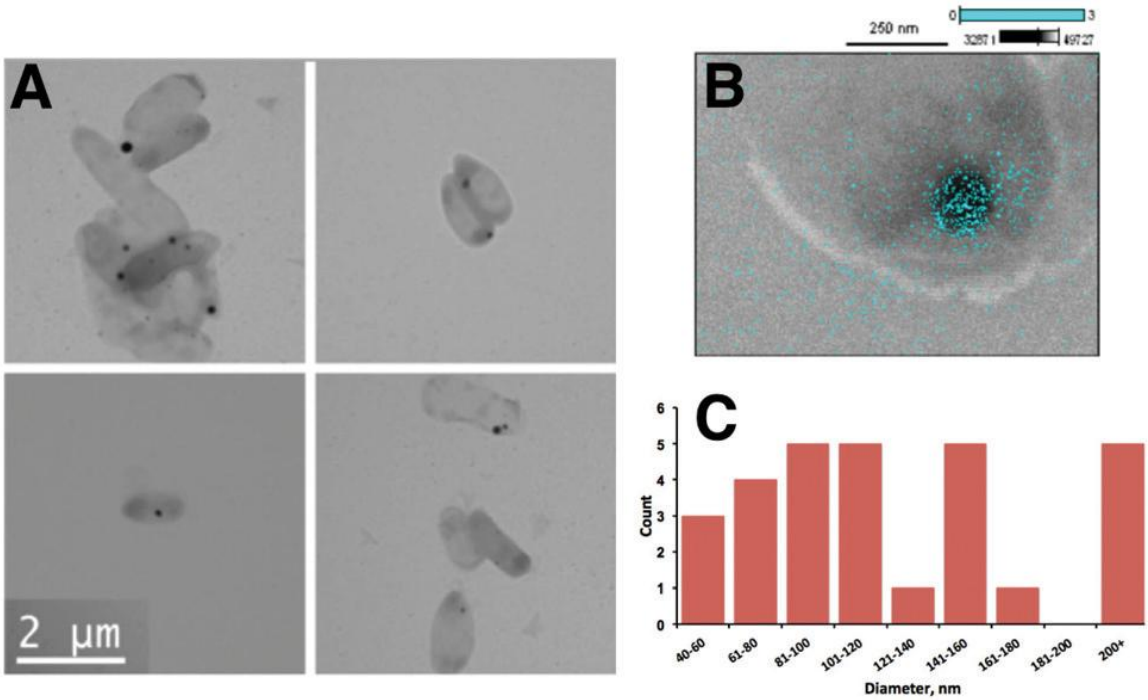

Figure 3.2. Transmission electron micrographs of glutaraldehyde-fixed dry mounted cells are shown in panel A. Electron-dense (dark) inclusions are present in many of the cells in panel A, as well as outside the cells. Panel B shows a scanning transmission micrograph of a selected area of one of the cells that includes a dark inclusion; overlaid on this inclusion is an EDS map of Se in the sample, indicating that the inclusion is Se-rich. Panel C shows a histogram of observed particle sizes.

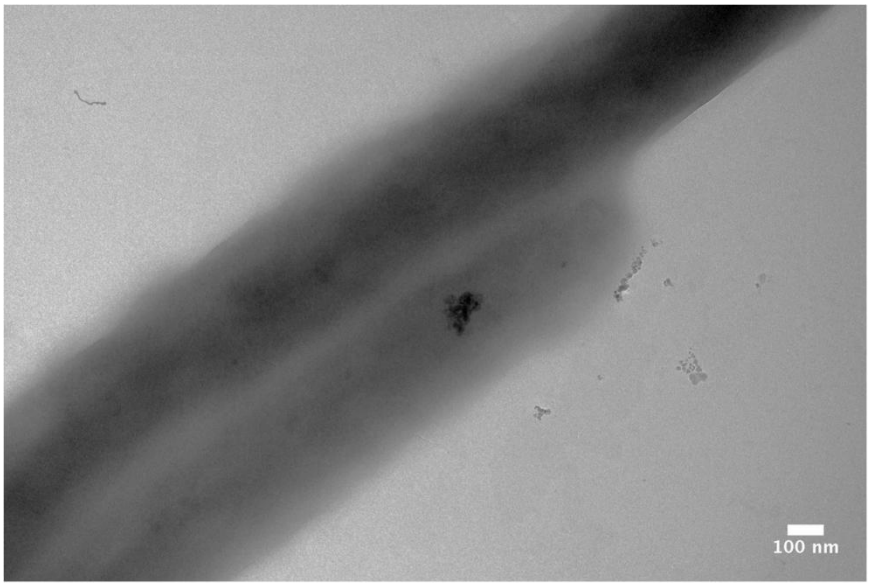

Figure 3.3. Representative micrographs showing irregular electron dense object.

Dry mount electron microscopy provides comparatively limited information compared to more sophisticated preservation and imaging methods, such as cellular electron tomogrpahy.[48,49] With appropriate preservation,[50-52] these methods allow high fidelity 3D resolution of cellular ultrastructure such as membranes and major cytoskeletal filaments, organelles and ribosomes.[53] Here we used electron tomography to definitively reveal whether the observed nanoparticles are inside the cells (as opposed to superimposed), reveal membranes, and reveal major cellular ultrastructure. *P. moraviensis* Stanleyae cells were grown as described in the methods section, both with and without 10 mM SeO_3^{2-} supplementation into the stationary phase where particles are easily discernable. Concentrated cultures were subjected to freeze substitution,[50] which provides the highest fidelity preservation of cellular ultrastructure aside from vitrification.[54] Vitrification was not used here because the size of the cells would require cryo-sectioning, which is technically difficult and not routinely successful.

3D reconstructions of both unstained and osmium stained 200 nm sections revealed large inclusions inside the cells. In the case of metal-stained cells, it was unclear whether the inclusions could be attributed to the staining of biological material or to SeNPs, although other ultrastructures (such as both inner and outer membranes) were clearly revealed (Figure 3.4).

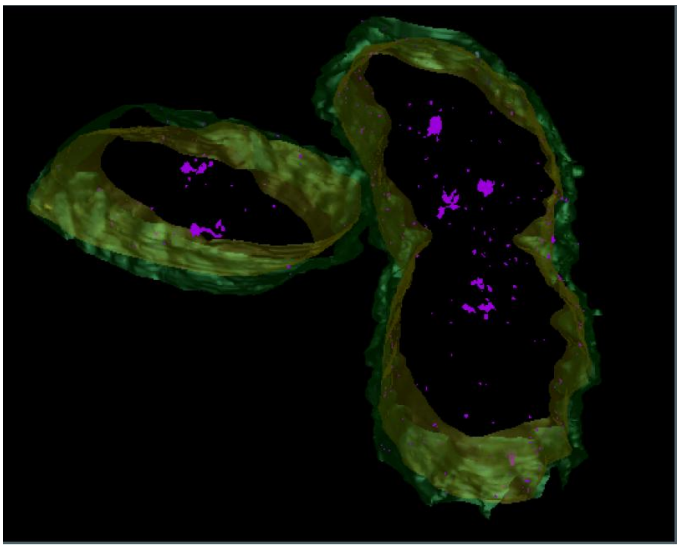

Figure 3.4. Electron tomographic reconstruction of *P. moraviensisi* stanleyae with osmium staining. The outer membrane (green) , inner membrane (yellow) and putative SeNP (pink) densities are segmented. Due to the presence of stain, the particle segmentation is ambiguous.

The reconstructions of unstained cells were more informative. Figure 3.5 shows a segmented reconstruction of a single cell; the outer membrane was segmented by hand, as is current standard practice with IMOD, while the SeNPs were sufficiently electron dense that segmentation could be accomplished automatically with a simple thresholding operation. Imodauto was set at a threshold of 1 (out of 255), which generated a model. This clearly auto-segments out high-density inclusions that we attributed to SeNPs. In each of three 3D reconstructions of cells grown with SeO_3^{2-} supplementation we observed high-contrast inclusions of 58.66 ± 2.47 nm diameter (from a total of 3 particles observed).

Figure 3.5 shows a 3D segmentation of one of the cells, with a XY view shown in panel B and an YZ view shown in panel C. These two views reveal unambiguously for the first time that large SeNPs can be intracellularly contained, where previous studies were 2D microscopy and could not rule out that particles and cells are superimposed. Notably, there is no evidence that these particles are membrane-encapsulated, as is observed for other inorganic inclusions such as magnetosomes.[55]

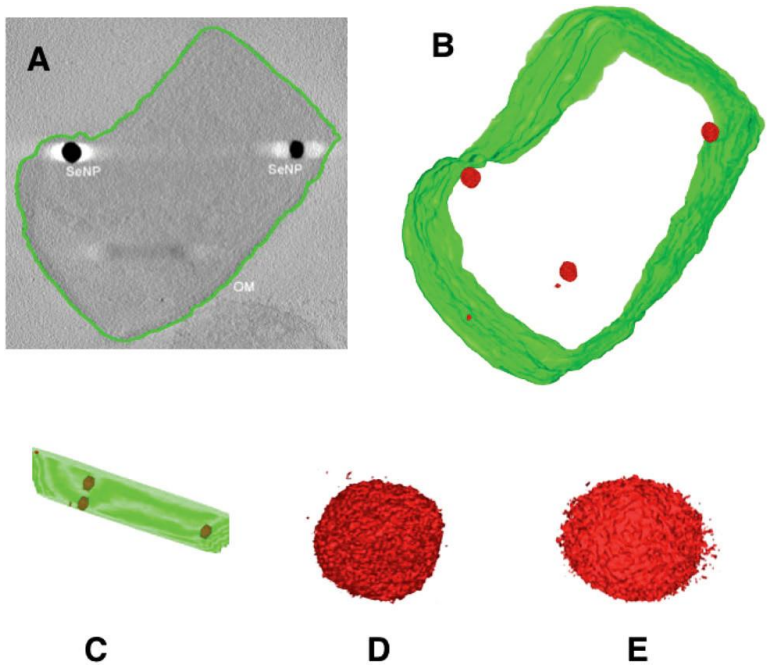

Figure 3.5. Electron tomographic reconstruction of *P. moraviensis* stanleyae. The reconstruction was segmented to reveal the outer membrane and SeNP nanoparticles (panels A-C). Magnified views of two SeNPs are show in panels D and E; panel D shows the large SeNP in the middle of the cell in panel B. Panel E shows the large SeNP in the upper left part of the cell in panel B.

Panels D and E of Figure 3.5 show the three larger intracellular particles at greater magnification. From these images it appears that while the particles are "approximately spherical" they are not perfectly spherical and in fact are symmetrically irregular. Some of the irregularity in these images is artifact. The "spikiness / texture" of the surface is also observed for the 10 nm diameter gold nanoparticles used as fiducial markers for alignment.[52] The anisotropic 'speckling' halo that surrounds some of the particles likely arises from the 'missing wedge' artifact in electron tomography.[56] Even accounting for these sources of artifact, however, the nanoparticles appear symmetrically irregular.

To derive greater insight into the mechanism of formation of these SeNPs, we identified proteins implicated in the reduction of SeO_3^{2-} to Se(0) by *P. moraviensis* stanleyae. Briefly we fractionated the soluble proteins from cell lysate on a nondenaturing polyacrylamide gel, and then stained the gel with metalloid oxyanions and electron donating cofactors. Any resulting bands indicating the presence of NADPH-dependent selenite reductase activity were excised and further analyzed by proteomic mass spectrometry.

To obtain better resolution, cell lysate of *P. moraviensis* Stanleyae grown in SeO_3^{2-}-supplemented media was further fractionated on a hydrophobic interaction column (HIC) that was eluted with different concentrations of $(NH_4)_2SO_4$. Proteins in each fraction from the HIC column were separated on a non-denaturing polyacrylamide gel. To develop bands corresponding to selenite reductases, gels were placed into nitrogen-filled zip-lock bags filled with a buffer supplemented with metalloid oxyanions and NADPH or NADH. The entire protocol was adapted from previous work by Hunter.[38]

Figure 3.6 shows the results of this experiment for the reduction of SeO_3^{2-} in the presence of NADPH. Clearly there are proteins with selenite reductase activity present in some of the HIC fractions. Tellurite (TeO_3^{2-}) reductase activity was observed with similar gel mobility, although the bands were less intense. No notable reduction of selenate or tellurate (TeO_4^{2-}) to elemental form was noted, and the reduction of SeO_3^{2-} and TeO_3^{2-} was notably weaker when NADH instead of NADPH was used as an electron donor. No bands developed in the absence of NADH or NADPH.

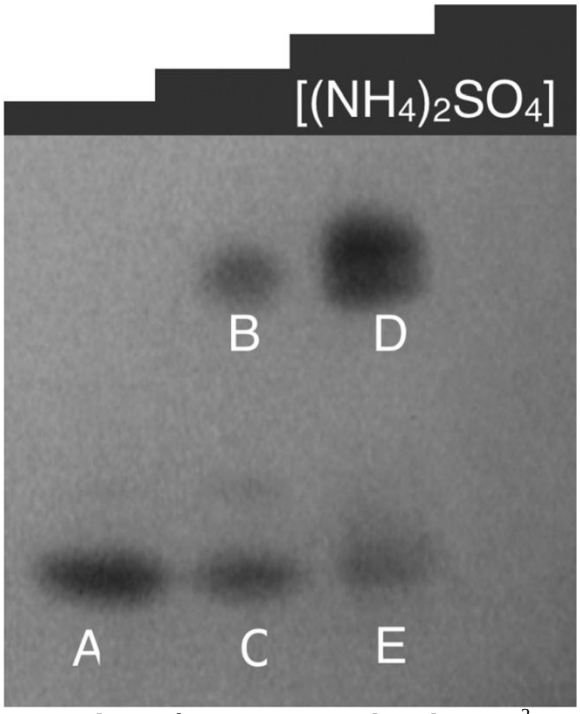

Figure 3.6. Native gel of HIC column fractions, stained with SeO_3^{2-} and NADPH to reveal bands containing enzymatic SeO_3^{2-} reductase activity. Lanes in the gel correspond to step fractions taken from a HIC column to process crude cell lysate. Lanes correspond to 0.1 M, 0.5 M, 1.0 M, 1.5 M and 2.0 M elutions of the HIC column with $(NH_4)_2SO_4$.

Figure 3.6 shows that two bands develop in the anaerobic SeO_3^{2-} + NADPH incubation condition, one that is associated with lower salt elutions from the HIC column and a second associated with higher salt elutions.

To identify the proteins involved in the observed reduction, we excised the bands and identified associated proteins by protein mass spectrometry. From a total of 5 activity bands excised and analyzed for protein content, 122 proteins were identified. Of these proteins ,7 are known to be NADPH or $NADP^+$ dependent. This set of NADPH-dependent proteins (Table 3.1) comprises a set of candidate proteins for specific NADPH-dependent SeO_3^{2-} reduction to Se(0).

Table 3.1. NADPH-dependent enzymes identified in mass spectrometry.

Oxyreductase	Accension number	MW (Da)	Cofactor/Rxn	Band association
Nitrite and sulfite reductase	gi|77459334	62 262	NADPH	B
Isocitrate dehydrogenase [*Pseudomonas fluorescens* SBW25]	gi|229591243	66 003	$NADP^+$/ATP	B, C, D
Glutathione reductase [*Pseudomonas fluorescens* Pf0-1]	gi|77459153	49 244	$NADP^+$/FAD	B, D
5,10-Methylenetetrahydrofolate reductase [*Pseudomonas fluorescens* Pf0-1]	gi|77461502	31 515	$NADP^+$/FAD	B, D
3-Ketoacyl-ACP reductase [*Pseudomonas fluorescens* Pf0-1]	gi|77460378	25 500	NADPH	A
Thiol peroxidase [*Pseudomonas fluorescens* Pf0-1]	gi|77458745	17 586	NADPH/H_2O_2	B, D
4-Aminobutyrate aminotransferase [*Pseudomonas fluorescens* Pf0-1]	gi|77456416	44 837	NADPH	A, B, C, D, E

Of these proteins, we were especially interested in glutathione reductase (GSHR) and nitrite reductase, as each was previously implicated in selenite reduction.[38,57-59] To validate the specificity and investigate the enzymatic mechanism, we obtained baker's yeast (*Saccharomyces cerevisiae*) GSHR from Sigma-Aldrich (G3664) and the NADPH-dependent cytochrome C reductase (C3381) and *Aspergillus niger* nitrate reductase (N7265) as comparison control enzymes. Each enzyme was tested for competence to reduce SeO_4^{2-}, SeO_3^{2-}, TeO_4^{2-}, and TeO_3^{2-} to zerovalent forms of Se and Te, respectively, as judged by a color change of the solution from clear to turbid red (Se) or gray (Te) upon inclusion of either NADH or NADPH as electron donors. In this initial screening of enzymes and substrate specificity, we found that GSHR with NADPH as an electron donor could reduce SeO_3^{2-} and TeO_3^{2-}, while no other combination resulted in notable metalloid oxyanion reduction.

In order to understand the mechanism by which GSHR converts these metalloid oxyanions, we first characterized basic enzymatic properties for both SeO_3^{2-} and TeO_3^{2-} substrates. K_m and V_{max} were determined by observing the rate of consumption of NADPH, which has an easily observable

spectroscopic signature (Figure 3.7). We found a K_M of 31 mM for SeO_3^{2-} and a K_M of 0.54 mM for TeO_3^{2-} (Figure 3.8). The reported K_m value of GSHR for GS-SG is ~50µM[60] suggesting that the enzyme has a substantially higher substrate affinity for GS-SG than for SeO_3^{2-}.

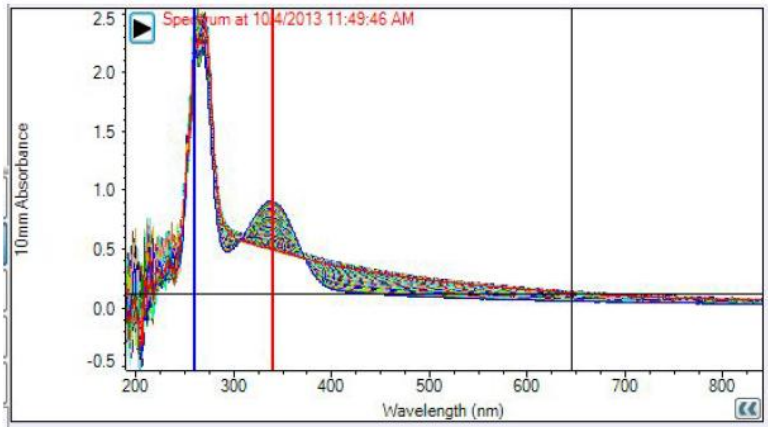

Figure 3.7. Example spectroscopic data showing enzymatic consumption of NADPH as judged by diminishment over time of the peak at 340 nm that arises from NADPH. Monitoring of this consumption (or lack thereof) allowed claims of substrate specificity and the Lineweaver-Burk plots show in Figure 3.8.

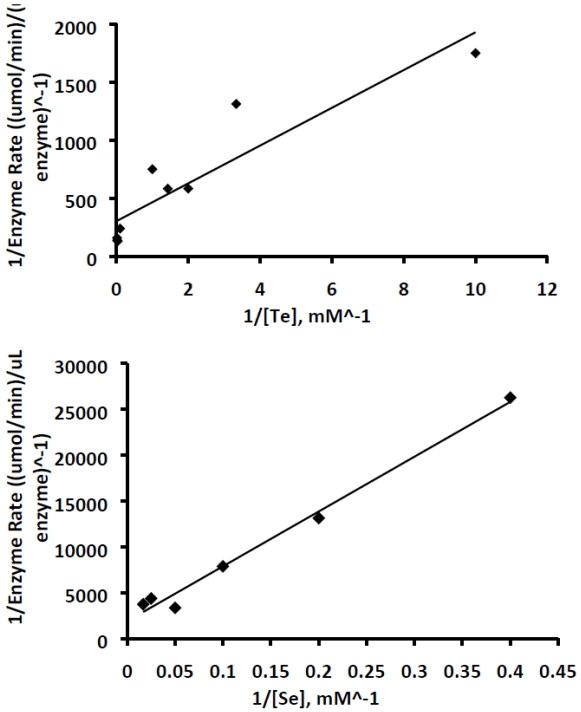

Figure 3.8. Lineweaver-Burk plots for TeO_3^{2-} and SeO_3^{2-} reduction by GSHR.

After dialysis to remove small molecules, the products of GSHR reduction of TeO_3^{2-} and SeO_3^{2-} were examined by TEM. Reduction of TeO_3^{2-} to Te(0) by GSHR produced networks of sub 5 nm particles, where the diameters are difficult to discern, similar to the previously reported enzymatic reduction of Ti^{3+} (as TiBALD) by cysteine and serine proteases.[34] Reduction of SeO_3^{2-} to Se(0) in otherwise identical conditions resulted in larger, discrete 61 ± 37 nm diameter SeNPs. Figure 3.9 shows electron micrographs of each product and a histogram of size distribution for the SeNP.

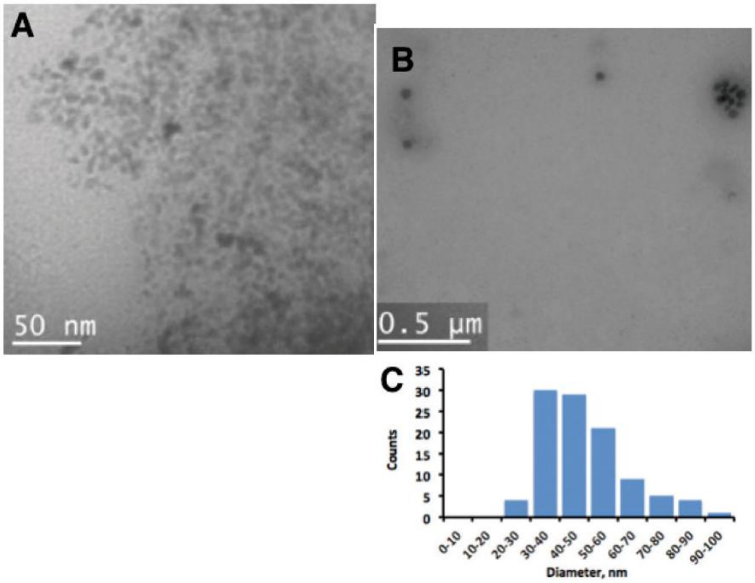

Figure 3.9. Transmission electron micrographs of the characterization of *in vitro* products of GSHR reduction of TeO_3^{2-} (panel A) and SeO_3^{2-} (panel B). Panel C shows the size distribution histogram observed for GSHR produced SeNPs.

In the enzymatic assays, we observed that the steady-state phase of product production was remarkably short-lived (Figure 3.8). We subsequently observed that the enzyme itself was consumed in the *in vitro* reaction, as determined by a Bradford assay for total protein (Figure 3.10, circles). This suggested that the enzyme is associated with the particles it synthesizes, perhaps even entombed in the particle. To test this hypothesis of association or entombment, we separated by centrifugation the enzymatically formed SeNPs from soluble enzyme. The insoluble protein fraction corresponded to 18% of the total enzyme in the assay. SeNPs are known to be dissolvable in solvents such as ethylenediamine and benzene.[61] We found that enzymatically produced SeNPs are also soluble in Bradford protein assay.

In fact, we could recover nearly quantitatively the protein that disappears from the enzymatic assay in a Bradford assay of the enzymatically produced SeNPs. This data is shown in Figure 3.10, left panel. There is evidence that the soluble fraction of GSHR is also associated with smaller SeNPs. In an SDS-PAGE of the soluble fraction of GSHR, a difference in electrophoretic mobility coupled to a 'smearing of the band', consistent with the enzyme being bound to polydisperse particles, is observed in comparison to a control reaction. Overall, we suggest that some fraction of the enzyme is associated with or entombed in the nanoparticles that the enzyme creates. When NADPH cofactor is omitted from the reaction, the enzymatic process does not proceed, and the observed enzyme concentration remains constant (Figure 3.11, diamonds).

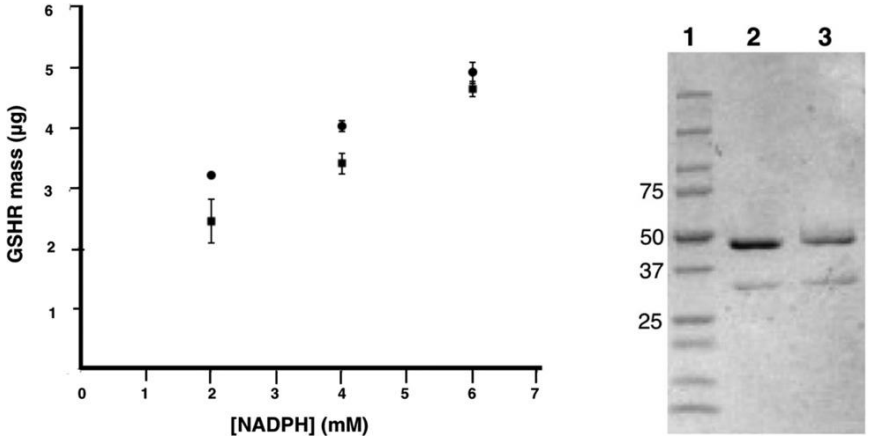

Figure 3.10. Left panel shows the amount of GSHR lost from the assay at different NADPH cofactor concentrations in circles. In squares is depicted the amount of protein measured from the insoluble selenium particles created during the assay. The agreement between protein lost from the assay and protein recovered from the particles suggests that the enzyme is associated or entombed in the particles it creates. The right pane shows an SDS-PAGE of the soluble fraction of GSHR after an assay. The small shift in electrophoretic mobility and large smear about the band can be attributed to association between the enzyme and smaller SeNPs.

The size of the enzymatically synthesized SeNPs is controllable through modulation of enzyme substrate concentrations. By varying the [NADPH] in an *in vivo* reaction, we observed that we could vary the size of the resulting particles from 2.5nm to more than 50nm diameter. The effect of [NADPH] on particle size is shown in Figure 3.12.

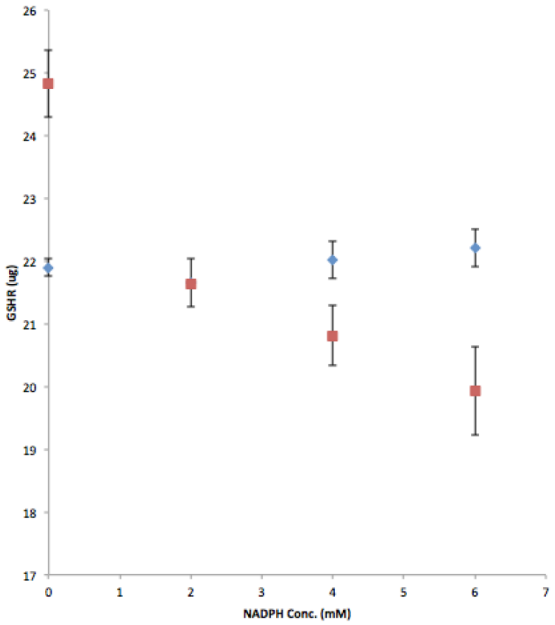

Figure 3.11. The results of a Bradford assay of a fixed amount of GSHR exposed to varying amounts of NADPH, with SeO_3^{2-} either present at 10 mM concentration (red squares) or absent (blue diamonds). When SeO32- is present (red squares) the enzyme vanishes from the assay in an NADPH dependent manner.

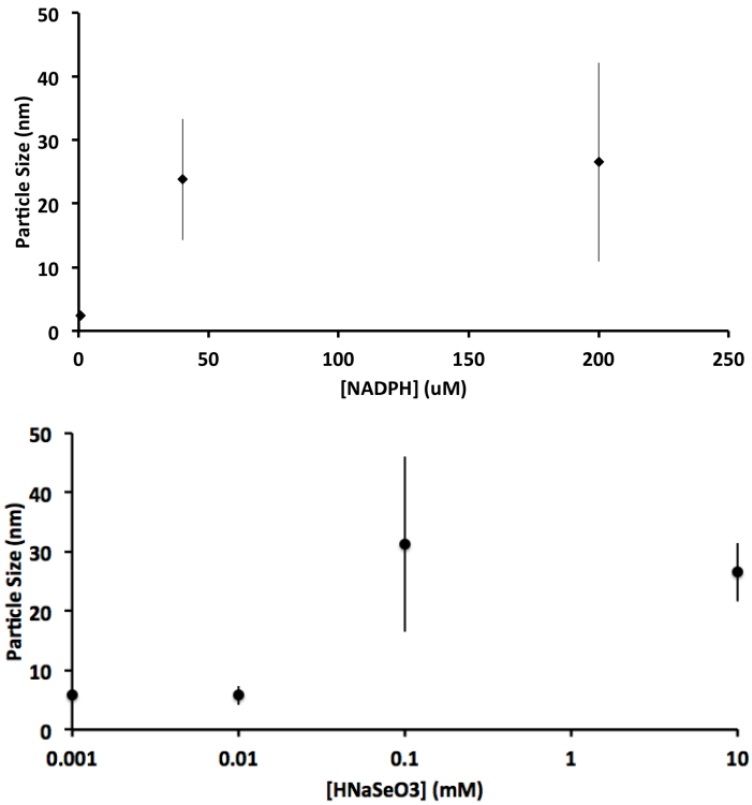

Figure 3.12. Top panel shows how particle size changes as [NADPH] cofactor is varied. Bottom panel shows distribution of particle sizes (y-axis) as a function of [SeO_3^{2-}] concentration in the assay (x-axis).

3.4 Discussion

We identify the first polypeptide capable of soluble precursor reduction, retention of reduced product at the site of reduction, and size control of the reduced product. This represents a notable step in progress toward a clonable nanoparticle, which is fundamentally different from other proposed strategies for clonable nanoparticles. First, other strategies rely on stoichiometric binding of metal ions,[4,5] or on oxidation events,[2] while this approach uses enzymes and NADPH as an electron donor to reduce inorganic precursors. We infer that the products of reduction are often retained by the enzyme that creates them, possibly by an entombing mechanism. This rare combination of three activities in biogenic nanoparticle production was previously suggested for reduction of Au(III) precursors by the same enzyme.[35] In that work, however, the resulting particles are quite small, and as noted above, Au reduction is quite promiscuous by biomolecule[8] while the selenite and tellurite reductions reported here appear specific to just a handful of enzymes, as evidenced by Figure 3.6.

We observe notable differences in the resulting size of particles, depending on the growth condition. We cultured *P. moraviensis* Stanleyae cells for up to 36 hours in the presence of SeO_3^{2-} supplementation, to ensure an abundance of SeNPs in subsequent microscopic examination. We grew cells for this extended time both with and without replacement of media. When the media was not replaced, it is likely that it is depleted of necessary nutrients at the 36 hour time point, and the cells are starving. The starvation condition of cells in Figures 3.2 and 3.3 may partially explain the difference in average particle size observed between the intracellular particles in Figure 3.2 (107 nm diameter) and Figure 3.5 (58 nm diameter). Notably, in Figure 3.4 the membranes are quite distorted, consistent with starving cells that are having difficulty maintaining homeostasis. The starvation condition was avoided for cells reconstructed for Figure 3.5 by replacing the growth media every 12 hours. Note that particle diameters measured for SeNPs in 'healthy' cells (58 nm diameter average diameter) and SeNPs produced *in vitro* by GSHR (61 nm average diameter) are within measurement error. This concurrence in particle size suggests that the *in vitro* and *in vivo* mechanisms that underlie the formation of these SeNPs are similar. Key for future application is minimizing the mass of the biological components of clonable

nanoparticles. For instance, the mass of GFP is 27 kDa, yet some studies have demonstrated that GFP concatemers can interrupt the native function of the protein fused to GFP.[61,62] A finding we make relevant to minimizing the mass of clonable nanoparticle tags is that the SeNPs described here may be effectively naked. This stands in contrast to the well-established intracellular inorganic nanoparticles, which are coated either by a membrane or by a structured protein capsule.

We hypothesize that the particles are naked, with the Se(0) exposed to the cytosol, from a combination of structural and chemical evidence. From the tomographic reconstructions, we observe no evidence for a membrane around the SeNPs, while membranes are easily observed for naturally occurring magnetite nanoparticles.[55] The low symmetry of the particles, dispersity, and differences in average size that depend on growth conditions suggest that there is no structured protein coat, such as that found with ferritin and DPS-coated nanoparticles.

Chemically, we note that nearly all clusters and nanoparticles require a ligand shell to quench the chemical reactivity associated with the open valence electron shells of most pure elements. A handful of elements, however, including Se and Te as well as As, Bi, and Sb are known to form stable naked cluster compounds.[63]

This is in many cases because the element can achieve noble gas-like electron counts by catenation, often resulting in ring structures in the solid state, such as the well-known S_n, Se_n, and Te_n ring compounds where $6 \leq n \leq 8$. Indeed, a recent report suggests that while the surface of SeNPs is more complex than an approximately scaled giant naked Se cluster, the surfaces are stable without formal ligation.[64] Furthermore, protein mass spectrometry on purified SeNPs fails to identify candidate proteins that are known to interact with inorganic ions or surfaces.[37] Thus, the combination of irregular symmetry, absence of a membrane, and plausibility of a ligand-free surface suggests that SeNPs may represent the first described class of cytosol exposed inorganic nanoparticle surfaces.

The commercially sourced GSHR and GSHR or GSHR-like enzymes identified in *P. moraviensis* Stanleyae are not immediately useful as a clonable label in cellular EM. First, the resulting SeNPs are substantially larger than practical; second, other GSHRs, nitrite reductases, and thioredoxin[65] may also

produce background particles. While these enzymes are not characterized *in vitro* as producing SeNPs, they are characterized as using SeO_3^{2-} as a substrate. We have not yet evaluated the portability of this clonable nanoparticle for use in other cell lines. The concentrations of SeO_3^{2-} we used in both the *in vitro* and *in vivo* work herein are in the range where toxicity is expected for most cells and organisms. The K_M of the baker's yeast enzyme is low, especially compared to oxidized GS-SG and GS-Se-SG substrates investigated historically for this enzyme.[60,66] Due to the measured K_M, the baker's yeast GSHR will always require typically toxic concentrations of SeO_3^{2-} for nanoparticle formation. Furthermore, specialized selenium transporters that may be present in the selenium hyperaccumulator studied here may also enable the large intracellular particles observed in Figures 3.2 and 3.5. Thus, we anticipate cloning the GSHR-like enzyme from *P. moraviensis* Stanleyae, under the hypothesis that this selenium-specialized enzyme will have a much more favorable K_M, and that the enzyme may function well with physiologically normal concentrations of SeO_3^{2-} while simulatenously conferring resistance to Se toxicity to cells in which it is expressed. An enzyme optimized for selenite or tellurite reduction may allow superior labeling specificity by kinetically outrunning any competing reactions.

While additional work is required to complete the adaptation of this clonable nanoparticle approach for general cellular use, this approach may find more immediate use in labeling purified macromolecular complexes. Presently labeling with *ex situ* synthesized gold nanoparticles is state-of-the-art for this purpose, with applications in molecular EM, X-ray free-electron laser, and SAXS studies of macromolecular complexes.[67] A clonable approach to this contrast problem may make this sort of tagging much more facile.

For instance, Se (and Te) oxyanions have notable advantages as precursors over previously investigated Au and Fe-based systems. The Au(I) and Au(III) coordination compounds are broadly cross-reactive (i.e., easily reduced into background particulate material) by a wide swath of biomolecules and buffers.[8,10,11] This broad cross-reactivity may explain the dearth of follow up to reports of metallothionein / Au combinations as molecular and cellular EM labels. In contrast, the present work and some

preceding work suggest that the palette of proteins that possess notable reactivity against the metalloid oxyanions TeO_3^{2-} and SeO_3^{2-} is comparatively limited in number.

Improved size control may be imposed by concatenated or co-expressed peptides. Several dodecapeptides are now known to impose size control[28] on a number of *in vitro* synthesized metal nanoparticles.[68] Similar peptides may be isolated to impose size control on SeNPs or TeNPs.

3.5 Conclusions

In conclusion, we identify the first polypeptide that appears capable of synthesizing, retaining and size-controlling an inorganic nanoparticle. By virtue of their metalloid composition, the particles may be naked and exposed to free cytosol. We also find that metalloid oxyanions are comparatively selective in their cross-reactivity against biological molecules. Overall, we suggest that metalloid reductases, including the GSHR-like reductase characterized here, comprise a class of enzymes that may find use in imaging applications needing a clonable nanoparticle.

Further we also present a small 15 amino acid peptide that may also potentially be useful as a tag. While the size of the nanoparticle formed is in the ideal range of 3-5 nm, it may be difficult to utilize iron inside of a cell as iron ions are carefully corralled inside of a cell[77] due to concerns of forming free radicals.[78,79] While this peptide may be ineffective as a potential tag due to difficulties in controlling both iron concentration and iron species formation inside of a cell, it does still however display interesting properties towards controlling shape and size of an iron oxide nanoparticle.

REFERENCES

1. Giepmans, B. N. G., Adams, S. R., Ellisman, M. H., Tsien, R. Y. *Science* **2006**, *312*, 217–224.

2. Wang, Q., Mercogliano, C. P., Löwe, J. *Structure* **2011**, *19*, 147–154.

3. Theil, E. C. *Annu. Rev. Biochem.* **1987**, *56*, 289–315.

4. Mercogliano, C. P. & DeRosier, D. J. *J. Mol. Biol.* **2006**, *355*, 211–223.

5. Mercogliano, C. P. & DeRosier, D. J. *J. Struct. Biol.* **2007**, *160*, 70–82.

6. Diestra, E., Fontana, J., Guichard, P., Marco, S., Risco, C. *J. Struct. Biol.* **2009**, *165*, 157–168.

7. Baksi, A., Xavier, P. L., Chaudhari, K., Goswami, N., Pal, S. K., Pradeep, T. *Nanoscale* **2013**, *5*, 2009–2016.

8. Xavier, P. L., Chaudhari, K., Baksi, A., Pradeep, T. *Nano Rev.* **2012**, *3,* 14767.

9. Chaudhari, K., Xavier, P. L., Pradeep, T. *ACS Nano* **2011**, *5*, 8816–8827.

10. Ahsan Habib, M. T. *Bull. Chem. Soc. Jpn. - BULL CHEM SOC JPN* **2005**, *78*, 262–269.

11. Xie, J., Lee, J. Y., Wang, D. I. C. *Chem. Mater.* **2007**, *19*, 2823–2830.

12. Turkevich, J., Stevenson, P. C., Hillier, J. *Discuss. Faraday Soc.* **1951**, *11*, 55–75.

13. Frens, G. *Nature* **1973**, *241*, 20–22.

14. de la Fuente, J. M. & Penadés, S. *Biochim. Biophys. Acta* **2006**, *1760*, 636–651.

15. Haizhen Huang, X. Y. *Carbohydr. Res.* **2004**, *339*, 2627–2631.

16. Amemiya, Y., Arakaki, A., Staniland, S. S., Tanaka, T., Matsunaga, T. *Biomaterials* **2007**, *28*, 5381–5389.

17. Kolinko, I. *et al. Nat. Nanotechnol.* **2014**, *9*, 193–197.

18. Richards, C. I., Choi, S.; Hsiang, J.-C., Antoku, Y.; Vosch, T., Bongiorno, A., Tzeng, Y.-L., Dickson, R. M. *J. Am. Chem. Soc.* **2008**, *130*, 5038–5039.

19. Guo, W., Yuan, J., Dong, Q., Wang, E. *J. Am. Chem. Soc.* **2010**, *132*, 932–934.

20. Díez, I. & Ras, R. H. A. *Nanoscale* **2011**, *3*, 1963–1970.

21. Gugliotti, L. A., Feldheim, D. L., Eaton, B. E. *Science* **2004**, *304*, 850–852.

22. Gugliotti, L. A., Feldheim, D. L., Eaton, B. E. *J. Am. Chem. Soc.* **2005**, *127*, 17814–17818.

23. Naik, R. R., Jones, S. E., Murray, C. J., McAuliffe, J. C., Vaia, R. A., Stone, M. O. *Adv. Funct. Mater.* **2004**, *14*, 25–30.

24. Naik, R. R., Stringer, S. J., Agarwal, G., Jones, S. E., Stone, M. O. *Nat. Mater.* **2002**, *1*, 169–172.

25. Whaley, S. R., English, D. S., Hu, E. L., Barbara, P. F., Belcher, A. M. *Nature* **2000**, *405*, 665–668.

26. Slocik, J. M., Stone, M. O., Naik, R. R. *Small* **2005**, *1*, 1048–1052.

27. Diamanti, S., Elsen, A., Naik, R., Vaia, R. *J. Phys. Chem. C* **2009**, *113*, 9993–9997.

28. Yu, J., Becker, M. L., Carri, G. A. *Langmuir* **2012**, *28*, 1408–1417.

29. Tomczak, M. M., Slocik, J. M., Stone, M. O., Naik, R. R. *Biochem. Soc. Trans.* **2007**, *35*, 512–515.

30. Chen, C.-L., Zhang, P., Rosi, N. L. *J. Am. Chem. Soc.* **2008**, *130*, 13555–13557.

31. Chen, C.-L., Rosi, N. L. *Angew. Chem. Int. Ed.* **2010**, *49*, 1924–1942.

32. Cha, J. N., Shimizu, K., Zhou, Y., Christiansen, S. C., Chmelka, B. F., Stucky, G. D., Morse, D. E. *Proc. Natl. Acad. Sci.* **1999**, *96*, 361–365.

33. Curnow, P., Bessette, P. H., Kisailus, D., Murr, M. M., Daugherty, P. S., Morse, D. E. *J. Am. Chem. Soc.* **2005**, *127*, 15749–15755.

34. Smith, G. P., Baustian, K. J., Ackerson, C. J., Feldheim, D. L. *J. Mater. Chem.* **2009**, *19*, 8299–8306.

35. Scott, D., Toney, M., Muzikár, M. *J. Am. Chem. Soc.* **2008**, *130*, 865–874.

36. Silver, S., Phung, L. T. *J. Ind. Microbiol. Biotechnol.* **2005**, *32*, 587.

37. Lenz, M., Kolvenbach, B., Gygax, B., Moes, S., Corvini, P. F. X. *Appl. Environ. Microbiol.* **2011**, *77*, 4676–4680.

38. Hunter, W. J. *Curr. Microbiol.* **2014**, *69*, 69–74.

39. Kessi, J. *Microbiology* **2006**, *152*, 731–743.

40. Bozzi, M., Mignogna, G., Stefanini, S., Barra, D., Longhi, C., Valenti, P., Chiancone, E. *J. Biol. Chem.* **1997**, *272*, 3259–3265.

41. Kröger, N. *et al*. *Angew. Chem. Int. Ed.* **2006**, *45*, 7239–7243.

42. Tinggi, U. *Toxicol. Lett.,* **2003**, 137, 103–110.

43. Hunter, W. J. & Manter, D. K. *Cur. Microbiol.,* **2008**, *57*, 83–88.

44. Hunter, W. J. & Manter, D. K. *Cur. Microbiol.,* **2009**, *58*, 493–498.

45. Oremland, R. S., Herbal, M. J., Blum, J. S., Langley, S., Beveridge, T. J., Ajayan, P.M., Sutto, T., Ellis, A. V., Curran, S. *Appl. Environ. Microbiol.* **2004**, *70*, 52–60.

46. Galeas, M. S., Zhang, L. H., Freeman, J. L., Wegner, M.; Pilon-Smiths, E. A. H. *New Phytol.* **2006**, *173*, 517–525.

47. Hunter, W. J. & Manter, D. K. *Curr. Microbiol.* **2011**, *62*, 565–569.

48. McIntosh, R., Nicastro, D., Mastronarde, D. *Trends Cell Biol.* **2005**, *15*, 43–51.

49. Robinson, C. V. & Sali, A.: Baumeister, W. *Nature* **2007**, *450*, 973–982.

50. McDonald, K. & Morphew, M. K. *Microsc. Res. Tech.* **1993**, *24*, 465–473.

51. Giddings, T. H. *J. Microsc.* **2003**, *212*, 53–61.

52. Iancu, C. V. *et al*. *Nat. Protoc.* **2006**, *1*, 2813–2819.

53. Frangakis, A. S. *et al. Proc. Natl. Acad. Sci. U. S. A*. **2002**, *99*, 14153–14158.

54. Nickell, S., Kofler, C, Leis, A. P., Baumeister, W. A. *Nat. Rev. Mol. Cell Biol.* **2006**, *7*, 225–230.

55. Komeili, A., Li, Z., Newman, D., Jensen, G. J. *Science* **2006**, *7*, 242–245.

56. Jensen, G. J., Briegel, A. *Curr. Opin. Struct. Biol.* **2007**, *17*, 260–267.

57. Butler, C. S., Debieux, C. M., Dridge, E. J., Splatt, P., Wright, M. *Biochem. Soc. Trans.* **2012**, *40*, 1239–1243.

58. Basaglia, M., Toffanin, A., Baldan, E., Bottegal, M., Shapleigh, J. P., Casella, S. *FEMS Microbiol. Lett* **2007**, *269*, 124–130.

59. Garbisu, C., Ishii, T., Leighton, T., Buchanan, B. B. *Chem. Geol.* **1996**, *132*, 199.

60. Jornstedt, M. B., Kumar, S.; Holmgren, A. *Methods Enzymol.* **1995**, *252*, 209–219.

61. Lu, J., Xie, Y., Xu, F., Zhu, L. *J. Mater. Chem.* **2002**, *12*, 2755–2761.

62. Margolin, W. *J. Bacteriol.* **2012**, *194*, 6369–6371.

63. Swulius, M. T., Jensen, G. J. *J. Bacteriol.* **2012**, *194*, 6382–6386.

64. Corbett, J. D. *Chem. Rev.* **1985**, *85*, 383–397.

65. Scopigno, T., Steurer, W., Yannopoulos, S. N., Chrissanthopoulos, A., Krisch, M., Ruocco, G., Wagner, T. *Nat. Commun.* **2011**, *2*, 195.

66. Kumar, S., Bjornstedt, M., Holmgren, A. *Eur. J. Biochem.* **1992**, *207*, 435–439.

67. Ackerson, C. J., Powell, R. D., Hainfeld, J. F. *Methods Enzymol.* **2010**, *481*, 195–230.

68. Bjornstedt, M., Kumar, S.; Holmgren. *J. Biol. Chem.* **1992**, *267*, 8030–8034.

CHAPTER 4

The Metalloid Reductase of *Pseudomonas Moravenis* stanleyae Conveys Nanoparticle Mediated Metalloid Tolerance

4.1 Synopsis

A glutathione reductase-like enzyme in *Pseudomonas moraviensis* stanleyae was previously implicated as underlying the bacterium's remarkable SeO_3^{2-} tolerance. Herein, this enzyme is sequenced, recombinantly expressed and fully characterized. The enzyme is highly adapted for selenodiglutathione substrates (K_M = 336 μM) compared to oxidized glutathione (K_M= 8.22 μM). Recombinant expression of this enzyme in laboratory strains of *E. coli* conveys a 10-fold increase IC_{90} for SeO_3^{2-} . Moreover, selenium nanoparticles are observed when the enzyme is overexpressed in cells exposed to SeO_3^{2-}, but not in corresponding no-enzyme controls. Analysis of structural homology models of the enzyme reveal changes in parts of the enzyme associated with product release, which may underlie the Se-substrate specialization. Combined, the observations of adaptation to Se reduction over oxidized glutathione reduction as well as the portability of this nanoparticle-mediated SeO_3^{2-} tolerance into other cell lines suggests that the *P. moraviensis* glutathione reductase may be better described as a glutathione reductase-like metalloid reductase.

4.2 Introduction

Enzymatic conversion of soluble inorganic ions into insoluble forms is accomplished by enzyme centers such as those found in ferritin, magnetosomes and silicateins. This enzymatic alteration in solubility state facilitates the synthesis of biogenic inorganic materials.[1–3] These naturally occurring catalysts, in concert with accessory proteins, can exhibit control over subsequent materials composition, oxidation state, morphology and structure. These natural precedents suggest that the intentional engineering of biological diversity could underlie engineered diversity in biogenically synthesized inorganic materials. Such inorganic materials – made by laboratory evolved or engineered biomolecules

(peptides, proteins, nucleic acids) attract attention for catalysis, self-assembly, and in bio-contrast (labeling) applications.[4–8]

Any self-contained biological system for synthesizing an inorganic nanostructure will generally require an oxidoreductase activity, enabling conversion of inorganic ions from soluble to insoluble oxidation states. Ferritins and DPS proteins accomplish this with ferroxidase enzymatic centers.[9,10] Silicateins accomplish this with substrate reduction through an active site serine,[11] whereas we reported previously that the silicatein homologous class of cysteine-proteases can accomplish the similar redox chemistry with TiO.[12]

We recently reported on the ability of glutathione reductase (GSHR) to enzymatically reduce selenite (SeO_3^{2-}) to zerovalent red selenium in a nicotinamide adenine dinucleotide phosphate (NADPH) dependent reaction.[13] Similar, although diminished activity, was observed for the same enzyme in reducing tellurite (TeO_3^{2-}) to elemental Te. Our prior work identified selenite reductase activity in *Pseudomonas moravenis* stanleyae. This microbe attracted our attention because it is found as an endophyte in the selenium tolerant plant, *Stanleya pinnata*. When cultured independently in liquid media, it tolerates SeO_3^{2-} supplementation in liquid culture up to 10mM. This is 10-fold more than the SeO_3^{2-} tolerance of most other microbes. We attributed the observed selenite reduction activity of *P.* m*oravenis* to a GSHR-like enzyme on the basis of proteomic mass spectrometry of an in-gel *in situ* selenium reductase activity.

GSHRs generally belong to the family of pyridine nucleoside dependent oxidoreductases. This enzyme family also, notably, includes another well-characterized metal reducing enzyme -- mercuric reductase.[14] Within this enzyme family, active sites are highly conserved. Typical active site peptide sequences are CXXXXC for type I and CXXC for type II enzymes.[15] This class of enzymes have demonstrated their ability to reduce a variety of metal ions to zerovalent forms including Se, Hg, Te, Fe, Cr, and U. [16–19] GSHR is reported to reduce Au(III) to zerovalent form as well.[20] Thus, the class of pyridine nucleoside dependent oxidoreductases may represent an evolutionarily adaptable platform of

inorganic ion reductases, with modifications to the enzyme altering metal ion selectivity. Such a catalytic center, with alterable precursor selectivity, is of interest in biogenic inorganic nanoparticle synthesis.

In prior study, we characterized commercially sourced *Saccharomyces Cervisiae* (*S. Cervisiae*) GSHR for selenite reductase activity, showing the ability of the enzyme to oxidize NADPH while reducing SeO_3^{2-} to Se(0) nanoparticles.[13] In the present study, we characterize a homologous metalloid reductase from the seleno-specialist *P. moravenis*. We find that the substrate selectivity of the metalloid reductase (K_M) shows a substantially larger preference for GS-Se-SG relative to all other reported glutathione reductase enzymes. These enzymatic properties can be partially rationalized in terms of sequence and corresponding homology-modeled structure of the enzyme. We also observe that expressing this enzyme in laboratory strains of *E. Coli* (BL21, SS320) results in increased tolerance to SeO_3^{2-}, as well as the presence of Se nanoparticles in these cells. Overall, our data suggests that the enzyme may be best described as a glutathione reductase-like-metalloid reductase (GRLMR).

4.3 Results and Discussion

Altered substrate specificity of GRLMR enzymes, favoring selenodiglutathione (GS-Se-SG) over oxidized glutathione (GSSG) as a substrate could underlie the remarkable SeO_3^{2-} tolerance of *P. Moravenis* stanleyae. We therefore characterized the *P. Moravenis* stanleyae GRLMR enzyme identified previously. The DNA sequence of the enzyme was acquired through a full-genome sequencing (ACGT Inc,Wheeling, IL). Sequencing was conducted using *de novo* paired end sequencing.[21] This revealed a genome where 70.3% of the nucleobases have, at the most, a 1:1000 probability of mis-assignment. Figure 5.3.1 shows the "Quality Score" (Q score) for each sequenced base with Q=-log10(e). Q scores, are derived from a phred-like error probability assessment of each individual nucleotide.[22]

A BLAST search of the genomic sequence, using the *Pseudomonas* R-28S GSHR as a reference, identified one GSHR-like sequence, with 93% sequence homology. Sequence alignment of this GRLMR DNA using Serial Cloner show high similarity (98.00%) to *Pseudomonas fluorescines* (*P. fluorescines*) GSHR and modest similarity (67 – 71%) to *E. coli*, *S. cervisiae*, and *Homo sapiens* (*H. sapiens*) GSHR DNA. The sequence similarities are summarized in Table 4.1, and full alignments are shown in Chapter

5.3. The DNA sequence, combined with homology modeling of the structure suggest that all of the structural domains of Type I pyridine nucleotide dependent oxidoreductases, including catalytic, dimerization, nucleotide binding, and substrate/product binding domains[15,23,24] are present in this enzyme. This GRLMR shows 19% DNA sequence homology to mercuric reductase from *Pseudomonas Aeruginosa*.

Table 4.1. Sequence and structural homology.

	PM MTLR	**PF GSHR**	**EC GSHR**	**SC GSHR**	**HS GSHR**
PM MTLR		93.10%/ 1.56	74.14%/ 1.23	60.78%*/ 1.27	64.71%/ 1.31
PF GSHR	98.00%/ 1.71		77.59%/ 1.05	75.47%*/ 1.12	68.00%*/ 1.07
EC GSHR	67.42%/ 1.44	68.31%/ 1.42		81.48%*/ .87	79.63%*/ .85
SC GHSR	70.92%/ 1.56	73.48%/ 1.33	74.61%/ 1.17		84.91%/ .56
HS GSHR	70.34%/ 1.44	70.63%/ 1.24	78.97%/ 1.07	75.77%/ .92	

Sequence similarity (left value) and RMSD calculations (right values). PF- *P. fluoresceine*, EC- *E. Coli*, SC- *S. cervisiaI*, HS- *H. sapiens*.

Homology modeling using intensive parameters on the Phyre 2 server[25] suggests that the structure of the *Pseudomonas* derived GSHR and GRLMR enzymes are homologous to other GSHR enzymes, despite modest DNA sequence divergence. Table 4.1 shows the root mean squared deviation of atomic positions (RMSD) values for a set of GSHR homology models and/or crysatal structures. Overall, the RMSD values for these structures are similar, suggesting an overall structural homology between GRLMR, and GSHR from *P. fluorescines*, *E. Coli, H. sapiens*, and *S. Cervisiae*.

Under the hypothesis that the GRLMR enzyme has altered selectivity relative to other characterized GSHRs, we characterized the enzyme kinetics of both GRLMR and *S. Cervisiae* GSHR. We expressed GRLMR recombinantly in *E. Coli* BL21 cells. Following a 6x-histidine tag purification, we determined the Michaelis-Menton constants (K_M) for both GRLMR and commercially sourced *S. Cervisiae* GSHR (Sigma, G3664). The K_M of each enzyme was determined for each of 3 substrates: SeO_3^{2-}, GSSG, and GS-Se-SG. While SeO_3^{2-} (Alfa Aesar, 12585) and GSSG (Sigma, G4376) are commercially available, we synthesized GS-Se-SG according to previous published methods. [26]

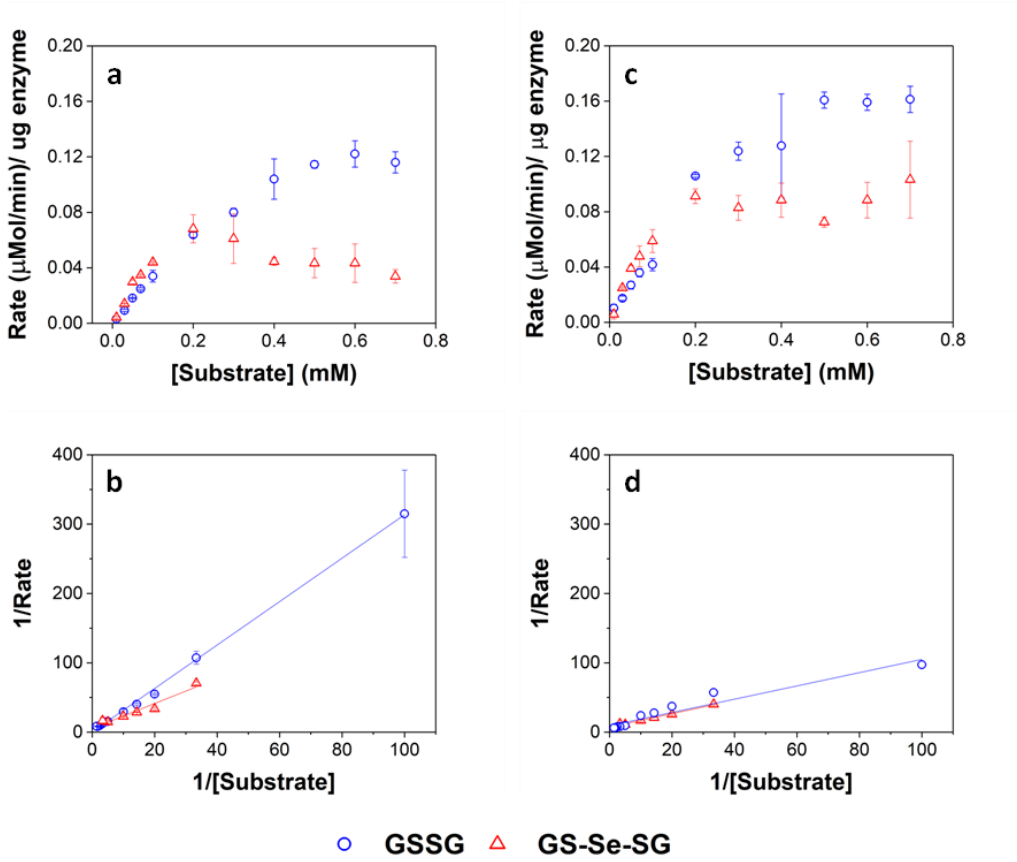

Figure 4.1. Substrate activity assays (a) GRLMR, (c) BY GSHR, with corresponding Lineweaver-Burke plots. b) GRLMR. d) BY GSHR.

The enzymatic rates for both enzymes with both GSSG and GS-Se-SG substrates are plotted in Figure 4.1, panels a and c. Data is plotted as NADPH cofactor consumption, observed experimentally as depletion of a spectroscopic peak characteristic of NADPH (but not NADP) at 340nm. The decay rate as measured at 340nm was converted to a normalized reaction rate. Lineweaver-Burke plots (shown as insets) were generated for each enzyme to determine V_{max} and K_M for the corresponding substrates. The determined K_M values for each enzyme/substrate combination are shown in Table 4.2.

Table 4.2. Enzyme Kinetics.

Enzyme/Substrate	**GRLMR K_m**	**SC GSHR K_m**	**GRLMR V_{max}**	**SC GSHR V_{max}**
GSSG	8.22mM	103µM	2.62	.107
GS-Se-SG	336µM	133µM	.187	.137

V_{max} reported in (µMol/min)/(µg of enzyme).

For the GRLMR enzyme, we observe a remarkable specialization of the enzyme for GS-Se-SG over GSSG. Specifically the K_M of GRLMR is 25 times more favorable for GS-Se-SG as compared to GSSG. This difference in K_M for the two substrates strongly implies that the enzyme is specialized for Se-reduction over GSSG reduction. For *S. Cervisiae* GSHR, we determined similar K_M values for GSSG and GS-Se-SG substrates, with the enzyme showing a slightly greater affinity for GSSG. The values we find for both substrates are consistent with the previous findings from other research groups. [13,26 27] The K_M of GSHR for SeO_3^{2-} has not been previously reported, to our knowledge. The physiological relevance of the SeO_3^{2-} K_M is questionable, since Se salts such as SeO_3^{2-} are converted to GS-Se-SG *in vivo*. [28] We established here the K_M for SeO_3^{2-} for both GRLMR and *S. Cervisiae* GSHR because we identified GRLMR on the basis of SeO_3^{2-} reductase activity, but note that the value is sufficiently unfavorable compared to GSH based substrates that it is unlikely to be physiologically relevant.

The V_{max} for GS-SG and GS-Se-SG substrates track in tandem up to initial concentrations of 0.20 mM. Deviations begin near a concentration of .3mM, where the rate for GS-Se-SG has reached its maximum velocity while the rate for oxidized glutathione continues to increase until roughly .6mM substrate concentration. The maximum velocity observed for the GSSG is approximately fourteen times greater than the V_{max} for GS-Se-SG, but this occurs at a larger substrate concentration for GSSG, accounting for the lower affinity. It is possible that the fall-off in rate that we observe at higher GS-Se-SG concentrations is artifactual, arising from interference in the optical assay by the selenium nanoparticles produced during the experiment.

Overall, the K_M values we find suggest a strong substrate preference for GS-Se-SG for the GRLMR enzyme. This is in contrast to essentially no differentiation between the substrates for other characterized GSHR enzymes. To our knowledge, this is the first finding of an enzyme specialized for reduction of GS-Se-SG over any other substrate..

We hypothesized that if the GRLMR conveys SeO_3^{2-} tolerance to *P. moravenis*, then recombinant expression of this enzyme may convey similar tolerance to the host-organism for GRLMR expression. To evaluate this hypothesis, we transformed lab expression strains of *E. coli*, BL21 and SS320, with the

Isopropyl β-D-1-thiogalactopyranoside (IPTG) inducible expression vector described above. For GRLMR enzyme-expressing *E. coli*, we determined selenite tolerance as the concentration of SeO_3 that kills 90% of the cells (IC_{90}). We also examined cells microscopically for presence or absence of SeNPs.

For IC_{90} determination, identical volumes of cells were plated on LB-Agar and LB-Agar + SeO_3^{2-}, each in triplicate, and grown overnight at 37°C. The following day, colony forming units (cfus) were counted. IC_{90} was calculated as the percentage of cfus present relative to an identical control supplemented with 1μM SeO_3^{2-}. We determined 1 μM SeO_3^{2-} necessary for maximizing the number of observed cfus. We hypothesize that such supplementation is necessary because the overexpression of a SeO_3^{2-} reducing enzyme in these cells reduces and makes unavailable the essential amount of Se needed as a micronutrient for optimum growth.[29]

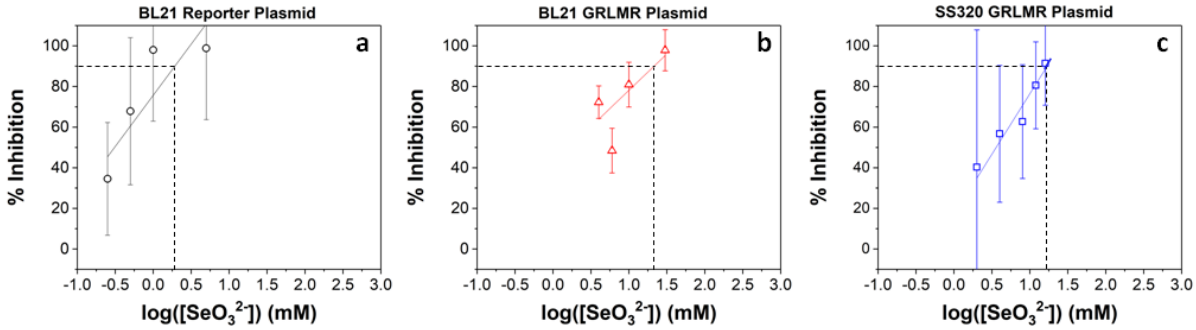

Figure 4.2. IC90 assays reported in percent inhibition vs. selenite concentration a) BL21 E. Coli cell lines with a GFP plasmid b) BL21cells with the GRLMR plasmid c.) SS320 cells with the GRLMR plasmid.

Figure 4.2 shows relative growth inhibition as a function of selenite concentration. The $\log_{10}[SeO_3^{2-}]$ gives a linear concentration dependence for SeO_3^{2-} growth inhibition. This allows determination of the inhibitory concentration of selenite that eliminates 90% of cell growth (IC_{90}). We found an IC_{90} of 21.3±9.8mM under conditions of GRLMR overexpression, whereas an IC_{90} of 1.89±.46mM is observed in a corresponding control experiment. This result is at least somewhat cell-line independent. When GRLMR is recombinantly overexpressed in *E. Coli* SS320, we observe an IC_{90} of 18.3±19.5mM. Even with the large error bars a statistically significant increase in SeO_3^{2-} tolerance is

induced by the presence of the GRLMR plasmid and we believe that the SS320 data is justified due to the similarly observed tolerance in the BL21 cell line.

We note that the presence of recombinantly expressed enzyme results in the liquid cultures taking on the red color characteristic of the red allotrope of zerovalent selenium, whereas cultures grown with SeO_3^{2-} without the recombinantly expressed enzyme do not take on this color. To illustrate this, Figure 4.3 shows cell cultures expressing the GRLMR (left panel) or GFP (right panel) in the presence of SeO_3^{2-} supplementation at 5 mM, after 3 hours of exposure. This 'bulk color' change suggests that the cells expressing the recombinant enzyme may also be forming Se(0) nanoparticles just as we previously observed for the *P. moravenis* strain.

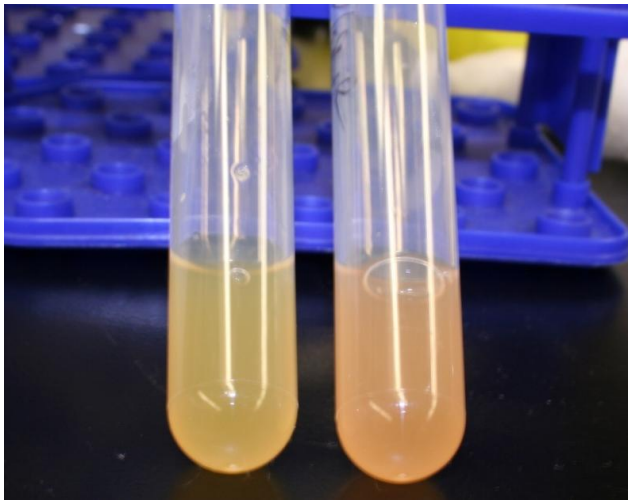

Figure 4.3. Separation of selenium NP growth. BL21 cells with (right) and without (left) GRLMR plasmid after a 3 hour exposure to 5mM selenite supplemented LB.

Examination of cells by SEM revealed the presence of selenium nanoparticles in cells expressing the recombinant enzyme and grown in Se supplemented media. Figure 4.4 shows scanning transmission electron micrographs of glutaraldehyde fixed dry-mounted BL21 *E. coli* cells expressing GFP or GRLMR after growth in SeO_3^{2-} supplemented media. Both GFP and GRLMR cells show dark inclusions, with more inclusions observed in the GRLMR expressing cell line. Electron dispersive spectroscopy (EDS) mapping confirms that the dark inclusions are Se rich for the GRLMR cells, whereas any inclusions observed in GFP expressing cells show no evidence of Se presence. The corresponding EDS spectra

further confirms these conclusions by the presence of signature selenium peaks being present for the GRLMR cells, and the absence of these peak for the GFP cells.

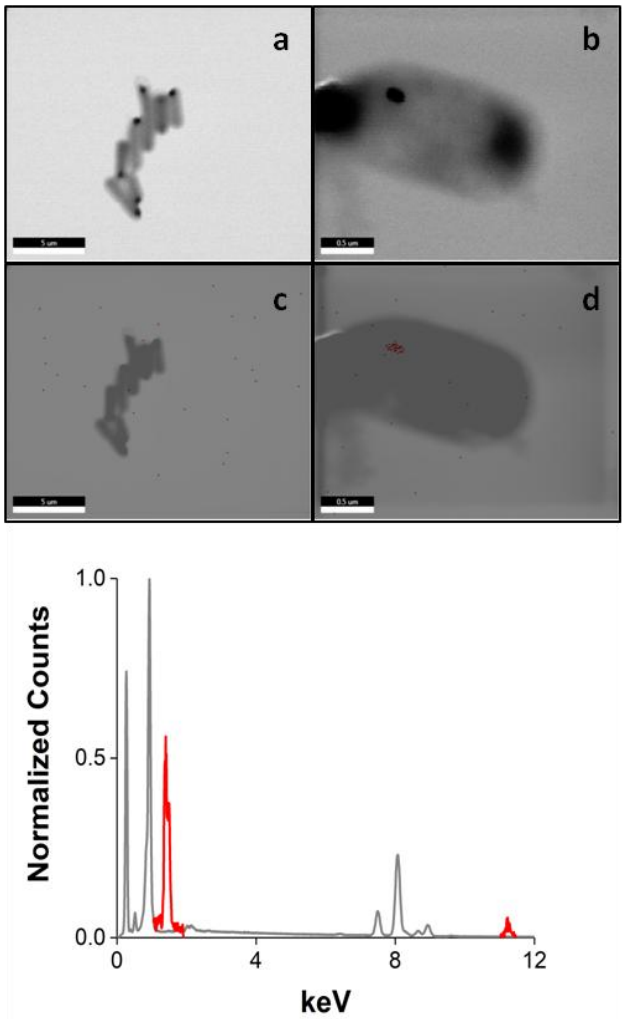

Figure 4.4. SEM images (top) with EDS overlay (middle) of fixed cells after 3 hour exposure to 5mM selenite. a,c) Cells without GRLMR plasmid. b,d) Cells with GRLMR plasmid. Corresponding EDS spectra of cells without GRLMR (grey), and additional peaks from cells with GRLMR plasmid (red) on bottom.

Previously, we observed that some fraction of nanoparticles synthesized by *S. cervisiae* GSHR were associated with the particle fraction.[13] We examined the GRLMR for similar behavior. Selenium particles were synthesized in vitro and were separated from the solution using centrifugation. The analysis of protein content in the solution and the particles were determined by Bradford assay (Bio-Rad). Overall, approximately 10% of the enzyme is

associated with the selenium nanoparticles. This is a smaller fraction than we observed for *S. cervisiae* glutathione reductase (~18%), suggesting that the *P. moravenis* derived enzyme is more efficient at turning over or releasing the particles that they create. Overall, this contributes to the picture of the GRLMR being specialized for conveying Se tolerance.

Table 4.3. Key Glutathione Pocket Residues.

Enzyme	**PM MTLR**	**PF GSHR**	**EC GSHR**	**SC GSHR**	**HS GHSR**
Key Product	α-Ser	α-Ser	α-Met	α-Cys	α-Met
Binding Site	βL-Lys	βL-Lys	βL-Lys	βL-Lys	βL-Lys
Residues	βR-Glu	βR-Glu	βR-Lys	βR-Asn	βR-Ser

Differences in the product/substrate binding pocket of this family of enzymes may underlie any observed differences in substrate specificity and enzyme activity. The key residues in the product/substrate binding area of GSHR are shown in Table 4.3, and models of this are shown in S.3. Structural alignment between GRLMR and *P. fluorescines* reveals an RMSD of 1.71 Å for the full enzyme and 1.56 Å for the product/substrate binding pocket. These values show the largest deviation between any of the enzymes considered here, but to the best of our knowledge no crystal structure of a *Pseudomonas* glutathione reductase has been obtained which would affect the generated structure models.

The product/substrate binding pocket for GSHR contains a set of evolutionarily conserved residues, most notably including a cysteine that is implicated in glutathionylation regulatory mechanisms. There are three residues that dominate the binding interaction, one on an α-helix, and two on parallel β-strands (βL, βR). Comparing our *Pseudomonas* enzymes we see that they contain the same key residues; α-Ser, βL-Lys, βR-Glu. (Figure 4.5.) [30]

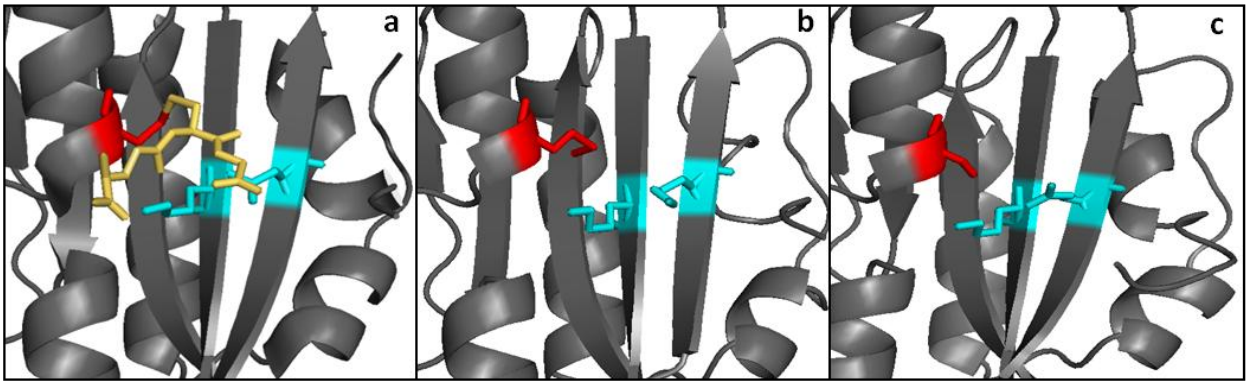

Figure 4.5. Red- α residue, Teal- β residues, Yellow- GSH a) Yeast GHSR substrate binding pocket with bound GSH b) E. Coli GSHR substrate binding pocket c.) GRLMR substrate binding pocket.

This absence of a sulfur-containing residue (Figure 4.1) in the *P. moravenis* GRLMR, suggests that the enzyme is not subject to the glutathionylation regulatory mechanism well established for canonical glutathione reductase enzymes such as *S. Cervisiae* glutathione reductase. Glutathionylation of enzymes is a common post translation modification for proteins in signaling pathways and survival gene modification.[31–34] This reversible post-translation modification is the binding of glutathione to an unpaired cysteine residue.[35] Such modification alters enzyme activity, presumably as a regulation mechanism.[36,37] In the case of *S. Cervisiae* GSHR, glutathionylation at C239 (Figure 4.5) inhibits the enzyme. Chemically blocking the glutathionylation pathway is shown to increase GSHR activity by a factor of 2.1.[38] Overall, the absence of the possibility of a glutathionylation regulation mechanism for the GRLMR enzyme suggests that it is distinct from other GSHR enzymes.

The selenium metabolism literature highlights several examples of species within the *Pseudomonas* genus with remarkable tolerance to Se. In many cases GSHR enzymes are implicated in the tolerance. GSHR was responsible for reducing selenite and tellurite to insoluble NP's using the O-2 strain of *Pseudomonas maltophilia*;[39] GSHR and thioredoxin reductase are responsible for selenite and selenate reduction in *Pseudomonas seleniipraecipitansI.* [40–43] The highly conserved sequence across species within the *Pseudomonas* genus, including conservation in the product/substrate binding pocket, is suggestive that the ability to handle normally toxic amounts of SeO_3^{2-} may be a general feature of the *Pseudomonas* genus. This Se tolerance may arise from the nature of GSHRs in this genus.

4.4 Conclusions

In summary, we have characterized a glutathione reductase-like metalloid reductase (GRLMR) from the bacterium *Pseudomonas moraviensis* stanleyae. Kinetic studies showed an overall decrease in substrate affinity for the GRLMR relative to the *S. cervisiae* GSHR, but an overall increased affinity for GS-Se-SG over GSSG. Transportability of the gene was tested by transforming lab strain *E. Coli* with GRLMR. Selenite tolerance increased ten-fold compared to cells without the gene, and the formation of elemental red selenium when GRLMR was present. SEM/EDS further confirmed this by showing selenium particles associated with cells containing the gene. Product association experiments showed a decrease in product retention when compared to *S. cervisiae* GSHR, which ultimately allows for increased product release and contributes to the overall Se tolerance.

4.5 Materials and Methods

Identification/Isolation

An LB agar plate with colonies of the original *P. moravenis* cell line was submitted for full genome sequence. The DNA sequence from the most closely related enzyme identified by MALDI was used to identify the sequence of our enzyme of interest. This sequence was cloned into a pD441-CH *E. Coli* vector and a standard heatshock protocol was used to transform BL21 *E. Coli*.

Standard protein purification was conducted by growing cells in 1L of LB to an optical density at 600nm ($O.D._{600}$) of .6 and inducing protein expression with 1mM IPTG for 2 hours. Cells were collected and re-suspended in 25 ml of lysis buffer and lysed by tip sonication. The soluble cell lysate was collected and nickel-agarose beads were used to isolate and wash our expressed protein.

GS-Se-SG Synthesis

Protocol from Ganther was followed for the synthesis of the selenodiglutathione.[26] 400umoles of $HNaSeO_3$ was added to 24 ml of .1 M HCl and cooled to 4^oC. Another solution of .1M GSH was cooled to 4^oC and added quickly to the selenite solution. The mixture was allowed to react at 4^oC for 20 minutes. 2.5ml of 2M NaOAc was added to obtain a final pH of 4.5. A C18 column was used to separate the

products using pH 2.0 HCl. TLC was used to check the contents of lyophilized fractions. Isolated GS-Se-SG was identified and the amount quantified using the UV-Vis absorption at 263 nm. (S.4)

Km

1 ml reactions were conducted in 1x PBS with .1mM NADPH, and 15ug of either purified enzyme or *S. cervisiae* GSHR purchased from Sigma. Substrates tested were GSSG, GS-Se-SG, and selenite. Their concentrations were varied between reactions and the depletion of the NADPH peak at 340 nm was monitored every 2 seconds after the contents were mixed.

Transportability

IC_{90}'s were determined by standard plating experiments. In short a culture of BL21 cells containing either a plasmid with the GRLMR or a generic reporter gene were grown overnight in LB at 37^{o}C. The following morning 100 ul of this starter culture were added to 2.5ml of fresh LB and grown for roughly 2.5 hours to reach an $O.D._{600}$ of .6. Various amounts of selenite were added to each culture and exposure was continued for 24 hours. After exposure the cells were diluted 10^6 fold and 20 uL of each dilution was plated in triplicate on 1x Kanamycin LB-Agar. Plates were put in the oven at 37^{o}C and colonies were grown overnight and colonies were counted the following day.

STEM

3 mL of BL21 cells containing either a metalloid reductase gene or GFP reporter gene were grown separately in 10 mL culture tubes overnight containing LB medium (Teknova) supplemented with Kanamycin at 25ug/ml. The following morning the culture was added to a 125 mL Erlenmeyer flask containing LB medium supplemented with Kanamycin (25ug/ml). The cells were grown for 2.5 hours and 100 mM Na_2SeO_3 (Alfa Aesar, 98+%) was added to reach a final concentration of 5mM. The cells were collected by centrifuging for 20 minutes at 4000 rpm and 4 ^{o}C after 3 hours of growth with selenite. Cells were washed with 20mM Tris (pH 7.4) (Fischer) three times followed by resuspension in 1 ml of fixing solution (2% gluteraldehyde (25% Sigma-Aldrich) and 2.5% formaldehyde); the fixing solution was alloed to react for 12 hours at 4 ^{o}C. The fixing solution was centrifugation and the pellet was washed five times in 20mM Tris (pH 7.4). The cells were resuspended in 1 ml 20 mM Tris (pH 7.4). Aliquots (4 uL)

were mounted on 400 mesh Cu grids with 50 nm C coating and washed two times with H_2O. Dry-mounted cells on TEM grids were loaded onto a STEM holder. STEM images were taken on a JEOL JSM-6500-F Scanning Electron Microscope at an accelerating voltage of 15 kV.

EDS

EDS was performed on *P. moreviensis* Stanleyae cells in the SEM as described above. EDS was collected on a Noran System 7 X-ray Microanalysis detector with a time interval of 1s.

REFERENCES

1. Harrison, P. M. *Biochem. Educ.* **1986,** 14**,** 154–162.

2. Kolinko, I. *et al. Nat. Nanotechnol.* **2014,** 9**,** 193–197.

3. Müller, W. E. G. *et al. Gene* **2007,** 395, 62–71.

4. J. Carter, C. *et al. J. Mater. Chem.* **2009,** 19, 8320–8326.

5. Slocik, J. M., Kuang, Z., Knecht, M. R. & Naik, R. R. *ChemPhysChem* **2016,** 17, 3252–3259.

6. Yeh, H.-C., Sharma, J., Han, J. J., Martinez, J. S. & Werner, J. H. *Nano Lett.* **2010,** 10, 3106–3110.

7. Klug, M. T. *et al. Chem. Mater.* **2017,** 29, 6993–7001.

8. Choi, S., Dickson, R. M., Lee, J.-K. & Yu, J. *Photochem. Photobiol. Sci.* **2012,** 11, 274–278.

9. Wang, Q., Mercogliano, C. P. & Löwe, J. *Struct. Lond. Engl. 1993* **2011,** 19, 147–154.

10. Castruita, M. *et al. Appl. Environ. Microbiol.* **2006,** 72, 2918–2924.

11. Brutchey, R. L. & Morse, D. E. *Chem. Rev.* **2008,** 108, 4915–4934.

12. P. Smith, G., J. Baustian, K., J. Ackerson, C. & L. Feldheim, D. *J. Mater. Chem.* **2009,** 19, 8299–8306.

13. Ni, T. W. *et al. Nanoscale* **2015,** 7, 17320–17327.

14. Lian, P. *et al. Biochemistry (Mosc.)* **2014,** 53, 7211–7222.

15. Fox, B. S. & Walsh, C. T. *Biochemistry (Mosc.)* **1983,** 22, 4082–4088.

16. Li, X. & Krumholz, L. R. *J. Bacteriol.* **2009,** 191, 4924–4933.

17. Freedman, Z., Zhu, C. & Barkay, T. *Appl. Environ. Microbiol.* **2012,** 78, 6568–6575.

18. Pugin, B. *et al. Appl. Environ. Microbiol.* **2014,** 80, 7061–7070.

19. Otwell, A. E. *et al. Environ. Microbiol.* **2015,** 17, 1977–1990.

20. Scott, D., Toney, M. & Muzikár, M. *J. Am. Chem. Soc.* **2008,** 130, 865–874.

21. Wang, Z. *et al. BMC Genomics* **2010,** 11, 726.

22. Ewing, B., Hillier, L., Wendl, M. C. & Green, P. *Genome Res.* **1998,** 8, 175–185.

23. Arscott, L. D., Gromer, S., Schirmer, R. H., Becker, K. & Williams, C. H. *Proc. Natl. Acad. Sci. U. S. A.* **1997,** 94, 3621–3626.

24. Mittl, P. R. & Schulz, G. E. *Protein Sci. Publ. Protein Soc.* **1994,** 3, 799–809.

25. Kelley, L. A., Mezulis, S., Yates, C. M., Wass, M. N. & Sternberg, M. J. E. *Nat. Protoc.* **2015,** 10, 845–858.

26. Ganther, H. E. *Biochemistry (Mosc.)* **1971,** 10, 4089–4098.

27. Mavis, R. D. & Stellwagen, E. *J. Biol. Chem.* **1968,** 243, 809–814.

28. Painter, E. P. *Chem. Rev.* **1941,** 28, 179–213.

29. Hunter, P. *EMBO Rep.* **2008,** 9, 15–18.

30. Yu, J. & Zhou, C.-Z. *Proteins Struct. Funct. Bioinforma.* **2007,** 68, 972–979.

31. Grek, C. L., Zhang, J., Manevich, Y., Townsend, D. M. & Tew, K. D. *J. Biol. Chem.* **2013,** 288, 26497–26504.

32. Sullivan, D. M., Wehr, N. B., Fergusson, M. M., Levine, R. L. & Finkel, T. *Biochemistry (Mosc.)* **2000,** 39, 11121–11128.

33. Townsend, D. M. *et al. Mol. Pharmacol.* **2006,** 69, 501–508.

34. Fiaschi, T. *et al. J. Biol. Chem.* **2006,** 281, 22983–22991.

35. Hill, B. G. & Bhatnagar, *J. Mol. Cell. Cardiol.* **2012,** 52, 559–567.

36. Humphries, K. M., Juliano, C. & Taylor, S. S. *J. Biol. Chem.* **2002,** 277, 43505–43511.

37. Townsend, D. M. *et al. Cancer Res.* **2009,** 69, 7626–7634.

38. Stepovaya, E. A. *et al. Biochem. Mosc. Suppl. Ser. B Biomed. Chem.* **2016,** 10, 235–239.

39. Blake, R. C. *et al. Environ. Toxicol. Chem.* **1993,** 12, 1365–1376.

40. Hunter, W. J. & Manter, D. K. *Curr. Microbiol.* **2009,** 58, 493–498.

41. Kora, A. J. & Rastogi, L. *J. Environ. Manage.* **2016,** 181, 231–236.

42. Lortie, L., Gould, W. D., Rajan, S., McCready, R. G. L. & Cheng, K.-J. *Appl. Environ. Microbiol.* **1992,** 58, 4042–4044.

43. Avendaño, R. *et al. Sci. Rep.* **2016,** 6, 37155.

CHAPTER 5

Supplemental Information

5.1 Chapter 2 Supporting Information

Reagents

The following chemicals were purchased from Sigma-Aldrich and used without further purification: Gold (III) chloride trihydrate ($HAuCl_4$, ≥49.0% Au basis), L-glutathione reduced (GSH, ≥98.0%), Boric Acid (H_3BO_3, ≥99.5%), Methanol (CH_3OH, ≥99.8%), N,N,N,'N'-Tetramethylethylenediamine (TEMED, ≥99%), N-(3-Dimethylaminopropyl)-N'-ethylcarbodiimide (EDC, 98%), polyvinylpyrrolidone (PVP, 40MW), and Ammonium Persulfate (APS, ≥98%). The following chemicals were purchased from TCI America and used without further purification: N^{ε}-carbobenzoxy-L-lysine (N^{ε}-Cbz-L-lysine, >98.0%). Other reagents were purchased from Alfa Aesar, Thermo Scientific, and Sigma-Aldrich and used without further purification. Lithium sulfate (Li_2SO_4, ≥98.5%). Trimethylamine N-oxide (TMAO, ≥98%). Sodium Thiosulfate Anhydrous ($Na_2S_2O_3$, ≥99%), Sodium Hydroxide (NaOH, ≥99%). Tris Hydochloride ($C_4H_{11}NO_3$, ≥99%), Ethanol (EtOH, ≥88%), Ammonium Acetate (NH_4OAc, ≥99%). L-Ascorbic Acid ($C_6H_8O_6$, ≥99%) and Nitric Acid (HNO_3, 70% Aqueous Solution) were purchased and used without further purification from Macron Chemicals. Ethylenediamine Tetraacetic Acid (EDTA, ≥99%) and Sodium Borohydride ($NaBH_4$, ≥96%) were purchased and used without further purification from EMD Millipore. Acrylamide/Bis Solution (40%, 19:1) was purchased and used without further purification from Bio-Rad.

Protein Crystal Preparation

Full sequence information as well as expression and purification protocols for protein CJ (Genebank ID: cj0420, Protein Data Bank code: 2fgs) can be found in the published supplemental information here.[1] CJ was crystallized overnight by sitting drop vapor diffusion in 3.2 to 3.6 M ammonium sulfate and 0.1 M BIS-TRIS at pH 6.5. Crystals were then transferred to a drop of 4.2 M

trimethylamine N-oxide (TMAO) and 50 mM imidazole to wash the crystal and equilibrate to the crosslinking solution. Crystals were crosslinked in 4.2 M TMAO, 50 mM imidazole, and 100 mM 1-Ethyl-3-(3-dimethylaminopropyl) (EDC). After two hours in the crosslinking solution, incomplete crosslinks were quenched in 50 mM borate at pH 10 for 15 mins. After crosslinking and washing, crystals retained smooth, hexagonal morphology and clear color.

Oxidoreductase protein (Protein Data Bank code: 3oc4) from *Enterococcus faecalis* was selected from a scan of the Protein Data Bank for proteins that crystallize with large pores. It was expressed in pSB3 in *E. coli* BL21 (DE3) pLySs using a glucose/lactose induction system at 17 °C for 36 hours.[2] The cells were lysed by sonication and purified via immobilized metal affinity chromatography. Purified protein was buffer exchanged into 150 mM NaCl, 10 mM HEPES, and 10% glycerol at pH 7.5 and characterized with SDS-Page.

3oc4 was also crystallized overnight by vapor drop diffusion in 1.5 to 2 M sodium formate and 0.1 M sodium acetate at pH 4.6. Crystals were washed and equilibrated in a drop of 4.2 M TMAO and 50 mM imidazole for 10 mins. Next, crystals were crosslinked in 4.2 M TMAO, 50 mM imidazole, and 100 mM EDC. After two hours in the crosslinking solution, the crystals were quenched in 50 mM borate at pH 10 for 15 mins. After crosslinking and washing, crystals retained smooth, elliptical morphology and clear to slightly yellow color.

Gold synthesis

$Na_3Au(S_2O_3)_2$ was synthesized using previously published methods.[3] Approximately 2 ml of 15 M NaOH was added dropwise to 3.65 ml of 0.1 M $HAuCl_4$ dissolved in H_2O until a white precipitate formed at approximately pH 8.5. After stirring for 5 mins, 10.16 mL of $Na_2S_2O_3$ (5.18 g) dissolved in water was added at once and was allowed to continue stirring for 5 mins. Approximately 1.8 ml of 4 M HNO_3 was added dropwise until a red color change was no longer seen after each drop addition. The reaction was filtered and washed x4 with 100 mL EtOH. The precipitate was dissolved in 20 mL H_2O followed by EtOH precipitation using 80 mL of solvent. The precipitate was filtered and washed x3 with 80 mL of EtOH.

$Au_{25}(GSH)_{18}$ was synthesized using previously published methods.[4] 98.6 mg $HAuCl_4$ were dissolved in 50 mL of MeOH. 0.3062 g of reduced glutathione (GSH) were added to the solution and stirred until colorless. The contents were placed in an ice bath for 30 mins along with 12 mL of 0.2 M $NaBH_4$. The $NaBH_4$ was added rapidly to the solution under vigorous stirring. The reaction was allowed to stir for 1 hr. The contents were spun at 4000 rpm for 10 mins. The supernatant was discarded and pellets were dispersed in 2 mL of H_2O followed by the addition of 200 uL of 5 M NH_4OAc and 48 mL MeOH. After spinning at 4000 rpm for 10 mins the supernatant was again discarded. The previous steps were repeated x2 and the pellet was allowed to dry. The clusters were further separated using 24% Tris-Borate-EDTA (TBE) buffered polyacrylamide gel electrophoresis (PAGE) run at 125 V for 4.5 hrs.

$Au_{25}(NTA)(GSH)_{17}$ was synthesized using a common ligand exchange reaction. Briefly dried and purified $Au_{25}(GSH)_{18}$ was dissolved in H_2O and five equivalents of HS-NTA was added. This reaction was allowed to shake for 7.5 minutes.[5] The products were then precipitated using MeOH and 200 µL of 5 M NH_4OAc. After collection using centrifugation the precipitate was dried under reduced pressure.

Gold growth with chloroauric acid

The following protocol was used to encourage maximum gold growth within the crystal pores. Gold nanorods can be obtained using this protocol with or without first adsorbing a gold nanoparticles ($Au_{25}(GSH)_{17}NTA$) into the pores as nucleation sites. Seeded or unseeded crystals were placed in 10 mM chloroauric acid ($HAuCl_4$) for 10 to 30 mins or until the crystals turned a bright yellow color. We hypothesize there are electrostatic interactions that cause adsorption of Au^{+3} within the crystal. Next, crystals were moved to 10 mM ascorbic acid until black (Fig 5.1.1). Crystals typically turn black within 10 mins, but may darken for up to 24 hrs.

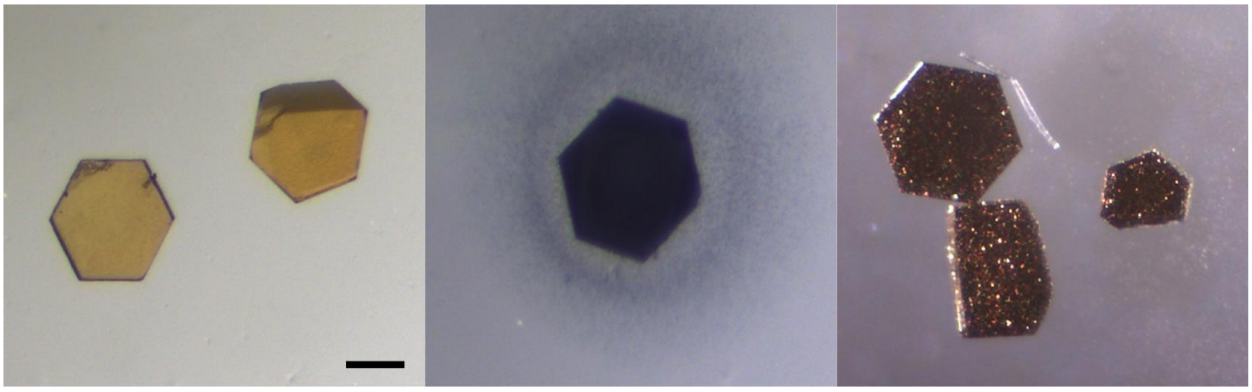

Figure 5.1.1. (a) A CJ protein crystal after loading in 10 mM $HAuCl_4$ for 10 mins. (b) A CJ protein crystal after transfer to 10 mM ascorbic acid for 1 hr. (c) CJ crystals grown by the same method but viewed with an overhead brightfield light to better display the complete presence of metallic gold. Scale bar is 100 um.

We investigated the effects of loading time of gold seeds (Au_{25}) and Au^{+3} ions on the amount of growth within the crystal. In summary, with no seed present, crystals may sometimes turn completely black by eye, but typically look more grey with particles crashed out in the surrounding well. When gold seeds were loaded into the crystal for only 5 mins before growth, the crystal took longer (up to overnight) to turn completely black. Whereas crystals that were loaded with Au_{25} for 1 hr prior to growth typically turned fully black within 20 mins of placement in 10 mM ascorbic acid. Additionally, the length of chloroauric loading had an effect on overall growth. When the length of loading time was increased to 16 hrs, crystals did not turn completely black in any case during reduction (independent of seed loading time). Additionally more aggregation and nucleation within the drop was seen.

We also investigated the effect of $NiSO_4$ (used for locking the nitrilotriacetic acid ligand on the Au_{25} particle to the Histidine tag on the crystal) on spontaneous nucleation. As we had noticed that with this method, Au_{25} was not needed to produce nucleation. Without $NiSO_4$ present, spontaneous nucleation could be slowed, but not fully prevented, so $NiSO_4$ was used in future experiments to preserve the specific attachment of the gold seed within the crystal pore.

Additionally, we explored the effect of pH on overall gold growth. Most experiments were carried out at pH 7.0. When the pH was changed to 9.0, much less overall growth occurred. We

hypothesized that this is because some gold structures are more stable at higher pH. At pH 5.0, much more aggregation occurred within the well, but did not aid in overall growth within the crystal.

In some early attempts at complete gold growth within the crystal we attempted to create a growth solution which contained both chloroauric acid and ascorbic acid. We hypothesized that when a seeded crystal was placed in this growth solution, rod formation and particle growth would preferentially occur within the crystal pores in the presence of a seed, locked in place by Ni(II). However, even upon changing solution concentrations, we found only that uncontrolled growth occurred within the well and often at the surface of the crystal, suggesting some favorable electrostatics between the crystal and the soluble gold (Fig. 5.1.2).

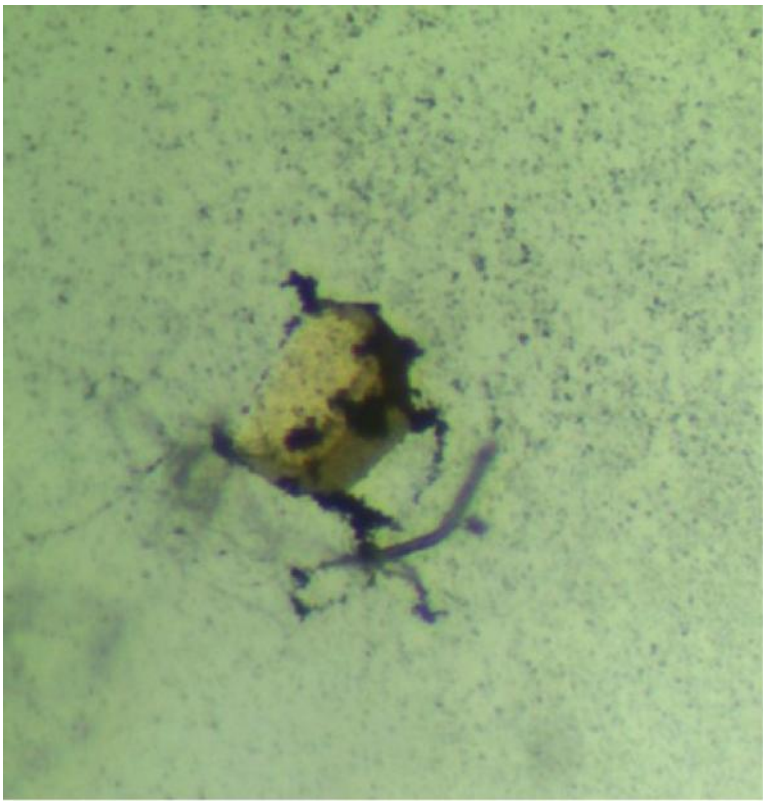

Figure 5.1.2. An Au_{25} seeded CJ crystal after 1 hr of exposure to a mixture of 5 mM $HAuCl_4$ and 5 mM ascorbic acid. Crystal is approximately 300 um in diameter at its widest point.

We determined that multiple rounds of growth can be performed to encourage further darkening of the crystal and presumably more growth within the pores. Once a crystal had been through one round of growth (Au25, HAuCl4, ascorbic acid), it was placed back into a fresh drop of HAuCl4, then again into

ascorbic acid. This "stepwise" growth caused darker crystals by eye after multiple rounds (Fig. 5.1.3), but we found that the rods present were no longer than those that could be produced by one round of growth. We suspect that prolonged exposure to the growth solutions may cause some etching of the longest, most fragile rods (Fig. 5.1.4).

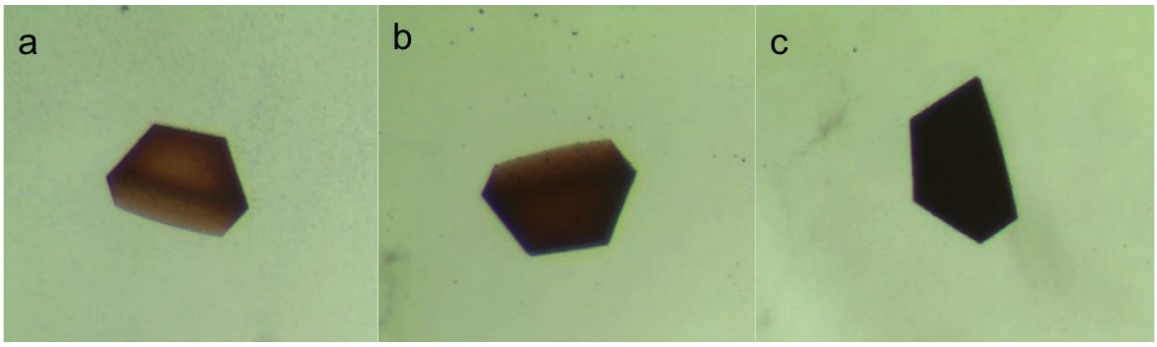

Figure 5.1.3. A CJ crystal after (a) one, (b) two, and (c) three rounds of growth with $HAuCl_4$ and ascorbic acid. Crystals are approximately 300 um in diameter at their longest point.

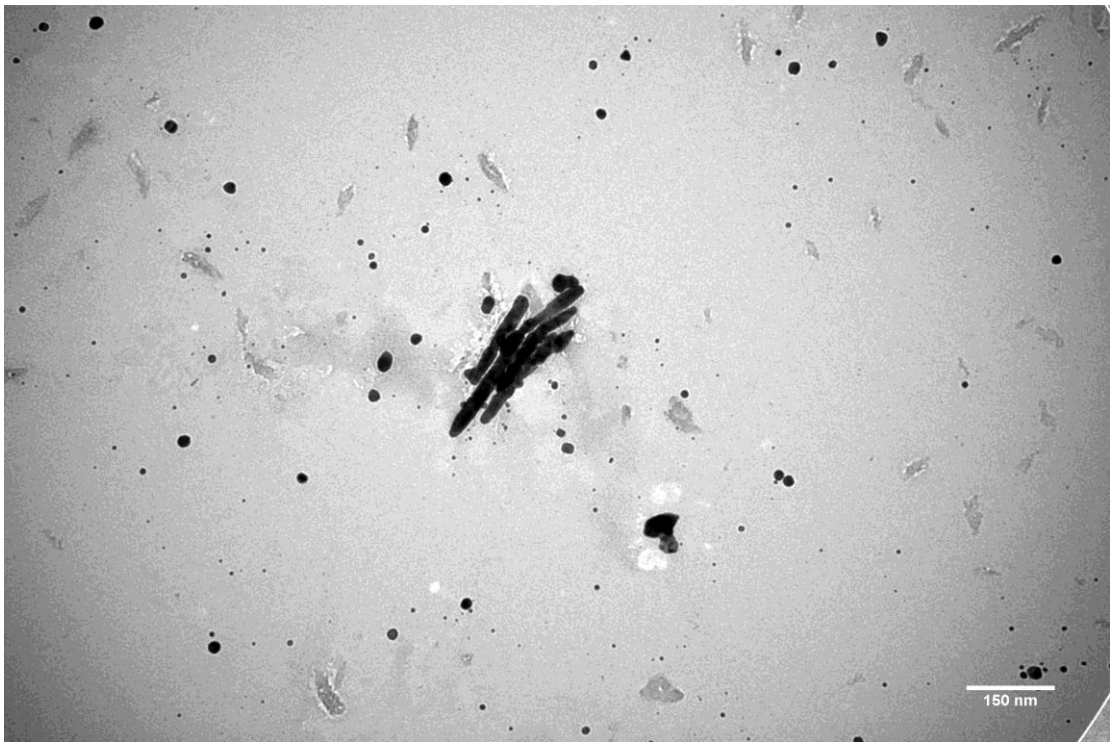

Figure 5.1.4. Transmission electron microscopy of structures resulting when a CJ crystal is subjected to six "rounds" of growth and then dissolved. Scale bar is 150 nm.

To confirm some of these anecdotal growth observations made by optical microscope (regarding the effect of Au_{25} and $HAuCl_4$ loading times), we dissolved many crystals and viewed the resulting

structures under transmission electron microscopy. Figure 5.1.6 shows the differences in gold products with and without the presence of Au_{25} as a nucleation point and with and without ascorbic acid as a reducing agent. These results show that although gold nanoparticles (and sometimes rods) are formed in the absence of a gold seed, rods were more plentiful and longer when a seed is present. Additionally, a lack of reducing agent leads to almost no particle formation.

Figure 5.1.5 depicts via optical microscopy the case in which no chloroauric acid is added to the crystal (Au_{25} seeds within the crystal are simply exposed to ascorbic acid). Here there is no color change by eye and only Au_{25} particles visible by TEM.

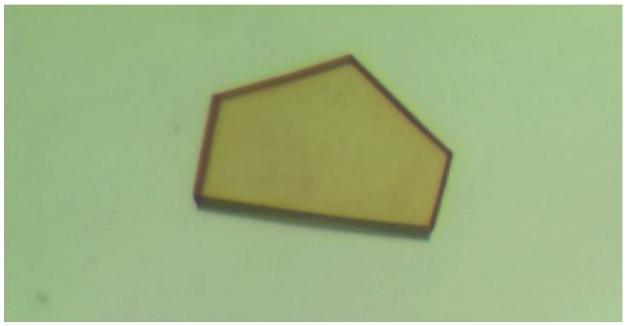

Figure 5.1.5. A CJ crystal loaded with Au_{25} seeds and exposed to 10 mM ascorbic acid for 16 hrs results in no color change, thereby no apparent particle growth or rod formation. The crystal is approximately 300 um in diameter at its widest point.

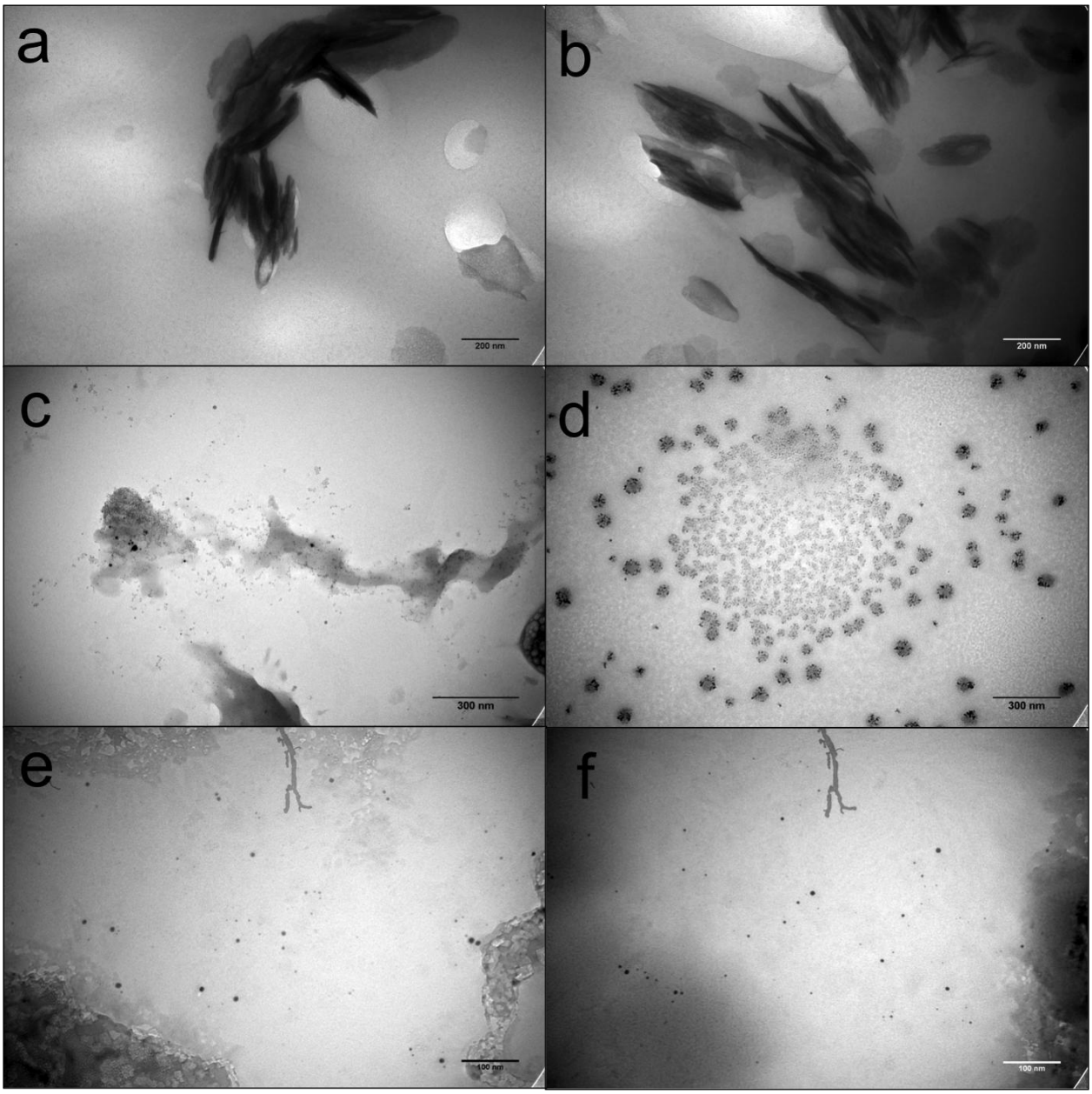

Figure 5.1.6. TEM of the resulting gold structures when a (a & b) seeded or (c & d) unseeded CJ crystals are grown in 10 mM $HAuCl_4$ for 10 mins, transferred to a drop of 10 mM ascorbic acid for 1 hr, and then dissolved. (e & f) TEM of seeded CJ crystal loaded with 10 mM $HAuCl_4$ for 10 mins and then dissolved shows that reduction is required for nanoparticle growth. Scale bars are (a & b) 200 nm, (c & d) 300 nm, and (e & f) 100 nm.

Additionally, we confirmed our visual observation that leaving a CJ crystal soaking in $HAuCl_4$ overnight before reduction may prevent rod formation. We believe this is because more self-nucleation occurred, including outside the crystal, which created only particles. Figure 5.1.7 shows typical TEM results from a normal versus extended $HAuCl_4$ loading time.

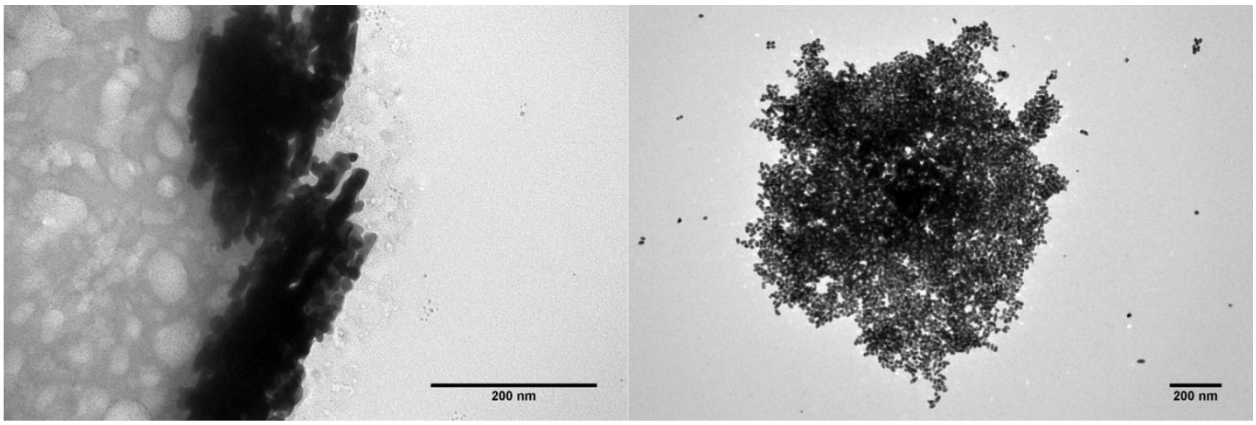

Figure 5.1.7. Left: A gold structures within a CJ crystal loaded with $Au_{25}(GSH)_{17}NTA$ for 30 mins, $HAuCl_4$ for 10 mins, reduced by ascorbic acid, then dissolved for imaging. Right: The results when the $HAuCl_4$ loading time is increased to 16 hrs. Scale bars are 200 nm.

The overall quantity of seeds present in the crystals before nucleation affected the products observed. We demonstrated this effect by varying the Au_{25} loading time which can be seen in Figure 5.1.8. The sample with a longer Au_{25} loading time appears to have only made smaller particles, while the sample with a shorter Au_{25} loading time formed larger particles and rods with low aspect ratios. We believe the results of these experiments are caused by altering the amount of nucleation sites for growth. The longer loading time of the seed will result in more available seed sights once nucleation is initiated in the growth step, ultimately leading to more particles. When a short seed load time is used there may be less available nucleation sites leading to large particles and more rod formation.

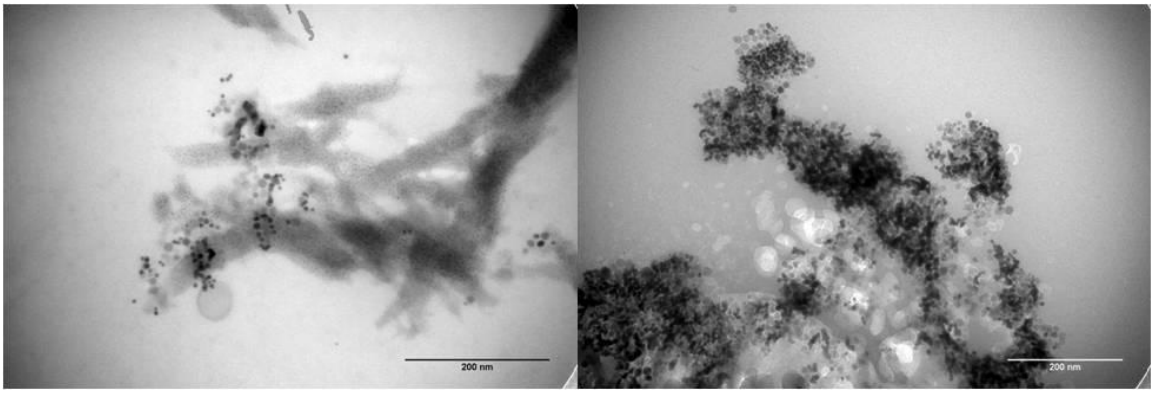

Figure 5.1.8. Left: CJ crystals load with Au_{25} seeds for 30 mins before gold growth, scale bar is 200 nm. Right: CJ crystals load with Au_{25} seeds for 16 hr before gold growth, scale bar is 200 nm.

Apart from looking at seed loading time effects we also carried out an experiment in which we varied the loading time of $HAuCl_4$ prior to reductant addition. 1, 3, and 4 minute, 10 mM $HAuCl_4$ soaking times were carried out and the resulting products after crystal dissolving can be seen in Figure S9. No images were obtained for the 1 minute Au^{3+} soak sample due to the lack of any products on the TEM grid. The 3 min Au^{3+} soak sample showed the formation of particles with an average diameter of 8.8 nm with a standard deviation of 2.9 nm (n=75). Four minutes of Au^{3+} soak time showed the development of rods with an average width of 25.0 nm with a standard deviation of 8.5 nm (n=33) and an average length of 79.8 nm with a standard deviation of 33.1 nm (n=34). In general, the longer Au^{+3} loading time resulted in the presence of more gold nanostructures.

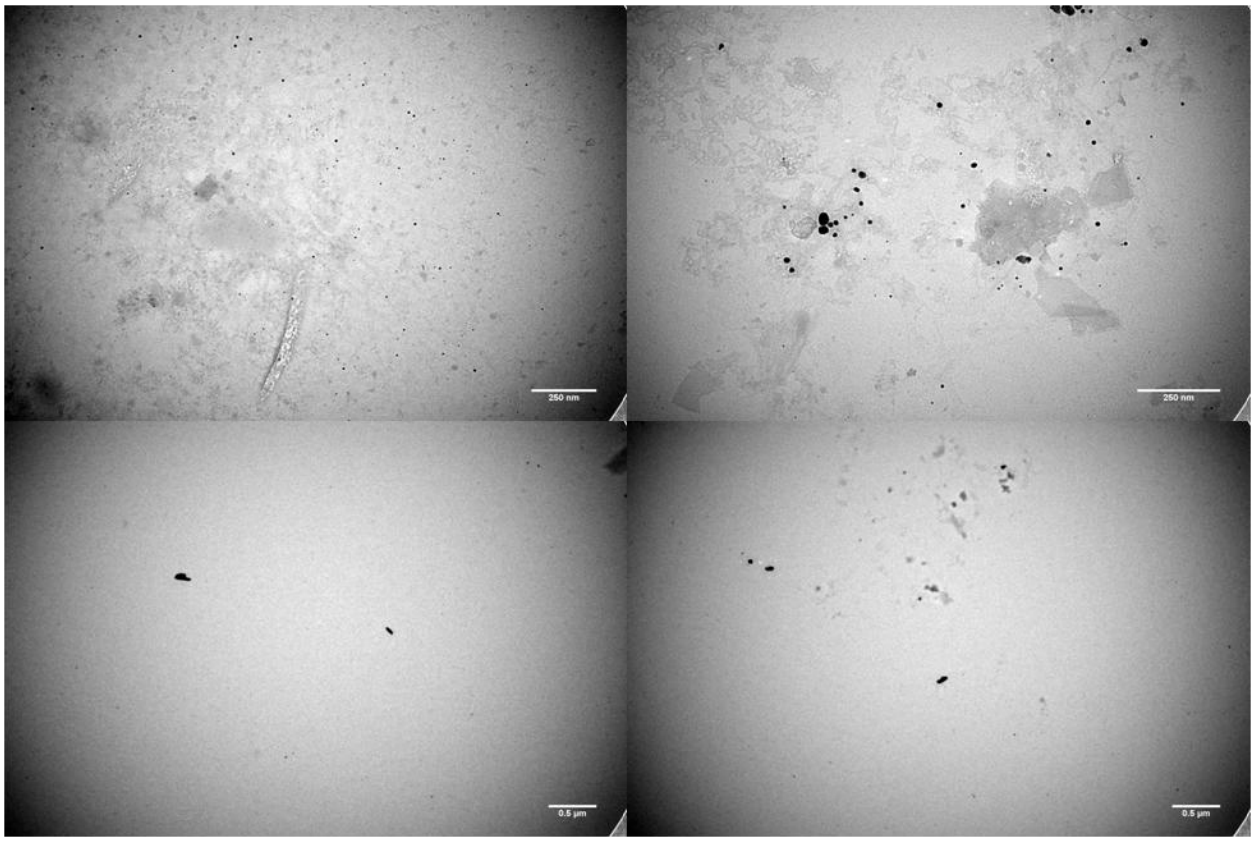

Figure 5.1.9: Top Row: Gold structures resulting from a 3 minute $HAuCl_4$ loading time. Bottom Row: Gold structures resulting from a 4 minute $HAuCl_4$ loading time.

Although there was significant variation between trials, this method of growth produced the longest overall rods we saw (870 nm). There were numerous rods between 500 and 700 nm in length. Possible reasons for the variability in products include impurities in the well that may provide nucleation

sites and variability in the chloroauric acid samples. Figure S10 shows some examples of the types of structures we saw from this protocol. Panels a and b are high resolution transmission electron microscopy images of some of the longer rods grown in CJ crystals. Of note in panel b are the perpendicular segments that connect the four rods. CJ crystals have lateral pores that may account for this attachment (Fig. 5.1.10). In panels c and d, there are many nanoparticles of varying sizes surrounding the rods. Panel e shows an only partially dissolved crystal still surrounding gold nanorods. Panel f shows some of the shorter rods produced by this growth method, and illustrates the bundles of rods that tend to form when the crystal is dissolved.

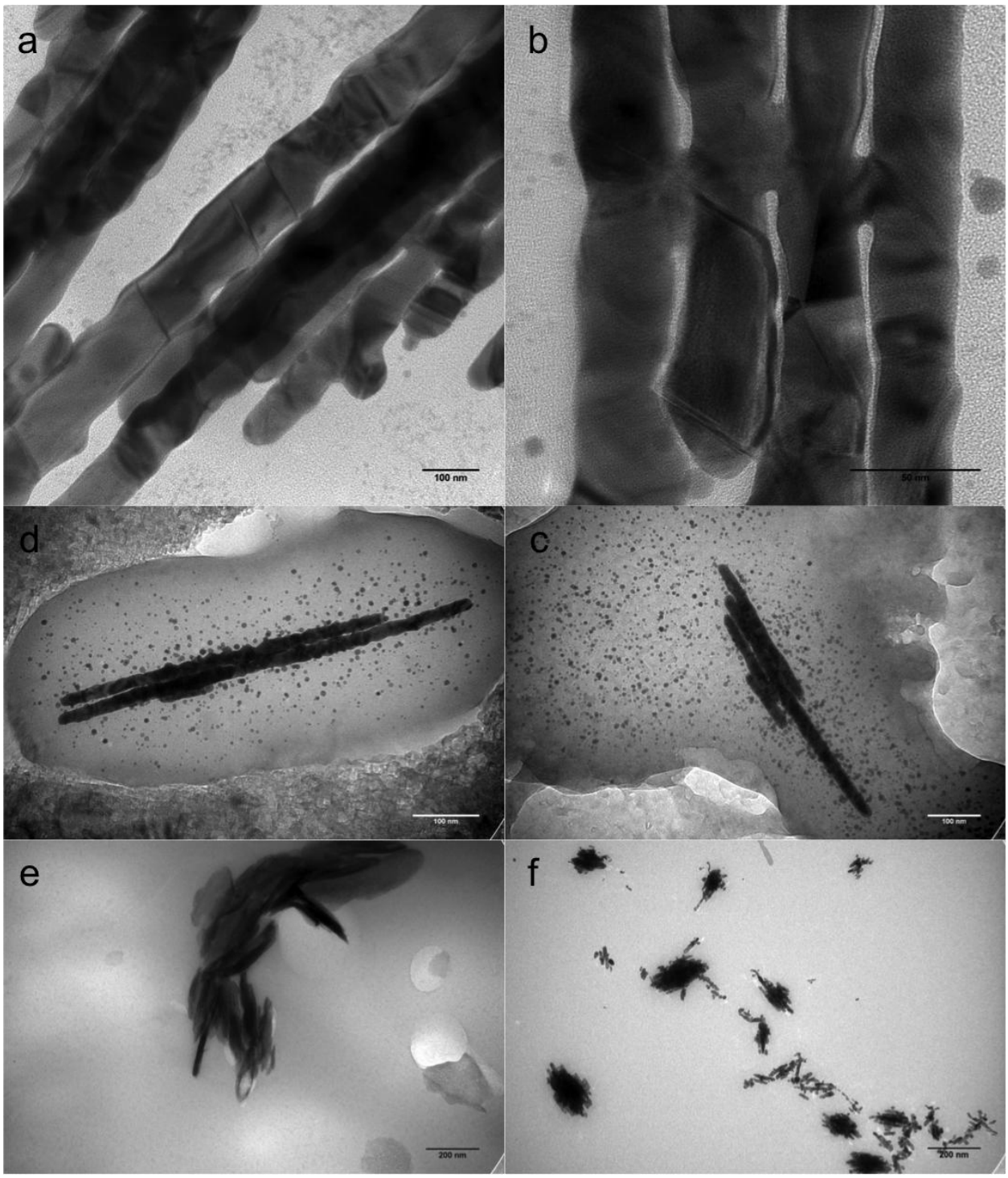

Figure 5.1.10. TEM of dissolved CJ crystals after seeded growth by $HAuCl_4$ and ascorbic acid. (a & b) High resolution TEM. Scale bar (a) 100 nm (b) 50 nm. Scale bar (c & d) 100 nm. Scale bar (e & f) 200 nm.

To demonstrate the versatility of this growth method, we grew gold structures within crosslinked CJ protein crystals using two other "seed" particles as nucleation sites: $Au_{102}(pMBA)_{44}$ and 5 nm diameter

gold nanoparticles (5nm AuNP) with tannic acid surface ligands. In both cases, the seed particle was allow to adsorb into the crystal before transfer to 10 mM $HAuCl_4$, then 10 mM ascorbic acid. Color change was seen in 1 hr, suggesting the presence of larger gold structures within the crystals. The 5nm AuNP seed also showed good control of growth between a seeded and unseeded crystal (Fig. 5.1.11 and 5.1.12).

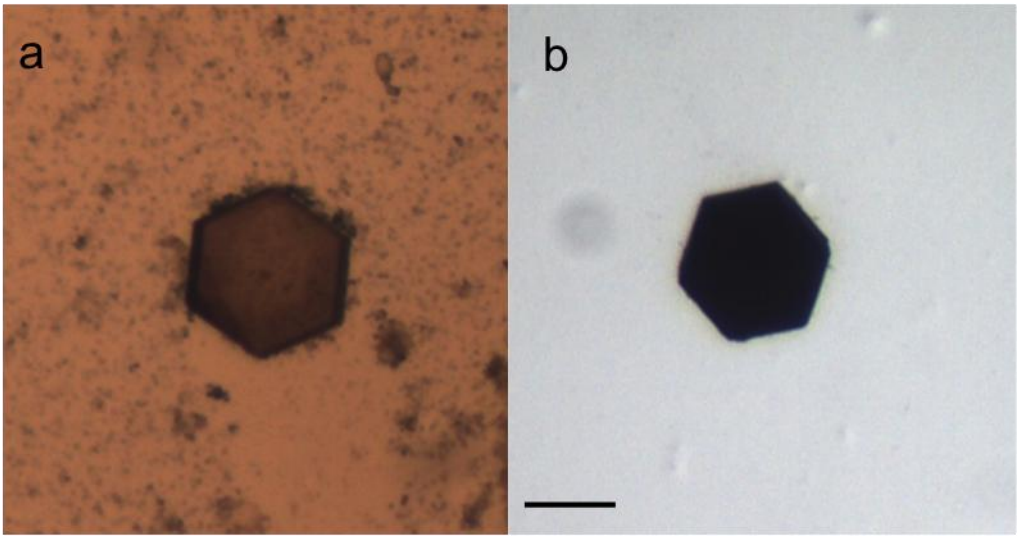

Figure 5.1.11. (a) CJ crystal in a solution containing $Au_{102}(pMBA)_{44}$ (b) The same CJ crystal after adsorption of $HAuCl_4$ and 16 hrs in ascorbic acid. Scale bar is 100 nm.

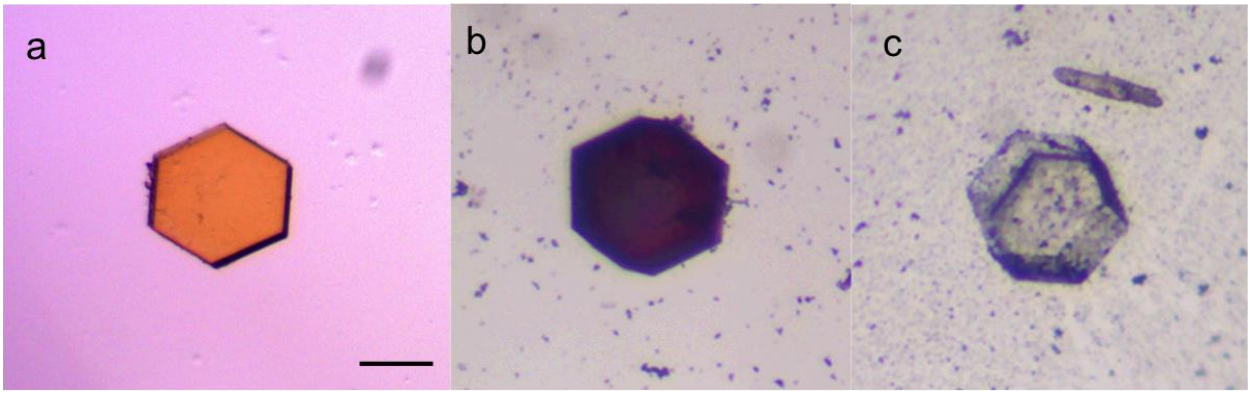

Figure 5.1.12. (a) CJ crystal after 3 days in 1 mg/mL 5nm AuNP. (b) The crystal from (a) after transfer to $HAuCl_4$ then ascorbic acid. (c) A similiarly prepared CJ crystal that was not loaded with 5nm AuNP before transfer to $HAuCl_4$ and ascorbic acid. This crystal shows minimal preferential gold growth within the pores. Scale bar is 100 nm.

We also grew mixed metal nanostructures within the CJ crystal pores by using Au_{25} as a nucleation site for silver growth, using a Silver Enhancer Kit from Sigma Aldrich (Product ID: SE100). Figure 5.1.13 shows the results of one such experiment. Panels a-c show an Au_{25} loaded CJ crystal in the silver growth solution over time, while panels d-f show a similar crystal in the growth solution over time, but without a pre-loaded Au_{25} seed. Over 24 hrs, the seeded crystal undergoes a more significant color change than the unseeded crystal.

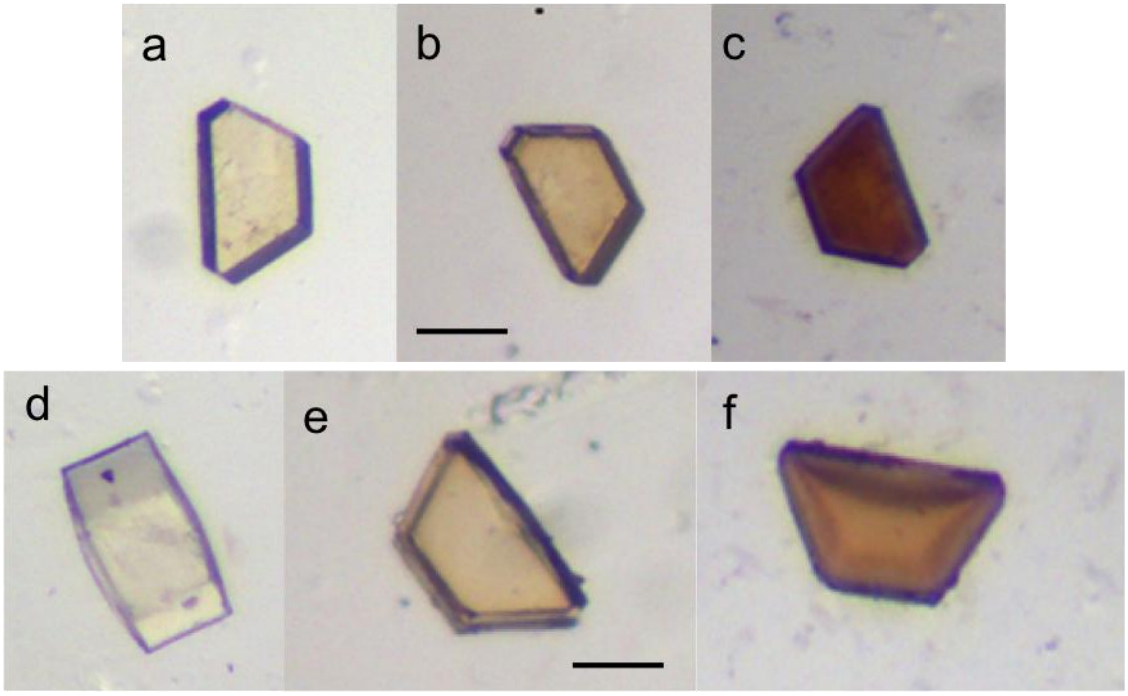

Figure 5.1.13. An Au_{25} loaded (top row) or not (bottom row) CJ crystal in the silver growth solution at t = 0 (a & d), t = 15 min (b & e), and t = 24 hrs (c & f). Scale bars are 100 nm.

Gold growth with surface passivating agents

The following protocol is adapted from[6] and was used to encourage growth only when a nucleation point in the form of $Au_{25}(GSH)_{17}NTA$ is present. In a glass vial under constant stirring, the following solutions were combined: 2 ml of water, 200 µl of 5% (w/v) polyvinylpyrrolidone (PVP), 200 µl of 0.2 M potassium iodide (KI), 200 µl of 0.1 M ascorbic acid, and 30 µl of 0.25 M $HAuCl_4$. The solution should be clear and remain clear for at least 2 hrs.

Separately, a CJ crystal was loaded with 1 mg/mL $Au_{25}(GSH)_{17}NTA$ in phosphate buffered saline (PBS) at pH 7.4 for 30 mins. This "seed" was bound by moving the crystal to a drop of 1 mM $NiSO_4$ for 5

mins and then washing with water for 1 min. This crystal was then placed in a 40 uL drop of the growth solution prepared above. After 10 mins, the crystal was black. This protocol could be repeated on the same crystal every 10 mins to encourage further growth. An empty crystal, one that has not been loaded with gold nanoparticles, remained clear when placed in the growth solution. Figure 5.1.14 shows TEM of the structures resulting after the crystal scaffold was dissolved. The anisotropic shapes (hexagons, prisms, etc.) are representative of the shape that this growth method produces when unconfined, as PVP acts as a crystal-face-blocking ligand.[7] Panel a shows that the heavily grown crystals may not have been completely dissolved by our methods. We visually checked these samples for complete growth through the interior of the crystal by cutting open CJ crystals (Fig. 5.1.15); we saw that the interior of the crystal was filled with gold. We hypothesize that we are synthesizing a substantial amount of gold throughout the crystals with this method, such that there are many interconnects among rods (which we have seen in TEM - Fig. 5.1.10b) that make it difficult to fully dissolve the crystal. We also hypothesize that the larger structures seen in Figure 5.1.14b and Figure 5.1.14c were grown from seeds on the surface of the crystal, and thus were not size restricted by the pores.

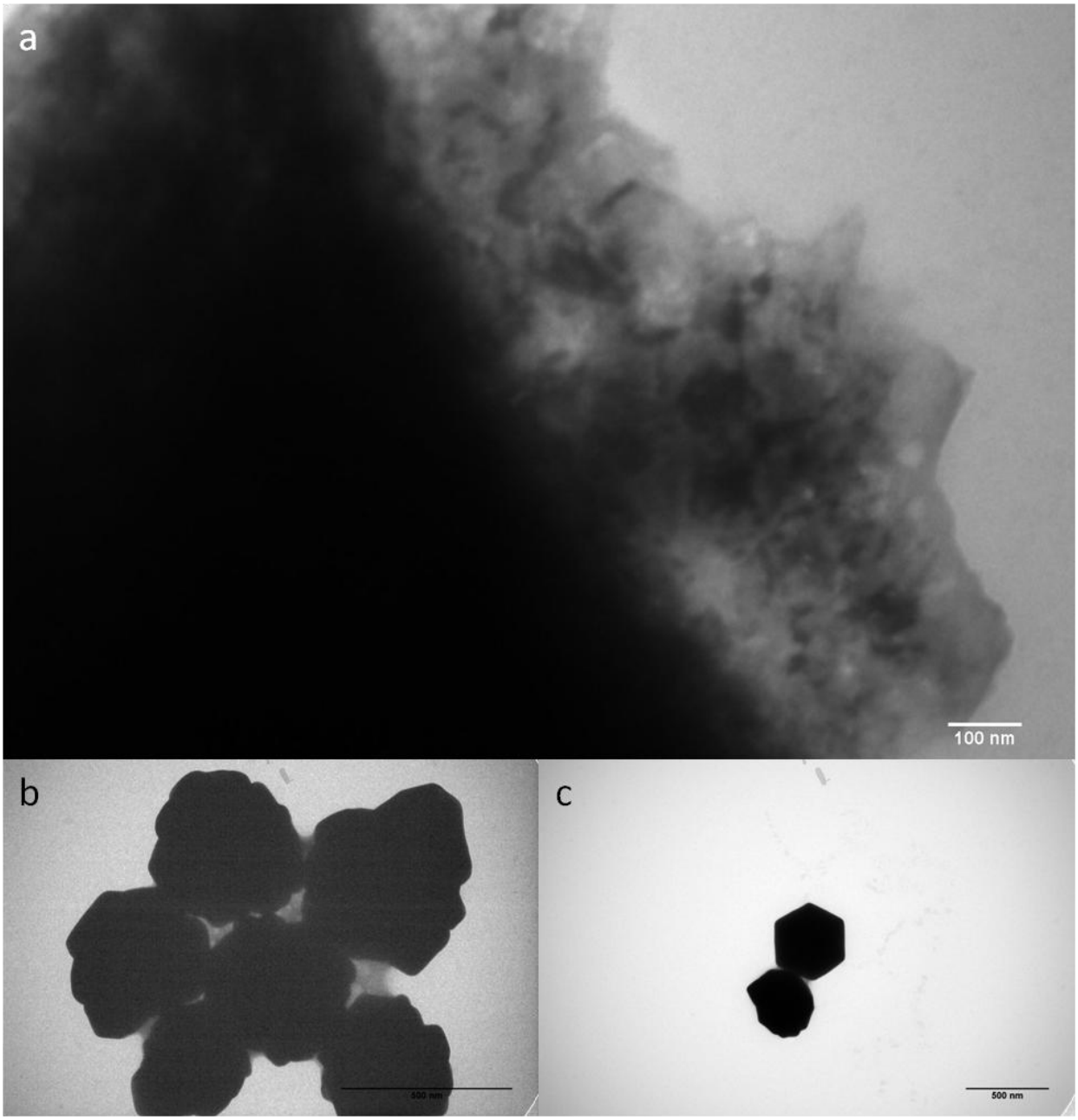

Figure 5.1.14. TEM images of the structures resulting after a crystal is subjected to the above growth protocol and then dissolved. (a) What we believe to be an incompletely dissolved crystal, where the interior gold structures are still connected by partially denatured protein. Scale bar is 300 nm. (b & c) Hexagonal and another amorphous structures. Scale bar is 500 nm.

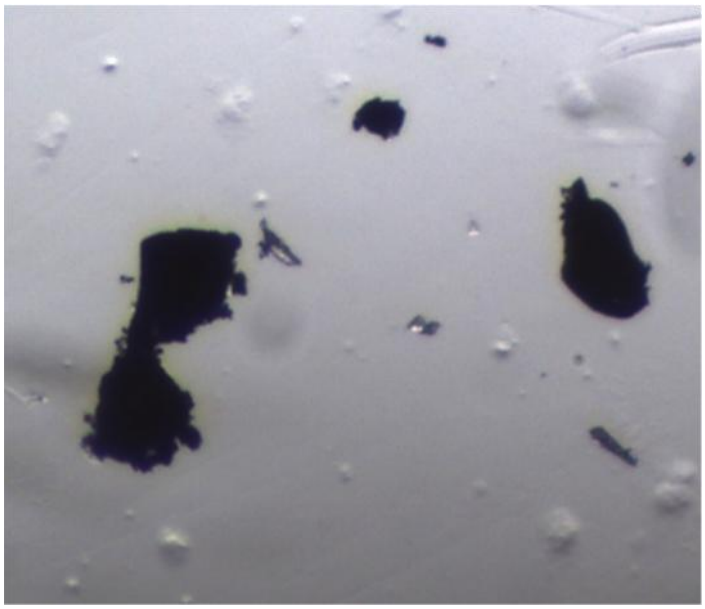

Figure 5.1.15. A crystal grown by the above method and cut into pieces to reveal gold growth throughout the interior.

Gold growth with thiolated precursors

The following protocols were used to encourage stable growth of seeded crystals with minimal self-nucleation due to the decreased reduction potential of sodium aurothiosulfate compared to that of chloroauric acid.

Pre-reduction gold growth: A CJ crystal was loaded with 1 mg/mL $Au_{25}(GSH)_{17}NTA$ in phosphate buffered saline (PBS) at pH 7.4 for 30 mins. The gold seed was then bound using 1 mM $NiSO_4$ for 5 mins, followed by a water wash for 1 min. The crystal was then moved into a drop of 10 mM sodium cyanoborohydride ($NaBH_3CN$) for 30 mins. No change in color or morphology was observed. The liquid was pipetted away and the crystal was washed with water for 1 min. The crystal was then moved to a 1 mM sodium aurothiosulfate (Au(I)) solution and observed for 15 mins. This procedure was repeated for a crystal that was not loaded with 1 mg/mL $Au_{25}(GSH)_{17}NTA$. There was no growth of the seeded crystal and no growth of the unseeded crystal.

Alternately, a CJ crystal loaded with with 1 mg/mL $Au_{25}(GSH)_{17}NTA$ in phosphate buffered saline (PBS) at pH 7.4 for 30 mins while another remained empty. The seeded and unseeded crystals were both bound using 1 mM $NiSO_4$ for 5 mins. Both crystals underwent a water wash for 1 min. Each crystal was placed

into 100 mM sodium borohydride ($NaBH_4$) for 30 mins. Then, the crystals were moved to 1 mM Au(I) and observed for 10 mins. No growth was observed for both the seeded and unseeded crystals.

Post-reduction gold growth: A CJ crystal was loaded with 1 mg/mL $Au_{25}(GSH)_{17}NTA$ in phosphate buffered saline (PBS) at pH 7.4 for 30 mins. A control crystal remained unseeded. Both crystals were moved to 1 mM $NiSO_4$ for 5 mins then placed in a water wash for 1 min. The crystals moved to a 1 mM Au(I) for 1 hour, then moved to the reducing solution of 10 mM $NaBH_4$ and observed for 10 mins.

This protocol was repeated for differing ratios of concentrations of Au(I) to $NaBH_4$. These variations include 10 mM Au(I) to 100 mM $NaBH_4$ and 10 mM Au(I) to 10 mM $NaBH_4$. As expected, the largest amount of growth occurred when there was a 10 mM Au(I) to 100 mM $NaBH_4$ concentration ratio, however there was little separation of growth between the seeded and unseeded crystals. The best separation of growth occurred at 1 mM Au(I) to 10 mM $NaBH_4$ ratio (Fig. 5.1.16) but the seeded growth was not as abundant as that of the higher concentration of Au(I) and $NaBH_4$. In all cases, the seeded crystal turned a dark brown shade and the unseeded crystal ranged from a light to a dark gray color dependent upon solution concentrations. At high concentrations the unseeded crystal had no separation of growth from the seeded crystal. Separation of growth was seen using 1mM Au(I) and 10mM $NaBH_4$ after the samples were left in the growth solution for approximately 2 months. The seeded crystal was completely black, while the unseeded crystal was clear.

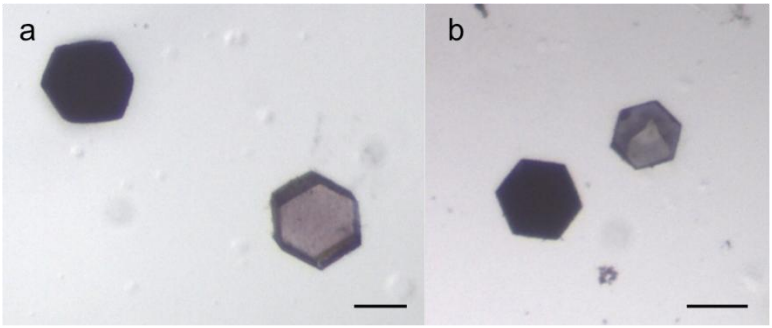

Figure 5.1.16. CJ crystals loaded (black) or not (grey) with Au_{25}, then subjected to gold growth with 1 mM Au(I) followed by 10 mM $NaBH_4$.

We dissolved some of the most successful attempts at seed-mediated Au(I) gold nanorod growth to view by transmission electron microscopy (Fig. 5.1.18). We found that the seeded crystal (panel a)

contained many large particles and other amorphous structures, while the unseeded crystal (panel b) was almost entirely empty.

However, as with most growth methods outlined in this paper, there were inexplicable instances where unseeded crystals (which should not contain defined nucleation points for gold growth) spontaneously grew gold structures as evidenced by their color change. Figure 5.1.17 shows transmission electron microscopy of one such instance, where an unseeded crystal, loaded with 1 mM Au(I) and transferred to 10 mM $NaBH_4$ turned dark in color by eye, and when dissolved showed evidence of some short rods and many particles by TEM. This highlights the precision required to prepare the crystals and solutions so that spontaneous nucleation is minimized.

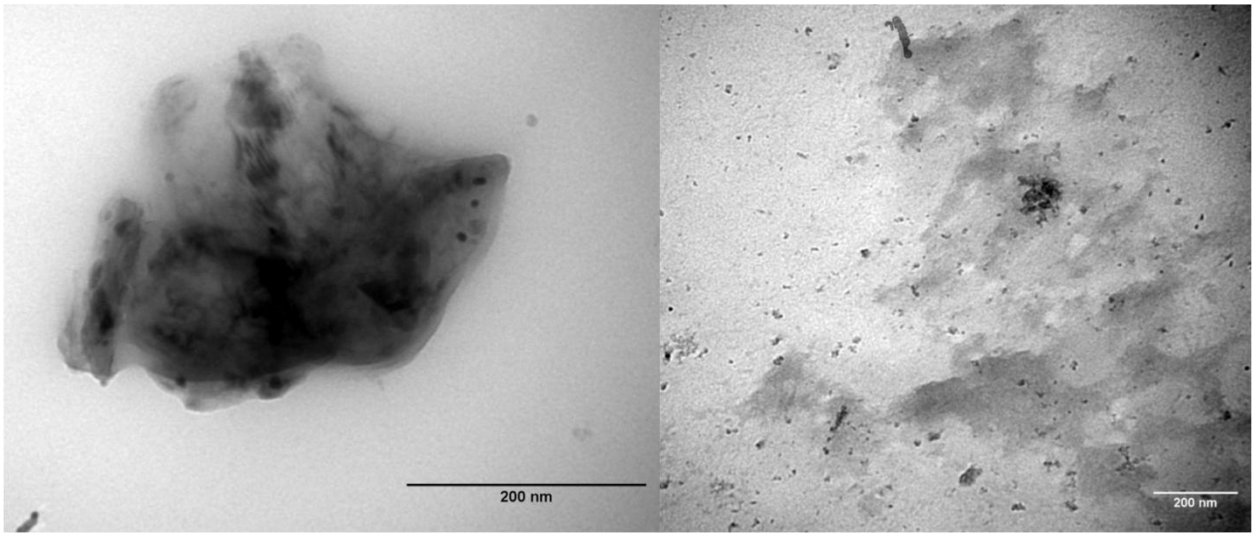

Figure 5.1.17. An unseeded CJ crystal grown in 1 mM Au(I) and 10 mM $NaBH_4$ and dissolved for imaging by TEM. The image on the right shows evidence of gold nanorod formation within the partially dissolved protein matrix, while the image on the left shows some large particles and elliptical structures.

We then attempted to form gold nanorods from Au(I) reduction by increasing the concentrations to 100 mM Au(I) and 100 mM $NaBH_4$. These crystals showed no separation of growth visually, and when dissolved, some rods were evident (Fig. 5.1.19).

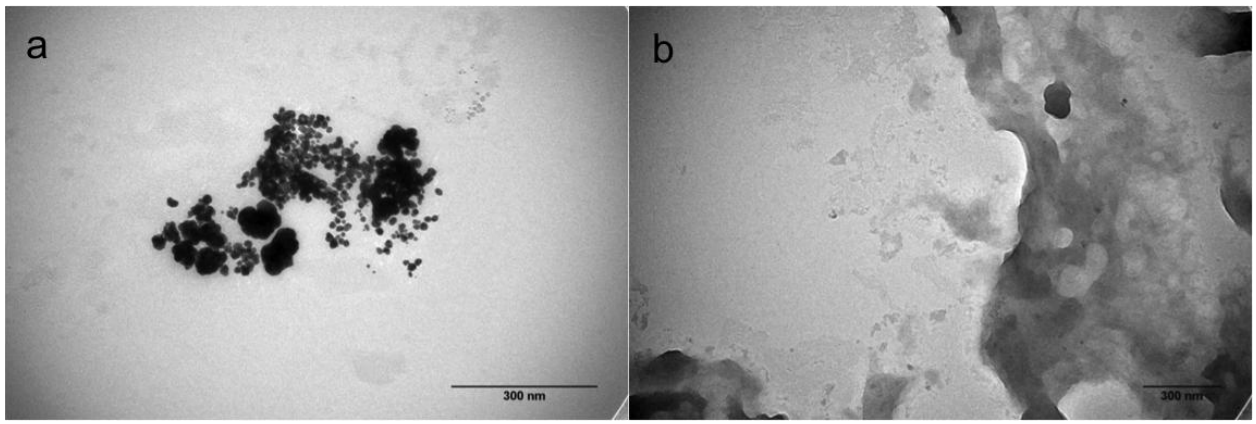

Figure 5.1.18. Transmission electron microscopy crystals from Figure 5.1.16. A CJ crystal that has been loaded with Au_{25} (a), subjected to gold growth by Au(I) and $NaBH_4$, and then dissolved, contains mostly gold particles. A CJ crystal that was unseeded upon gold growth (b) remains devoid of larger gold particles.

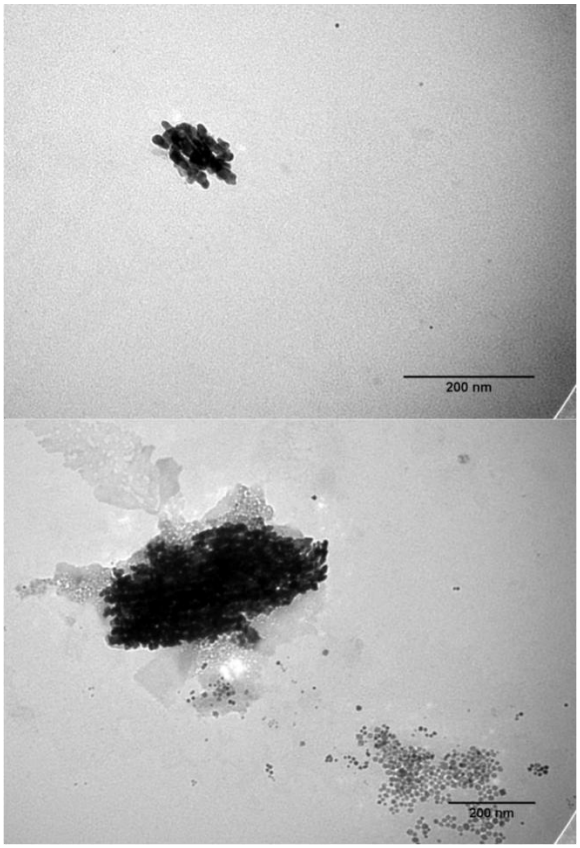

Figure 5.1.19. The short rods and rod bundles that result from gold growth within a seeded CJ crystal placed in 100 mM Au(I) for 1 hr, followed by 100 mM $NaBH_4$ overnight, then dissolved.

Gold growth in 3oc4 crystals

In order to demonstrate the versatility of this method for synthesizing gold nanostructures in arbitrary shapes, we prepared an alterate protein crystal scaffold. The protein crystal (PDB code 3oc4), crystallizes with 9 nm and 5 nm cylindrical axial pores and 5 nm lateral pores (Fig. 5.1.20).

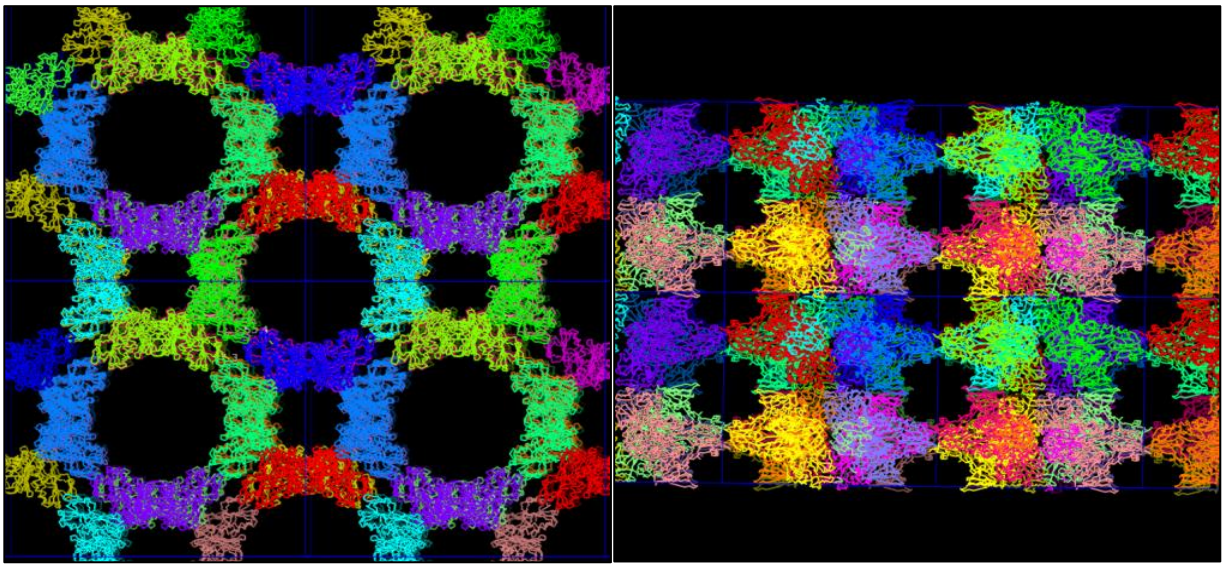

Figure 5.1.20. Molecular Python (Pymol) of the top (left) and side (right) view of a 3oc4 crystal.

We hypothesized that we could grow gold nanorods by the same method within the pores of 3oc4, and when the crystal was dissolved, we would see gold nanostructures that matched the dimensions of the scaffold. Figure 5.1.21 shows the general topology of a 3oc4 crystal, as well as its color after loading 10 mM $HAuCl_4$ for 1 hr (a) and 10 mM ascorbic acid for 1 hr (b). Figures 5.1.22 shows the results of dissolved TEM of these crystals. We can see ~ 5 nm diameter rods embedded within sections of undissolved protein.

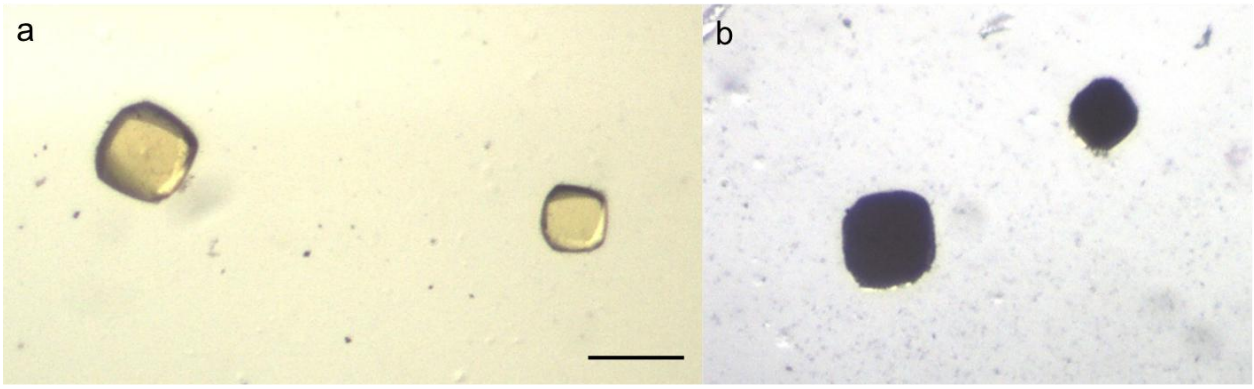

Figure 5.1.21. (a) Crosslinked 3oc4 crystals previously loaded with Au_{25}, now adsorbing 10 mM $HAuCl_4$. (b) The 3oc4 crystals from (a) after 1 hr in 10 mM ascorbic acid. Scale bar is 100 nm.

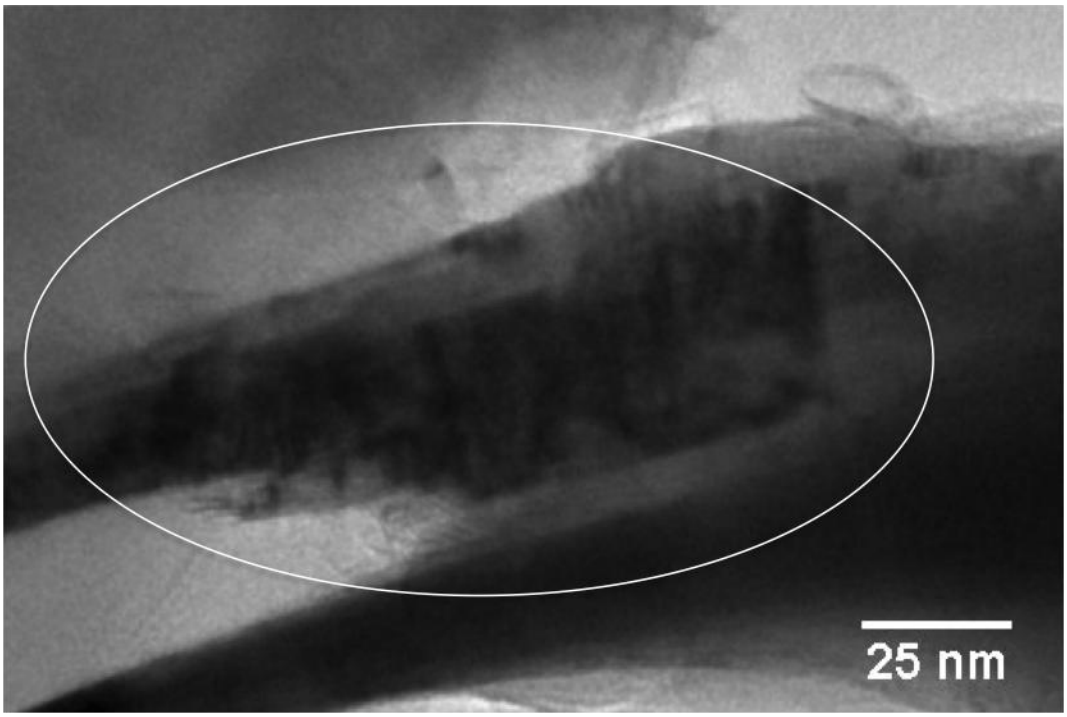

Figure 5.1.22. TEM of rods released from 3oc4 crystals that have been loaded with Au_{25} and soaked in 10 mM $HAuCl_4$ and 10 mM ascorbic acid.

Dissolving crystals for TEM

Protein crystals were dissolved using a variety of methods. Crystals were soaked in approximately 200 uL of 0.5 M NaOH either at room temp, at 35^{o}C, or at 200 rpm and 40^{o}C. For specific experiments detailed below, the dissolving solutions were supplemented with 0.1 M glutathione (GSH) as a capping agent. Dissolving was considered finished when no sign of the crystal was seen under an optical

microscope. This could take anywhere from 4 hrs to 7 days depending on the density of growth within the crystal and the overall size of the crystal.

We often found that using much smaller crystals aided in our ability to quickly dissolve the samples and release the gold nanorods for imaging. Typical CJ protein crystals are between 100 um and up to 1 mm. However by altering the crystal growth conditions, crystals under 1 um in diameter can be grown, whose height is likely limited to 50 nm (Fig. 5.1.23).

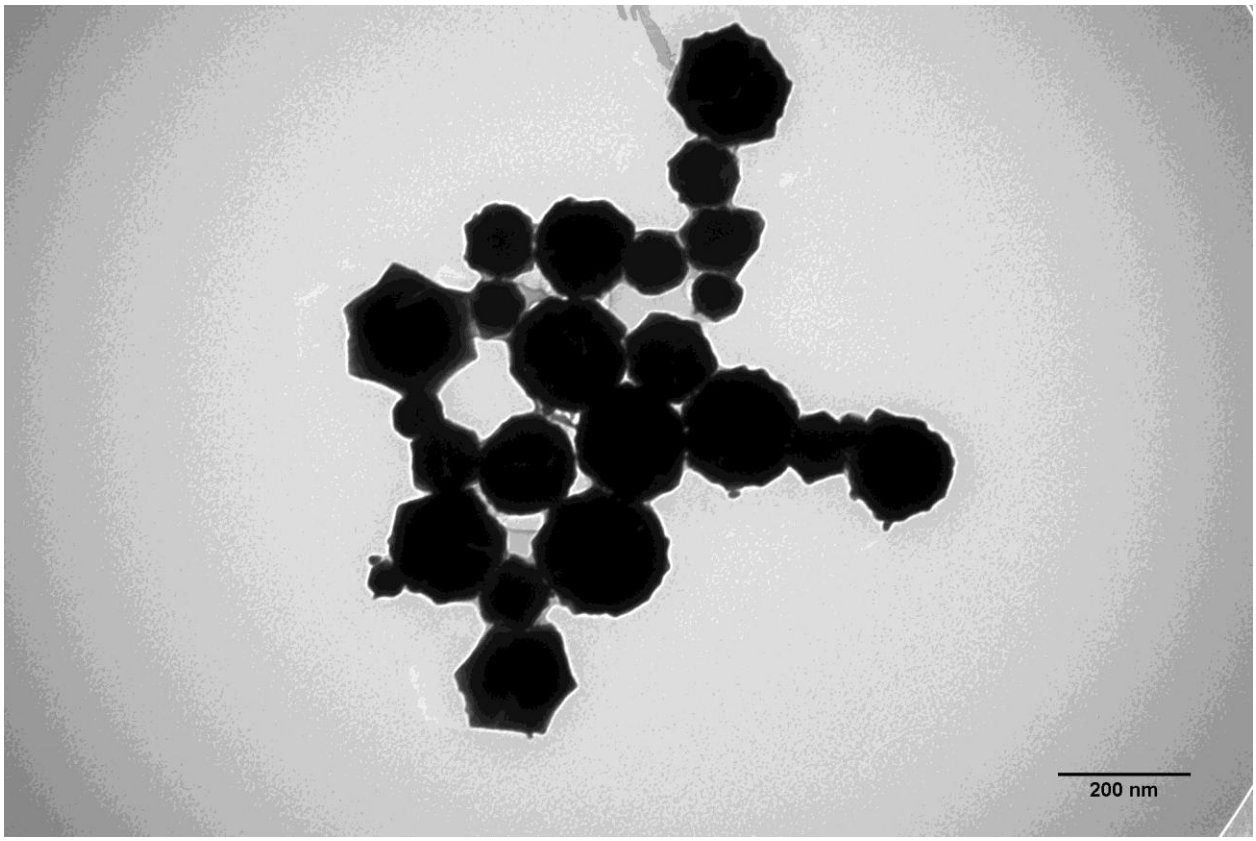

Figure 5.1.23. Transmission electron microscopy of several "microcrystals" whose pores are filled with gold nanostructures.

These "microcrystals" are prepared by a batch method. Instead of individually transferring or looping each crystal into a new solution, a 1 mL sample of microcrystals can be moved to each new solution (i.e. crosslinking, quenching, Au_{25} loading, etc.) by centrifugation and supernatant removal. By this method, we were able to synthesize many microcrystals filled with gold in one process. Additionally, these microcrystals dissolve much more quickly than their larger counterparts. Microcrystals were dissolved using a standardized method. 10 uL of microcrystals suspended in H_2O were added to 500 uL of

dissolving solution (0.5 M NaOH, 0.1 M GSH) and put in an oven at 35^{o}C for 4 hours. The products were centrifuged at 14,000 rpm for 30 minutes and the supernatant was discarded. Products were then re-suspended in water.

It became apparent that a universal dissolving protocol was unattainable for larger crystals, and variations in the dissolving method were needed for different samples created. The following section is intended to summarize the dissolving variations and their implications.

Extended dissolving times needed to dissolve heavily grown crystals tend to convert rods to particles and particles to small particles. A pair of +/- Au_{25} crystals grown with 1 mM Au(I) and 10 mM $NaBH_4$ were dissolved at 40^{o}C and 250 rpm in 0.5 M NaOH and 0.1 M GSH. The -Au_{25} sample dissolved within 3 days, while the +Au_{25} sample took 1 month to dissolve. Both crystals appeared to have a similar amount of growth as seen by eye before dissolving, but once plated onto TEM grids, particles and some rods were seen in the unseeded sample (Fig. 5.1.24) and the grid was blank for the +Au_{25} sample. This suggests that extended dissolving periods allow for product etching, and conversion of nanorods to nanoparticles which is supported by previous studies.[8-10] The magnitude of the effect demonstrated here is twofold due to previous observations, which showed a correlation between darker grown crystals, or more heavily grown crystals, and their need for longer dissolving times.

Alterations in the dissolving protocols varied in their affect on observed products. A pair of samples seen in Figure 5.1.24 show the rod clumps observed after one sample was exposed to slightly higher heat and stirring for 24 more hours (b). This example shows that stirring has no noticeable effect on the products obtained, while short increases in dissolving temperature and time have no noticeable affects either.

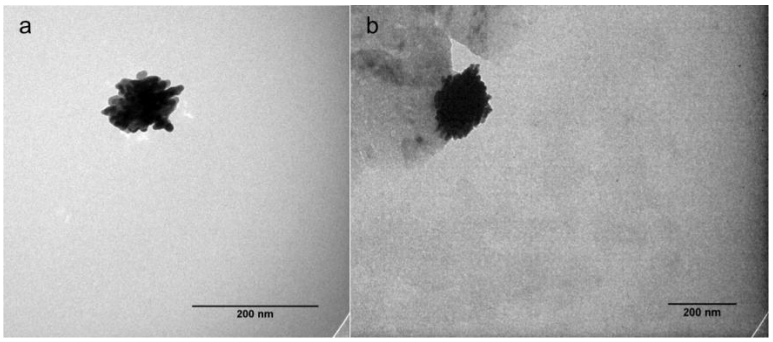

Figure 5.1.24. (a) Nanorod clump derived from a crystal exposed to 0.5 M NaOH at 35^{o}C for 2 days. (b) Nanorod clump derived from a crystal exposed to 0.5 M NaOH at 40^{o}C and 250 rpm for 3 days. Scale bars are 200 nm.

In Figure 5.1.25, we can see that sonication of the dissolved rods using a water bath (3 min) has no noticeable effect on the rods observed. The rods in panel a have an average diameter of 21.4 nm (±3.8, n=630) while the rods in panel b have an average rod width of 22.8 nm (±4.3, n=603).

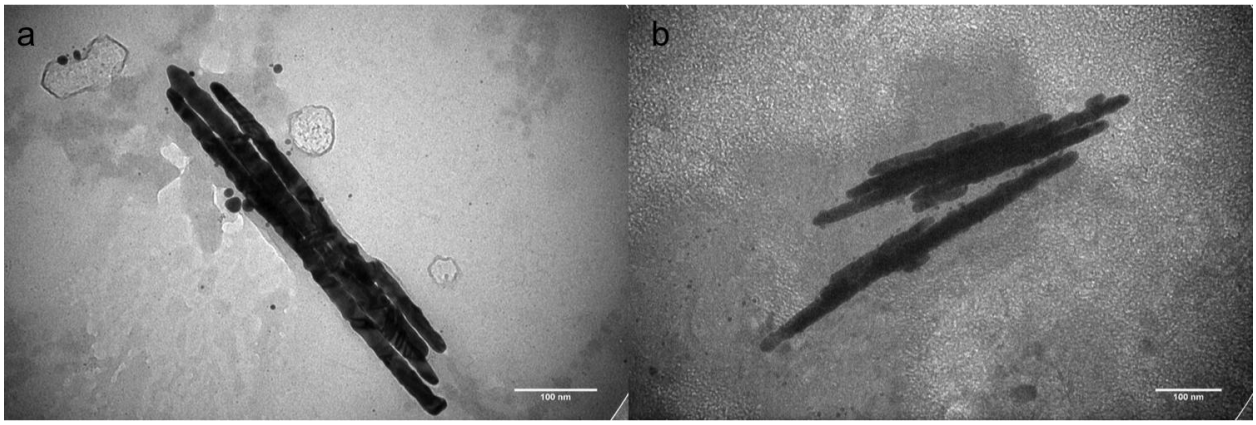

Figure 5.1.25. (a) Gold nanorods after dissolving in NaOH and KCl at pH 13. (b) Gold nanorods after dissolving in the same buffer with the addition of 3 min bath sonication. Scale bars are 100 nm.

The addition of GSH did have an effect on the rods observed, but was based on the amount of growth that occurred in the crystal, which appeared to vary from trial to trial. Figure 5.1.26(a) shows a rod clump resulting from crystals being dissolved at 35^{o}C for 3 days in 0.5 M NaOH. Figure 5.1.26(c) was dissolved under the same parameters with supplementation of 0.1 M GSH. It is clear that GSH helps break rod clumps and exposes portions of the protein crystal that would be difficult to dissolve. It should be noted that exposure to GSH for this length of time results in rod etching, leading to an average diameter of 13.5nm (±2.6, n=185). Glutathione's ability to disrupt rod clumps is oxygen dependent,

which is shown in Figure 5.1.26(d) (dissolved in air free conditions). As shown in Figure 5.1.26(b), we found that by exposure to GSH, we could reduce the effect of etching.

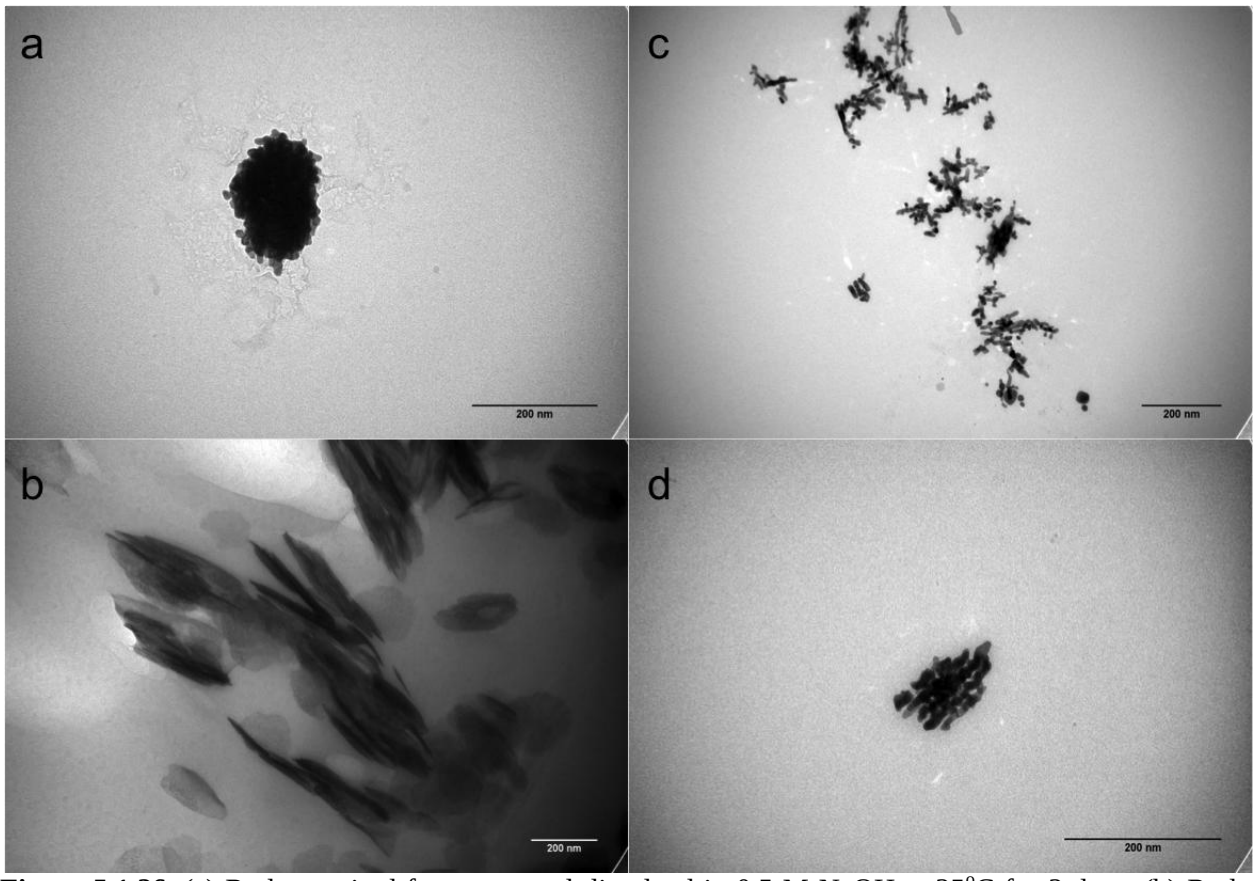

Figure 5.1.26. (a) Rods acquired from a crystal dissolved in 0.5 M NaOH at 35°C for 3 days. (b) Rods acquired from microcrystals dissolve in 0.5 M NaOH and 0.1 M GSH at 35°C for 4 hrs. (c) Rods acquired from a crystal dissolved in 0.5 M NaOH and 0.1 M GSH at 35°C for 3 days. (d) Rods acquired from a crystal dissolved in 0.5 M NaOH and 0.1 M GSH at 35°C for 3 days under Argon. Scale bars are 200 nm.

With all of these variables taken into consideration we were unable to find a reliable universal dissolving method for all samples. Extended exposure to thiols and heat will inevitably etch rods and lead to increased nanoparticle yields, but limited exposure time does not appreciably effect obtained products. It should be noted that the addition of thiols and heat to the original high pH dissolving solution were only used for heavily grown samples that would not dissolve in a reasonable amount of time otherwise.

In addition, we attempted some more creative dissolving methods to help break apart remaining protein structures that often disrupted our imaging ability. We used a solution of cyanogen bromide, which is reported to cleave the protein backbone adjacent to the C-terminus of methionine residues, to attempt to

fully dissolve the protein crystal. However, the chemical crosslinks prevented the crystal from losing it's structure (Fig. 5.1.27).

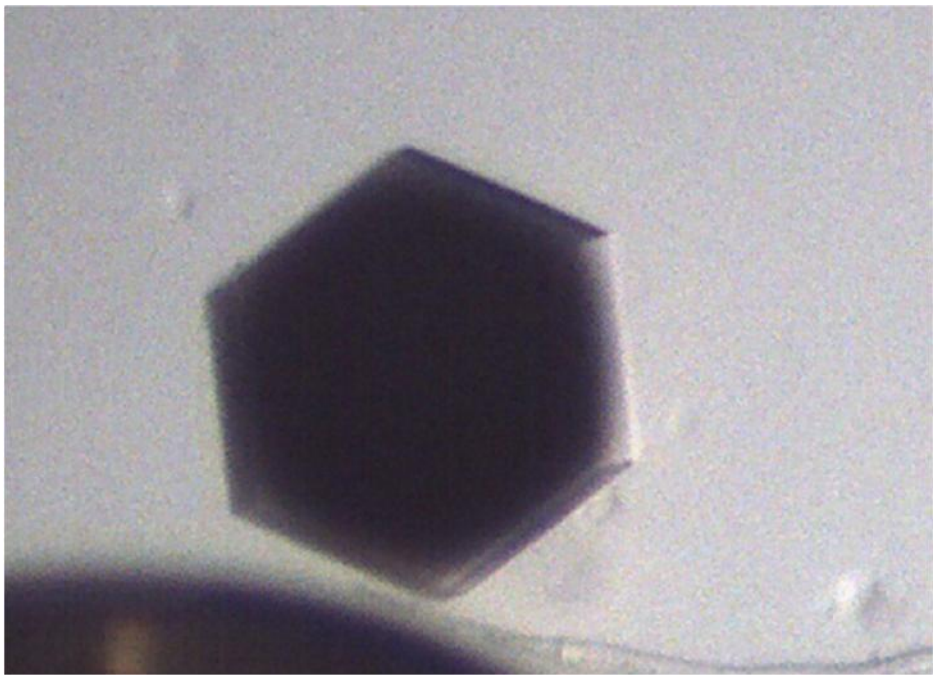

Figure 5.1.27. A gold grown CJ protein crystal in a drop of 0.1 M cyanogen bromide (CNBr). Although CNBr cleaves peptides, the chemical crosslinking by EDC held the protein in place and did not allow for separation of the gold nanostructures. Crystal is approximately 400 nm across.

We used a combination of 4.2 M guanidine hydrochloride (GdnHCl) and 15% hydroxylamine to denature the protein and cleave ester bonds in EDC crosslinks, respectively. This was successful, but we found that hydroxylamine was significantly etching rods and making it difficult to interpret our products on TEM (Fig. 5.1.28).

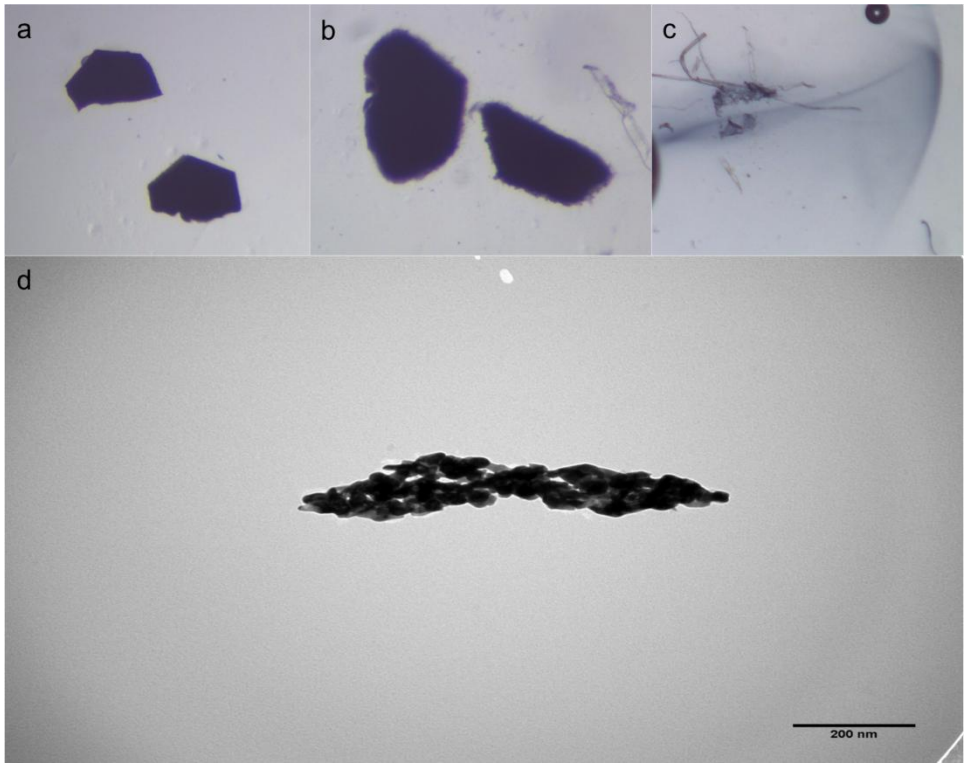

Figure 5.1.28. A gold grown CJ protein crystal in a 10 uL drop of 4.2 M GdnHCl and 15% hydroxylamine at (a) t = 0, (b) t = 4 hrs, and (c) t = 16 hrs. By 16 hrs, the crystal has dissolved and gold nanostructures remain visible in the drop of liquid. (d) TEM images of the gold structures resulting from the above sample. Although this solution completely dissolved the protein crystal, it also appeared to etch the gold products. Some hint of rods remain, but are difficult to interpret. Original crystals (a) were approximately 200 um in size, and expanded to ~300 um in GdnHCl (b). Scale bar for (d) is 200 nm.

Electron microscopy

To obtain TEM images of released gold nanorods, solutions of the grown and dissolved protein crystals were spun at 14,000 rpm for 30 minutes and the supernatant was decanted. The remaining solution (approximately 10 uL) was used to suspend the rods and 4uL of this solution was mounted onto 200 mesh Cu grids with a 50 nm carbon coating (Ted Pella Inc.). TEM images were taken on a JEOL-1400 Transmission Electron Microscope at an accelerating voltage of 100 kV. A tilt series from $\pm 60^{o}$ was collected on a rod bundle in 0.5^{o} increments suing the JEOL-1400 TEM mentioned above. IMOD was used to generate a 3D reconstruction from the acquired tilt series.

For high resolution TEM/STEM (scanning transmission electron microscopy), gold nanorods were mounted as explained above, and images were taken on a JEOL JEM2100F Transmission Electron

Microscope at 200 kV. STEM images were collected using a Gatan 806 HAADF detector and Nano Beam Diffraction was used to collect electron diffraction of rods in 10 nm increments (Fig. 5.1.29).

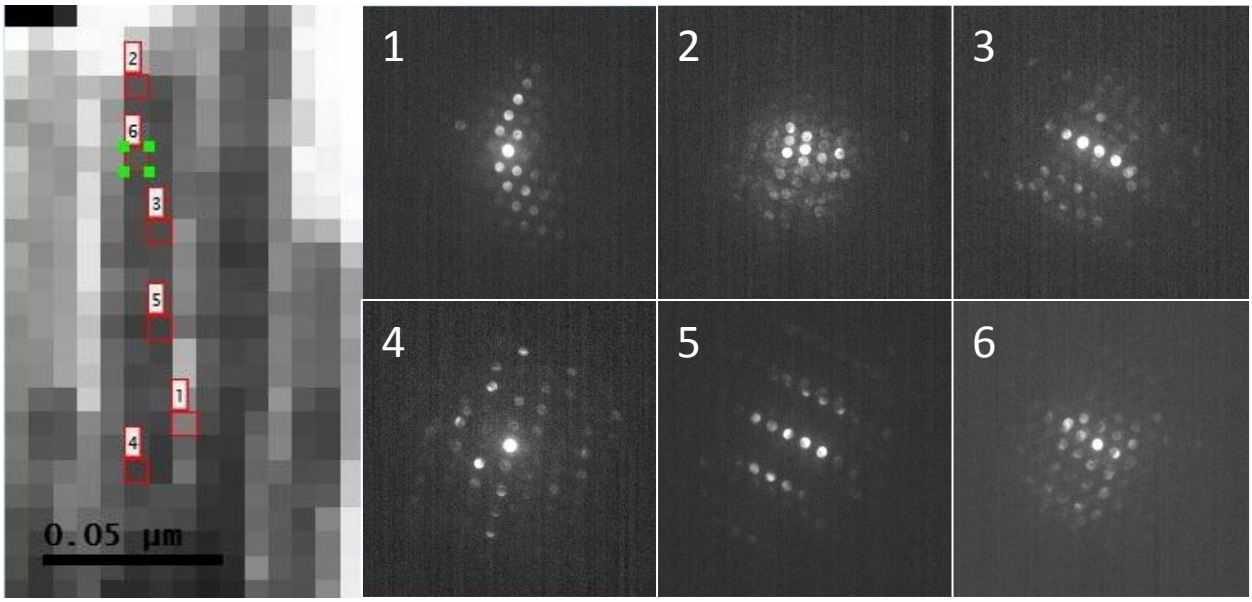

Figure 5.1.29. Left Panel: Electron diffraction heat map taken every 10 nm on a gold rod bundle with 6 highlighted segments. Right Panels (1-6): Electron diffraction patterns corresponding to the highlight regions in the left panel.

In-situ imaging of gold rods grown within crystal pores

We used a variety of methods to attempt to view the gold nanostructures within intact crystal pores. Our first attempts involved ultramicrotomy of resin embedded crystal samples for observation by transmission electron microscopy (TEM). Gold grown crystals were embedded following previously published methods.[11] Briefly, a hard grade Epon resin mixture containing 50% resin monomer, 35% nadic methyl anhydride, and 15% dodecenyl succinic anhydride was lowly introduced to the crystal solution, beginning with 5% resin mixture in acetone (v/v). Over three days this was increased to 100% with shaking. Accelerator (dimethylaminemethyl phenol) was added to the resin at the 100% step. The resin mixture, with crystal embedded, was cured over two days at 60^{o}C. The samples were cut to ~ 90 nm thick on a Riechert Ultracut E using a glass or diamond knife and imaged by TEM as described above.

It was apparent when cutting the thin sections that the difference in mechanical properties between the gold and the protein/resin was causing the sample to warp or shear when cutting, a common problem when imaging composite materials. When these samples were viewed under TEM, we saw

evidence of sheering and buckling (an example can be seen in Figure 5.1.30). Physical deformation of this kind would easily destroy any crystallographic periodicity before imaging could occur.

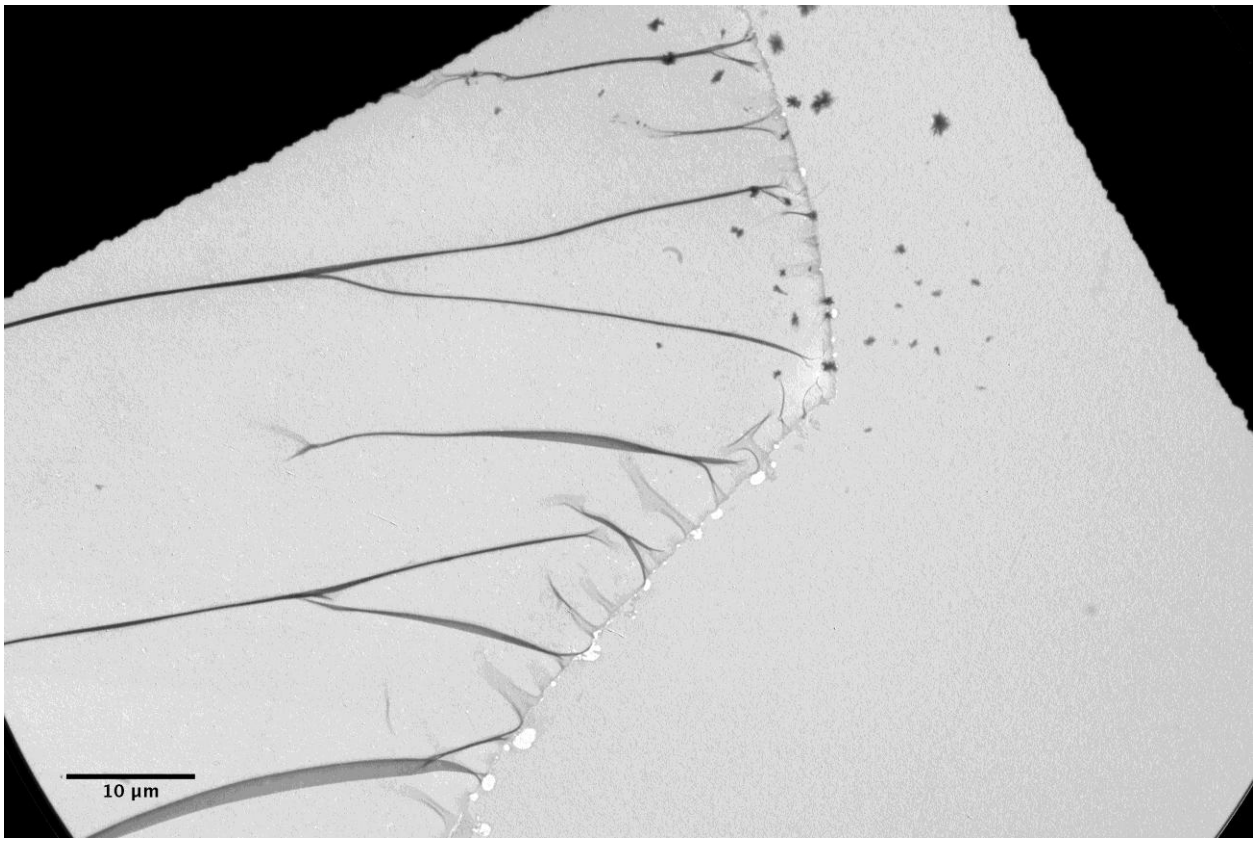

Figure 5.1.30: Thin section of resin embedded crystal shows shearing and buckling under TEM.

Next, we attempted scanning electron microscopy (SEM) on gold grown crystals that were cut into pieces to expose the interior of the crystal. Figure S31 shows that while cutting/smashing the crystals clearly caused damage to the protein, the bright spots of high electron density suggest the presence of gold structures throughout the crystal.

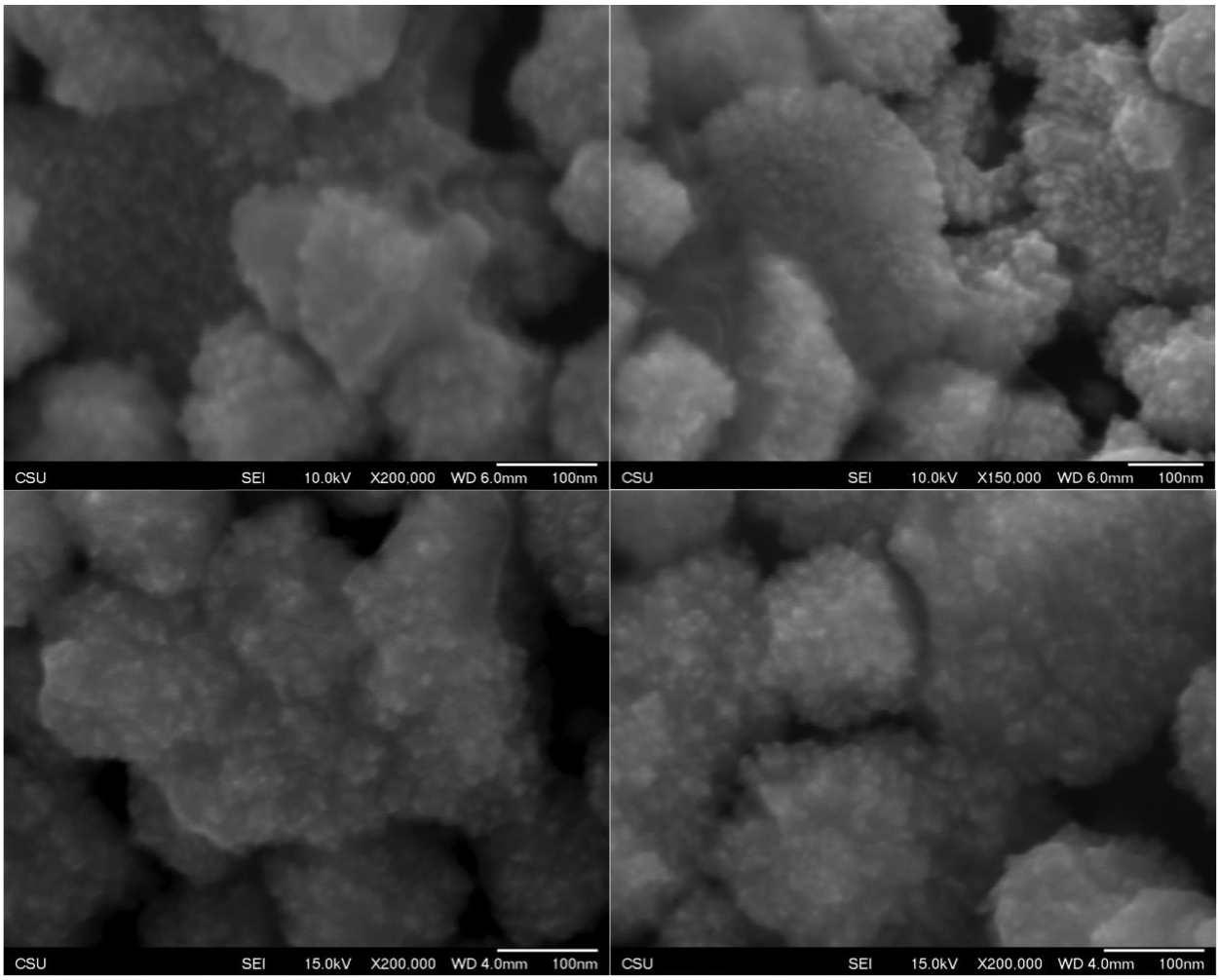

Figure 5.1.31. Scanning electron microscopy of gold grown CJ crystals cut into pieces to expose the interior of the crystal.

Given the possibility for distortion during cutting, we next fractured grown crystals under liquid N_2 to help preserve their structure. Specifically, liquid N_2 was poured into a well containing gold grown crystals. A frozen crystal manipulation tool was used to crush the crystal sample. The frozen pieces were then transferred to a TEM grid. Figure 5.1.32 shows the results of this imaging method. Panel a suggests the presence of a ~20 nm electron dense rod that is half exposed and half crystal embedded after the shattering procedure. Panel b again suggests the presence of ~20 nm electron dense rods still completely embedded in the crystal after shattering. Panel c shows evidence for potential axial pore growth with parallel ~4 nm rods embedded within the crystal. Panel d shows a zoomed in view of the thin rods from panel c.

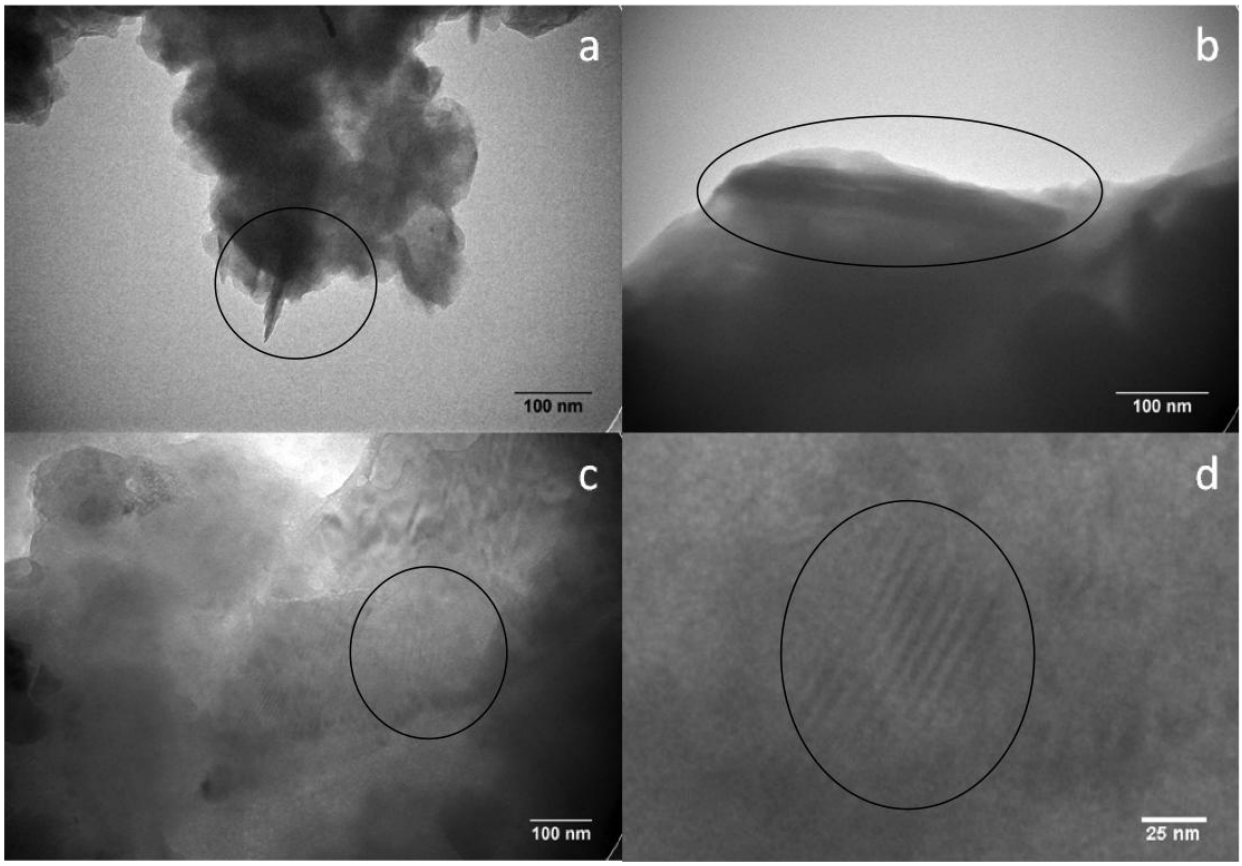

Figure 5.1.32. TEM images of gold grown CJ protein crystals frozen under liquid N_2 and shattered to reveal the interior of the crystals. (a) Gold nanorod, partially crystal embedded and partially exposed. (b) Two nanorods trapped within the crystal. (c) Evidence for axial pore growth within the crystal. (d) Zoomed in section of the approximately 4 nm rods embedded in the crystal from image C. Scale bar is 20 nm.

Additionally we attempted to confirm the presence of gold through energy-dispersive X-ray spectroscopy (EDS) of thick sections of grown crystals. We again resin embedded gold grown CJ crystals (by the same method described for ultramicrotoming), but instead used a glass knife to cut thick sections (2-3 um) of the sample. These were placed on a grid for SEM/EDS imaging. By EDS, we were able to detect significant presence of gold within the interior of the crystal. However, the crystal and resin surrounding the embedded sample was very beam sensitive and prevented viewing and focusing on the sample for extended periods of time due to beam damage.

Because we are able to grow microcrystals that are less than 1 um in diameter and theoretically less than 200 nm in thickness, we attempted to visualize intact, gold grown crystals by TEM (see Fig. 5.1.23 above). Unfortunately at room temperature the samples were too sensitive for the amount of beam power

that would be required to image at the needed resolution. Additionally, we believe that the distance between axial pores in the CJ crystal (<3 nm) approaches the resolution limit to detect separation between gold rods in adjacent pores.

Elemental analysis

The elemental analysis samples consisted of three replicates, each containing three crystals loaded with gold nanoparticles and dissolved in 2 mL of aqua regia. Volumes were calculated by measuring the surface areas and heights of the crystals using a calibrated optical microscope. Samples were prepared by loading crosslinked CJ crystals with $Au_{25}(GSH)_{17}NTA$ overnight, binding the seed with Ni(II), moving the crystal to a drop of 10 mM $HAuCl_4$ for 1 hr, and lastly reducing the gold in a drop of 10 mM ascorbic acid until black. Elemental Analysis was performed at Midwest Laboratories, Inc. Further information regarding *in crystallo* gold loading concentrations and theoretical gold packing calculations can be found here.[1]

Rod diameter and length analysis

After TEM image acquisition, rod widths and lengths were analyzed using ImageJ software. Rod lengths varied significantly between 10 and 900 nm. A histogram of occurrences for a total of 453 measured rods is shown below in Figure 5.1.33.

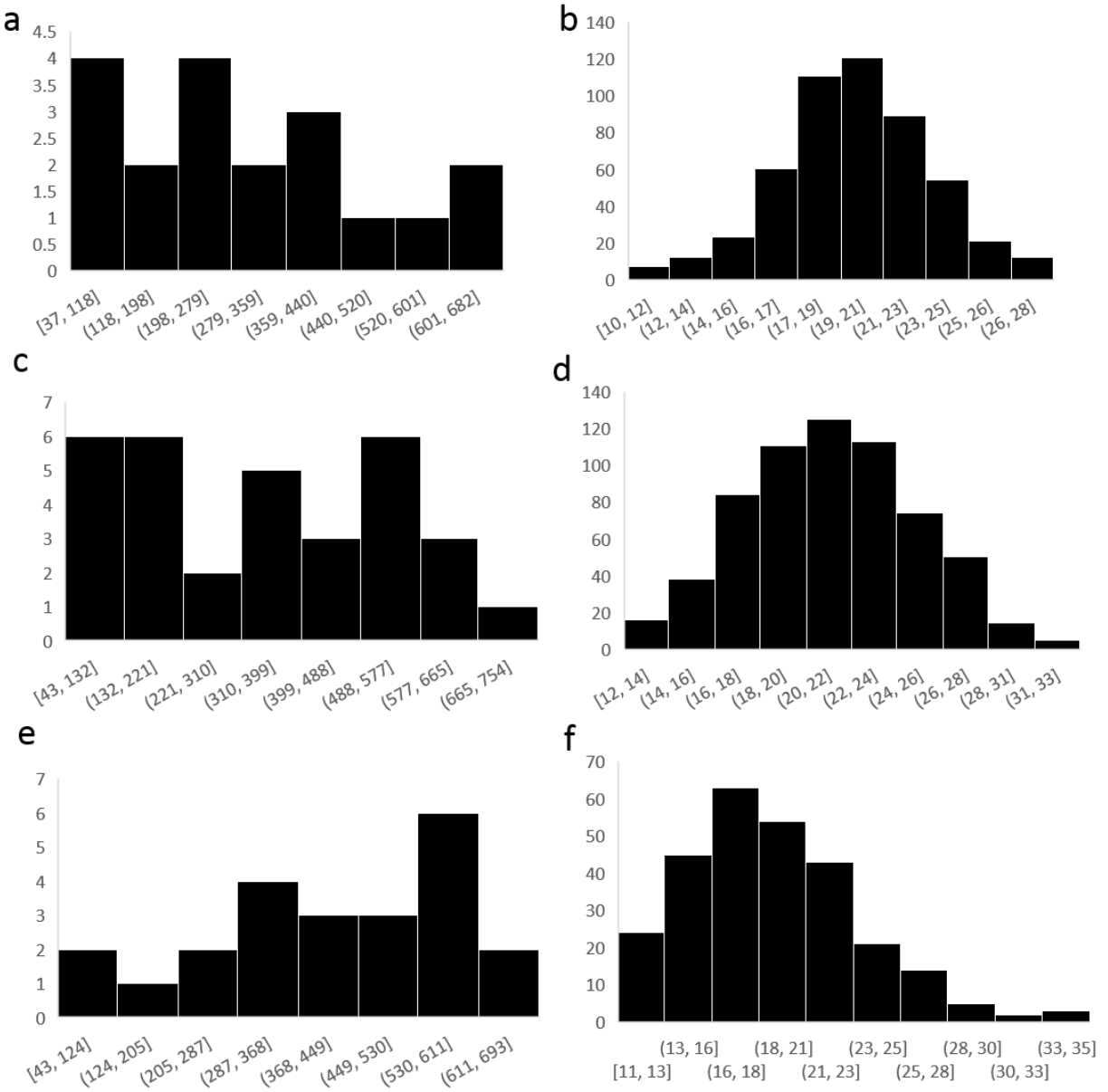

Figure 5.1.33. Histogram of frequencies of occurrence of rod length and width (a) unseeded length (b) Unseeded width (c) Seeded length (d) Seeded width (e) Seeded and sonicated products length and (f) width.

Due to the variation in rod width within a single rod, multiple measurements were made per rod. CJ crystal axial pores are ~13.1 nm in diameter, but the average rod width over all growth methods and dissolving protocols was 20.2 nm with a standard deviation of 4.7 nm.

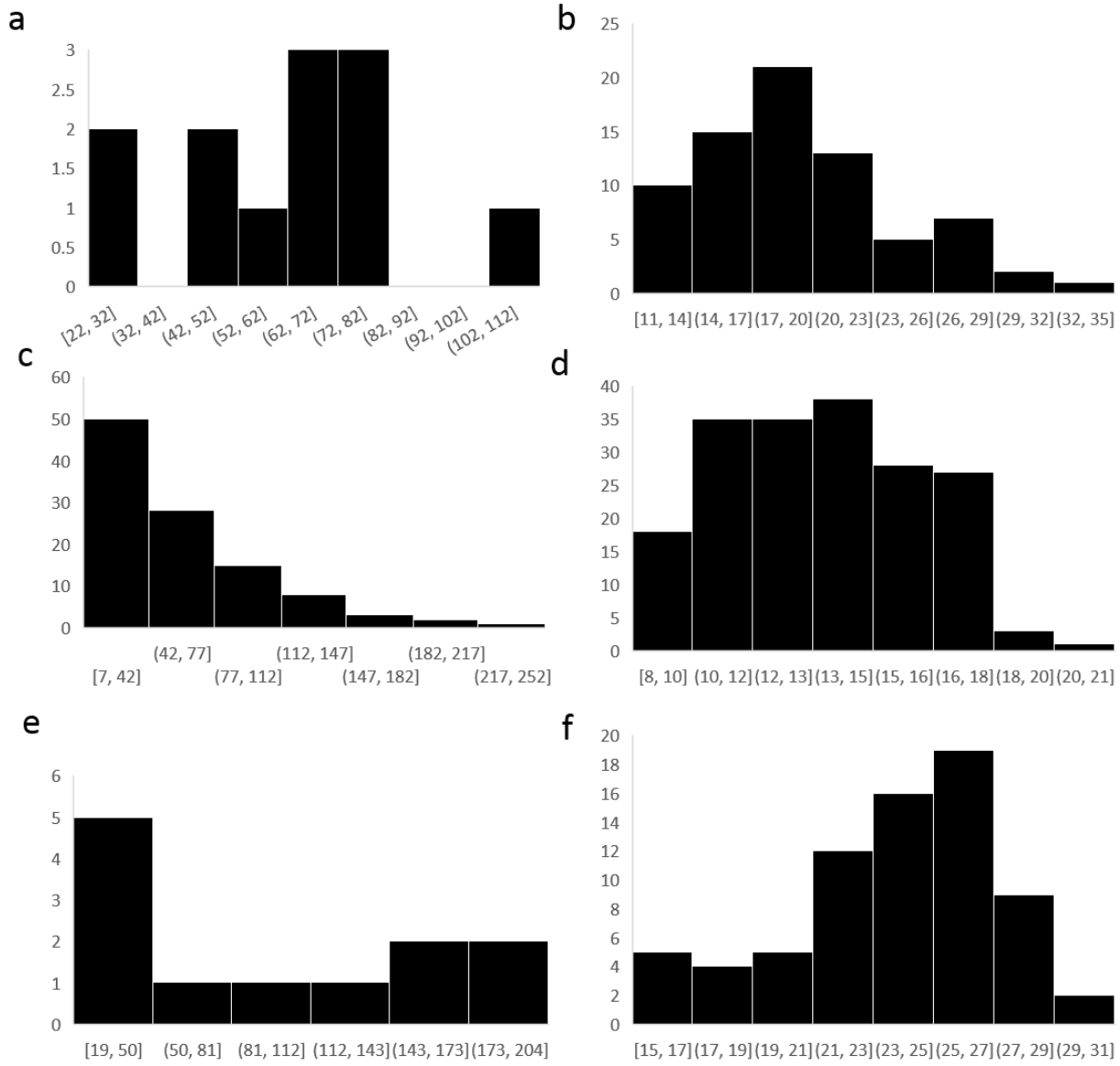

Figure 5.1.34. Histogram of frequencies of occurrence of rod widths and lengths from (a & b) GdnHCl and HA and heat (c & d) GSH and heat and (e & f) 6x growth cycles. A total of 2496 measurements were taken over 452 rods and four different crystal dissolving conditions.

For multiple samples, we measured crystal surface areas before and after gold growth and observed a crystal swelling of approximately 20% (Fig. 5.1.35).

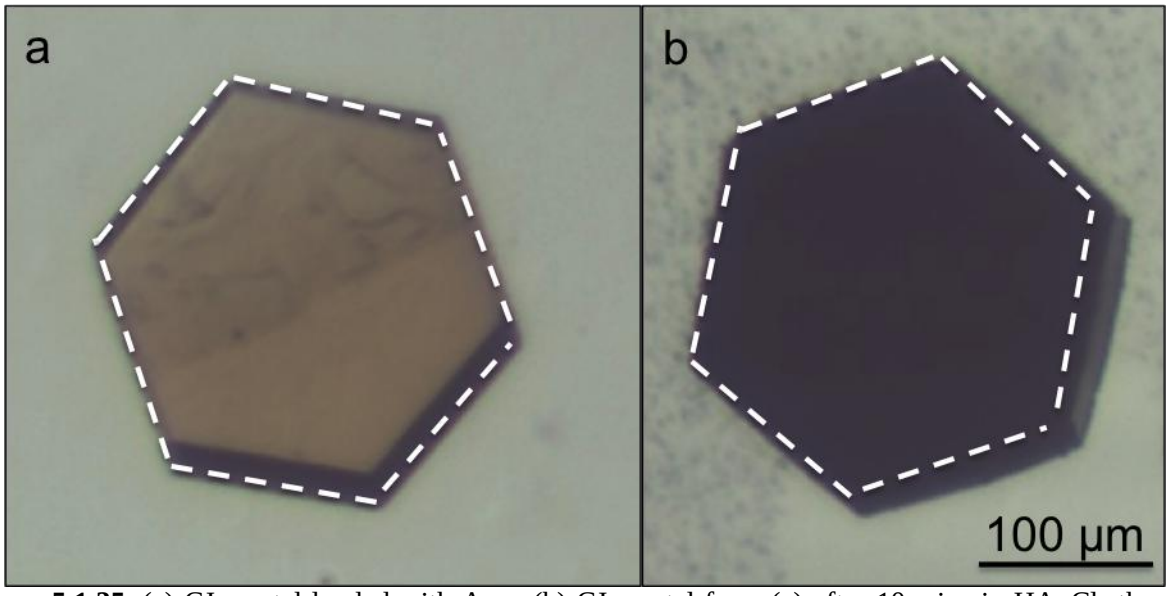

Figure 5.1.35. (a) CJ crystal loaded with Au_{25}. (b) CJ crystal from (a) after 10 mins in $HAuCl_4$ then 10 mM ascorbic acid at t = 1 hr. The white dotted line roughly indicates the original outer area of the crystal.

The calculations shown in the diagram below help explain how this phenomenon of pore and crystal swelling may take place. Before gold growth (top left) the 13 nm diameter pore is within a translated unit cells of 18 nm side length. The total area is 281 nm^2, with the pore consisting of 133 nm^2 and the protein approximately 148 nm^2. With the new pore diameter of 20 nm, equal to that of the gold rods grown within, and assuming retention of the same unit cell angles, the new minimum total unit cell area is 462 nm^2 and the new protein area remains the same at 148 nm^2. In fact, a 20 nm diameter circle is the largest circle that can be contained within a parallelogram whose non-circle area (grey areas in diagrams below) are limited to 148 nm^2. In other words, 20 nm is as large in diameter as the gold nanorods can become without breaking or expanding the unit cell in some way. For example (bottom right), a gold nanorod of hypothetical 21 nm diameter would require a total protein (grey) area of 158 nm^2 to be fully contained, which is larger than the protein area available per unit cell of the CJ crystal. Without significant denaturation, the overall volume of the protein within the crystal should not change. We hypothesize here that the force of the fast and significant gold growth was able to move the protein 'out of the way' up until the point of actually breaking peptide bonds, denaturing the protein, or severing crosslinks between monomers. Looking more closely, the growth of the gold nanorods expands one corner of the unit cell (length a) by 1 nm while contracting the adjacent corner (length b) by 1 nm. The

corners of these diagrams correspond to a tetramer (interface of four CJ monomers) within the crystal, which is also the location of some of the most flexible loops and helices in the crystal structure, most likely allowing for more than enough room to make these changes in area.

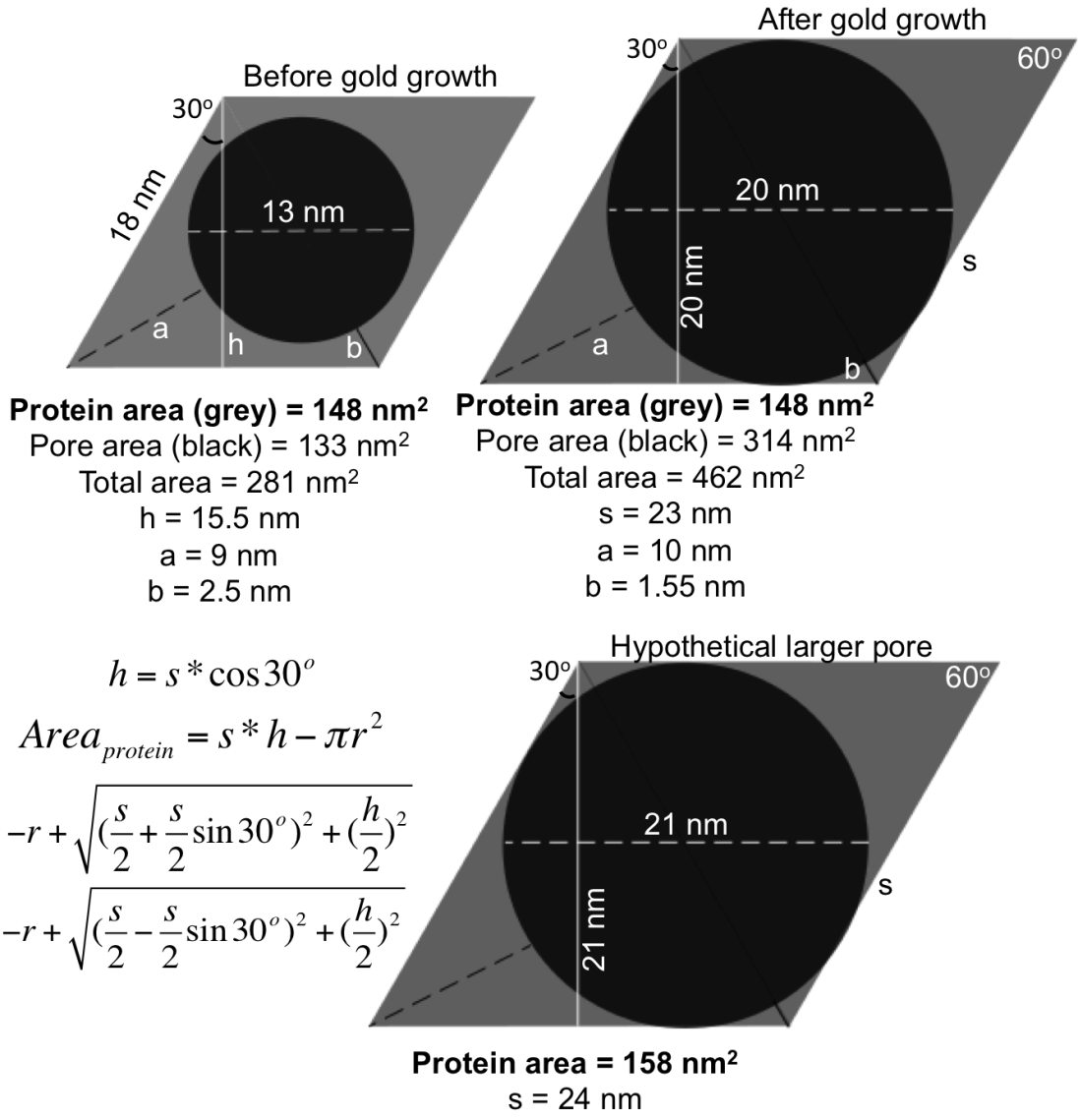

Figure 5.1.36. Area calculations due to pore swelling after gold nanorod growth.

To further explore how the gold growth can distort the protein crystal pores, we used 1% gluteraldehyde as an alternate crosslinker to EDC. Gluteraldehyde is a more aggressive crosslinker that is capable of polymerizing and forming covalent linkages between more sites, and we hypothesized that rods grown within the pores of gluteraldehyde-crosslinked CJ crystals might have smaller diameters than

those grown in EDC crosslinked crystals. Most rods were superimposed on others within bundles, so only a few individual rods were able to be accurately measured. The average width of rods growth in this type of crosslinked crystal were 15.2 nm with a standard deviation of 1.7 nm (n=19) (Fig. 5.1.37). These results may suggest that rods grown in more rigid crystals will have an overall smaller width due less crystal expansion.

Figure 5.1.37. Gold nanorods resulting from a gluteraldehyde-crosslinked CJ crystal grown with 10 mM $HAuCl_4$ and 10 mM ascorbic acid and dissolved for TEM.

Pore space visualization[12]

To visualize the major solvent channels in CJ crystals we started with the recent CJ structure (pdb code: 5W17) with improved resolution (2.58Å).

We then used the map_channels_v0.5 software (CITATION BELOW) to generate a "cast" of the solvent channels ("./map_channels 5w17.pdb –cm"). The resulting pdb file consisted of a field of dummy atoms on a hexagonal grid with an automatically selected grid spacing of 2.24 Å. We pruned this cast by

excluding all grid points that were less than 4 Å from a protein atom. Within PyMOL we then used the supercell.py utility (contributed to the PyMOL wiki by Thomas Holder) to generate a 2 x 2 x 3 collection of unit cells. To observe the fine structure in the minor solvent channels most clearly, we excluded the top 40% of the uppermost unit cells. We then completed the visualization for Figure 1b in chapter 2 in PyMOL using a smooth Gaussian surface representation (gaussian_resolution = 7) for the solvent channels (b=50, q=1, 3 Å grid, 6 Å buffer, 0.1 isosurface level).

PyMOL commands for gaussian surface representation:

set surface_quality, 1

alter all, b=50

alter all, q=1

set gaussian_resolution, 7

map_new mapB, gaussian, 3, all, 6

isosurface surfB, mapB, 0.1

5.2 Chapter 3 Supporting Information

Cell Lysate Preparation

P. moraviensis Stanleyae cells were grown for 24 h at 30 °C in 2,800-mL Fernbach flasks containing 1 L of LB-Miller medium supplemented with 10 mM Na_2SeO_3. Cells were harvested via centrifugation at 10,000 x g for 20 minutes and the pellet resuspended in 15 ml of ice-cold 25 mM Tris and 192 mM glycine buffer (pH 8.3) supplemented with 1 mM 4-(2-aminoethyl) benzenesulfonyl fluoride hydrochloride (AEBSF) and 0.02% 3-[(3-cholamidopropyl) dimethylammonio]-1-propanesulfonate hydrate (CHAPS). Then, cells were treated with 0.2 mg mL-1 lysozyme (Sigma-Aldrich, St. Louis) for 20 min in a 100 rpm shaking incubator at 30°C. Following lysozyme treatment, the cells were homogenized

via a French pressure cell operated at 120 MPa. The procedure was repeated twice and this final homogenate was spun at 22,500 x g for 60 min at 4°C to remove unbroken cells and cell debris. These procedures were modified from Hunter.[13]

SEM

P. moraviensis Stanleyae cells were grown for 24 h at 30 °C in a 125 mL Erlenmeyer flask containing 50 mL LB medium (Teknova) supplemented with 10 mM $HNaSeO_3$ (Alfa Aesar, 98+%). Cells were harvested via centrifugation at 4,000 rpm (3,220 rcf) for 20 minutes at 4 °C. Cells were then washed in 20 mM Tris (pH 7.4) (Fisher) three times followed by resuspension in 1 mL of fixing fixative solution (2% glutaraldehyde (25%, Sigma-Aldrich) and 2.5% formaldehyde); the fixing solution was allowed to react for 6 h at 4 °C. Post-fixation, the fixing solution was removed by centrifugation and the pellet was washed five times in 20 mM Tris (pH 7.4). The cells were then resuspended in 1 mL 20 mM Tris (pH 7.4). Aliquots (2 μL) were mounted on 400 mesh Cu grids with a 50 nm C coating. Dry-mounted cells on TEM grids were loaded onto a STEM holder. STEM images were taken on a JEOL JSM-6500-F Scanning Electron Microscope at an accelerating voltage of 30 kV.

EDS

EDS was performed on *P. moreviensis* Stanleyae cells in the SEM as described above. EDS was collected on a Noran System 7 X-ray Microanalysis detector with a time interval of 1 s.

Dry-mount cellular TEM

P. moraviensis Stanleyae cells were grown for 24 h at 30 °C in a 125 mL Erlenmeyer flask containing 50 mL LB medium (Teknova) supplemented with 10 mM $HNaSeO_3$ (Alfa Aesar, 98+%). Cells were harvested via centrifugation at 4,000 rpm (3,220 rcf) for 20 minutes at 4 °C. Cells were then washed in 20 mM Tris (pH 7.4) (Fisher) three times followed by resuspension in 1 mL of fixing fixative solution (2% glutaraldehyde (25%, Sigma-Aldrich) and 2.5% formaldehyde); the fixing solution was allowed to react for 6 h at 4 °C. Post-fixation, the fixing solution was removed by centrifugation and the pellet was washed five times in 20 mM Tris (pH 7.4). The cells were then resuspended in 1 mL 20 mM Tris (pH

7.4). Aliquots (2 μL) were mounted on 400 mesh Cu grids with a 50 nm C coating. TEM images were taken on a JEOL JEM-1400 Transmission Electron Microscope at an accelerating voltage of 100 kV.

3D EM

Cells Harvested at 6, 6, 12 hours post selenium inoculation

A single colony was picked from an LB agar plate of P. moraviensis Stanleyae and placed into 3 ml of LB culture media and incubated aerated at 160 RPM, overnight at 28 ^{o}C. The cells were harvested and rinsed 2 times with sterile phosphate-buffered saline (PBS) and then resuspended into 200 mL of fresh LB media. Half of the flasks were given a 10 mM final concentration of $HNaSeO_3$, the other half an equivalent amount of media as control. The cultures were shaken at 160 RPM at 28 ^{o}C and samples were collected 6, 9, and 12 hours post Se inoculation. They were high pressure frozen using a Wohlwend Compact 02 (Technotrade) high pressure freezer into aluminum planchettes. Samples were freeze-substituted in 0.2% osmium tetroxide, 0.1% uranyl acetate, and 5% water in acetone using the fast-freeze substitution method[15] over 3 hours. Samples were rinsed in acetone and embedded in epon (EMS) over several days. 200 nm sections were cut using a Ultracut UCT (Leica) microtome with a diamond knife (Diatome) and placed on formvar-coated copper slot grids. Sections were post-stained with 2% aqueous uranyl acetate and lead citrate. 15 nm gold fiducials were added.

Dual-axis tilt-series were acquired using SerialEM[16] on a Tecnai TF20 (FEI) transmission electron microscope from +/-60, 1 degree intervals on an Ultrascan digital camera (Gatan) at a pixel size of 0.91 nm. Tomograms were reconstructed using IMOD.[17] A total of 23 tomograms were collected which are detailed below.

+6 hours control: 3 TS

+6 hours Se: 3 TS

+9 hours control: 3 TS

+9 hours Se: 3 TS

+12 hours control: 3 TS

+12 hours Se: 3 TS

36 hours control, dried: 1 TS

36 hours Se, dried: 1 TS

36 hours Se, resin: 1 TS

Cell Harvested at 36 Hours Post Se Inoculation

Cells were grown as previously described in the dry-mount cellular TEM methods. Differences in the procedure were that the cells were grown for 36 hours and the media was changed every 12 hours. Media was exchanged by centrifuging cells at 4,000 rpm at 4 °C for five minutes. The supernatant was poured out and new LB was added and the cells were then resuspended and allowed to continue growing. Cells were fixed at 36 hours as described in the dry-mount cellular TEM methods. Chemically fixed cells were rinsed 2 times in dH20 and then went through a graduated dehydration series into 100% acetone. They were infiltrated with epon (EMS) over several days. 300 nm sections were cut using an Ultracut UCT (Leica) microtome with a diamond knife (Diatome) and placed on formvar-coated copper slot grids. Samples did not undergo post-stain. 10 nm fiducials were added. Single-axis tilt-series were acquired using SerialEM[4] on a Tecnai TF30 (FEI) transmission electron microscope from +/-60, 1 degree intervals on an Ultrascan digital camera (Gatan) at a pixel size of 1.02 nm. Tomograms were reconstructed and modeled using IMOD.[17]

Segmentation

Reconstructions were sectioned using IMOD.[17] The outer cell walls were segmented every 5 tomographic slices on the XY plane. An isosurface was generated and the threshold lowered to determine a cutoff value for imodauto to differentiate cellular background from SeNP. Imodauto was set at a threshold of 1 (out of 255), which generated a model with both the gold fiducials and the SeNPs. The models were merged and the outline of the cell was meshed to generate the image.

Native Polyacrylamide Gels

Native polyacrylamide gels were used to check for selenite reduction capabilities utilizing the procedure described by Hunter.[18] Briefly, cell lysate was purified via HIC column then separated on a 8% non-denaturing polyacrylamide electrophoresis gel (Invitrogen, Carlsbad, CA) using a Novex® Tris-Glycine Native Running Buffer (Invitrogen). Following electrophoresis, gels were placed into zip-lock bags filled with Ar and assayed for selenite reduction capability. Assay was performed by incubation of the gel in a solution of 50 mM HEPES (pH 7.5), 200 mM Na_2SeO_3 and 1mM NADPH. Bands that turned red were excised for further study.

Protein MS/MS

SDS-PAGE and In-Gel Trypsin Digestion for LC-MS/MS

Bands of interest were excised from the gel and processed for in-gel trypsin digestion and LCMS/MS as previously described.[19] Briefly, the gel pieces were washed with 200 μL of LC-MS Grade Water (Optima LC-MS, Fisher Scientific) for 30s and destained with 2 x 200 μL of 50% Acetonitrile (ACN; Optima LC-MS Grade)/50 mM ammonium bicarbonate at 60 ^{o}C, with intermittent mixing. The pieces were dehydrated with 100% ACN and dried via vacuum centrifugation in a SpeedVac for 5 min. Proteins were reduced and alkylated, in-gel with 25 mM DTT in 50 mM ammonium bicarbonate (60°C for 20 min) and 55 mM IAA in 50 mM ammonium bicarbonate at room temperature in the dark for 20 min. Gel pieces were then washed with Optima water and dried. The dried gel pieces were rehydrated in 20 μL 12 ng/μL MS-grade Trypsin (ThermoPierce, San Jose, CA) /0.01% ProteaseMAX surfactant/50 mM ammonium bicarbonate mixture for 10 min at room temperature, overlaid with 30 μL 0.01% ProteaseMAX surfactant/50 mM ammonium bicarbonate and incubated at 50 °C for 1 h. Extracted peptides were transferred and the digestion halted by addition of 10% trifluoro-acetic acid to a final concentration of 0.5%. Peptide extracts were dehydrated and stored at −20 °C prior to analysis by LC-MS/MS.

Peptides were purified and concentrated using an on-line enrichment column (Thermo Scientific 5 mm, 100 mm ID x 2 cm C18 column). Subsequent chromatographic separation was performed on a

reverse phase nanospray column (Thermo Scientific EASYnano-LC, 3 mm, 75 mm ID x 100 mm C18 column) using a 30 minute linear gradient from 10%-30% buffer B (100% ACN, 0.1% formic acid) at a flow rate of 400 nanoliters/min. Peptides were eluted directly into the mass spectrometer (Thermo Scientific Orbitrap Velos). The instrument was operated in Orbitrap-LTQ mode where precursor measurements were acquired in the Orbitrap (60,000 resolution) and MS/MS spectra (top 20) were acquired in the LTQ ion trap with a normalized collision energy of 35kV. Mass spectra were collected over a m/z range of 400-2000 Da using a dynamic exclusion limit of 2 MS/MS spectra of a given peptide mass for 30 s (exclusion duration of 90 s). Compound lists of the resulting spectra were generated using Xcalibur 2.2 software (Thermo Scientific) with a S/N threshold of 1.5 and 1 scan/group.

GHSR TEM

Glutathione reductase Se nanoparticles were made by mixing 25 μL(66 μg) of glutathione reductase (from S. cerevisiae) with 500 μL 100 mM selenite ($HNaSeO_3$), 100 μL 10mM NADPH and 275 μL 10x PBS (pH 7.4). The solution was allowed to mix for an hour, at which point the solution turned red. The samples were centrifuged and the pellet washed with 1x PBS (pH 7.4). Particles were then mounted onto 400 mesh Cu grids with a 50 nm C coating (Electron Microscopy Sciences). TEM images were taken on a JEOL JEM-1400 Transmission Electron Microscope at an accelerating voltage of 100 kV.

SeO_3/TeO_3 Assays

Samples (1 ml) were made using a constant NADPH concentration (0.36 mM) in PBS. Varying selenite/tellurite concentrations were used (1 mM to 1 M). All blanks contained the same content as the reactions except NADPH. 5 μL (13 μg) of glutathione reductase was added to the reaction and A340 measurements were obtained every 2 seconds for the first 10 minutes, every 10 seconds for the next 20 minutes, followed by every minute for the next 30 minutes. The decrease in absorbance at 340 nm was used to analyze the initial reaction rate.

Protein Concentration Assay

Four 315 uL samples were created in 1x PBS, 10mM selenite, and equal amounts of Baker's yeast glutathione reductase from Sigma Aldrich. The samples had varying NADPH concentrations from 0 to 6mM and were allowed to react for approximately 20 hours. Once the reaction was completed the samples were centrifuged at 14000 rpm for 30 minutes to remove any synthesized nanoparticles. The supernatants were collected and a Bradford assay was performed in triplicate on the four samples in a 1:9 ratio of sample to reagent. The nanoparticle pellets were then washed with water two times to remove any free protein, followed by redispersion of the pellets in .005% SDS. These samples were then run through the assay in the same ratio also in triplicate. Two standard curves were made, one using GSHR in 1x PBS and one using GSHR in .005% SDS.

SDS Gel Assay

Seven 315 uL samples were created in 1x PBS, six in 4mM NADPH and a control with no NADPH. The six samples contained a range of selenite from 0 to 10mM while the control contained no selenite. An equal amount of Baker's yeast glutathione reductase from Sigma Aldrich was added to each sample and allowed to react for approximately 20 hours. The samples were spun down at 14000 rpm for 30 minutes to remove any synthesized nanoparticles. Following this, a 4-15% SDS gel from Bio-rad was set up with each well containing 25 uL of a solution made from 25uL sample in 5 uL of SDS loading dye (Bio-Rad). The gel was run at 110 V for 75 minutes. After staining with Coomassie Brilliant Blue G-250 followed by de-staining, the gel was imaged with a Bio-Rad GelDoc XR. It should also be noted that another set of samples were created which contained 1/3 of the protein as the SDS samples. Three samples were created under the exact same conditions as stated before apart from the difference in added enzyme. The samples consisted of a control of GSHR in 1x PBS, and two samples containing 4mM NADPH. One of the cofactor samples contained no selenite and the other with a final concentration of 10mM. A 6% native gel was casted and six wells were loaded with 25uL of a solution made from 25uL sample and 5 uL SDS loading dye. The first three wells were filled with samples containing the lowered amount of added enzyme, while the last three wells contained samples with the added enzyme mentioned

in the beginning of this section. This gel was run at 110 V for 1 hour and was stained with Coomassie Brilliant Blue G-250 following destaining and imaged with the same Bio-Rad GelDoc XR.

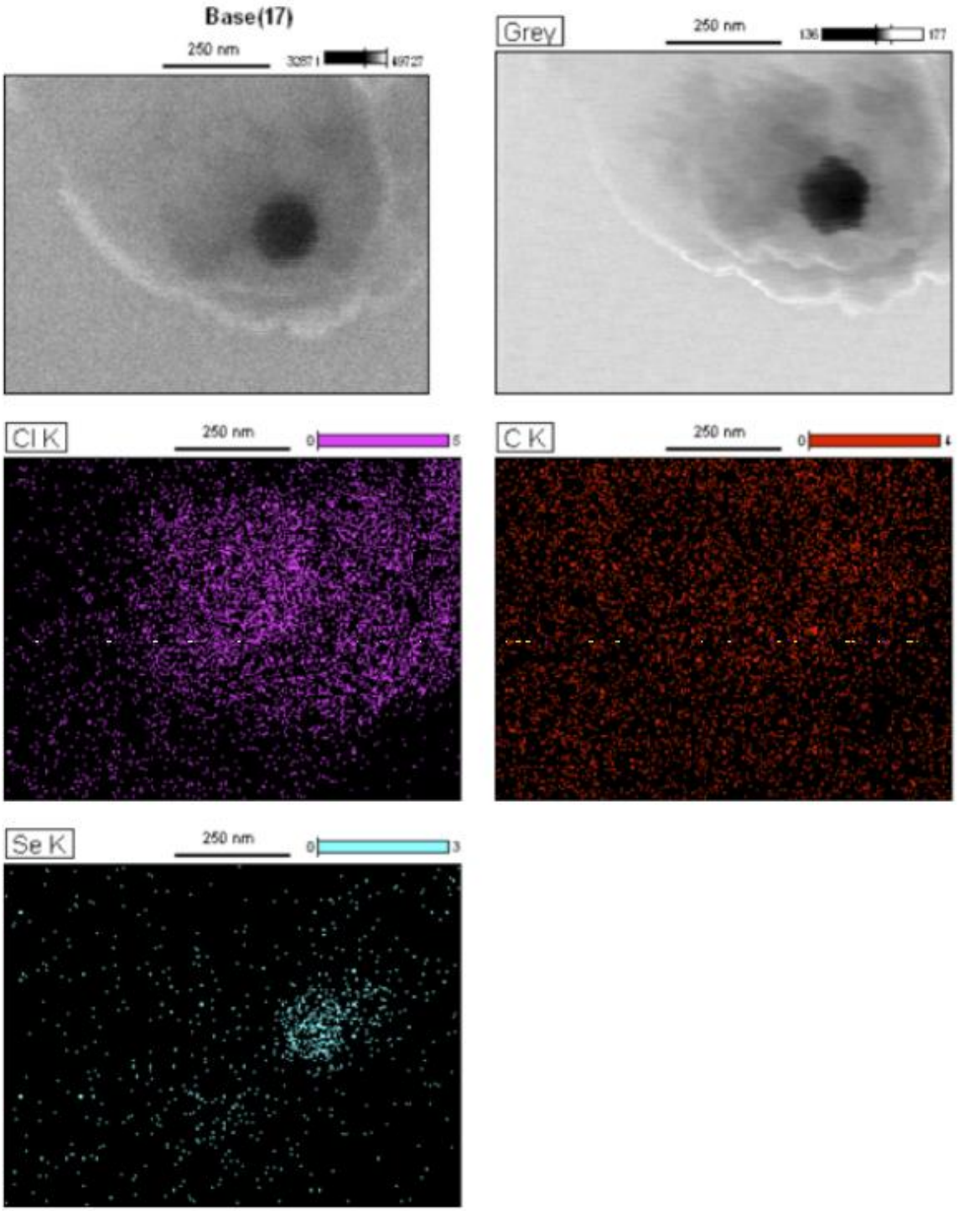

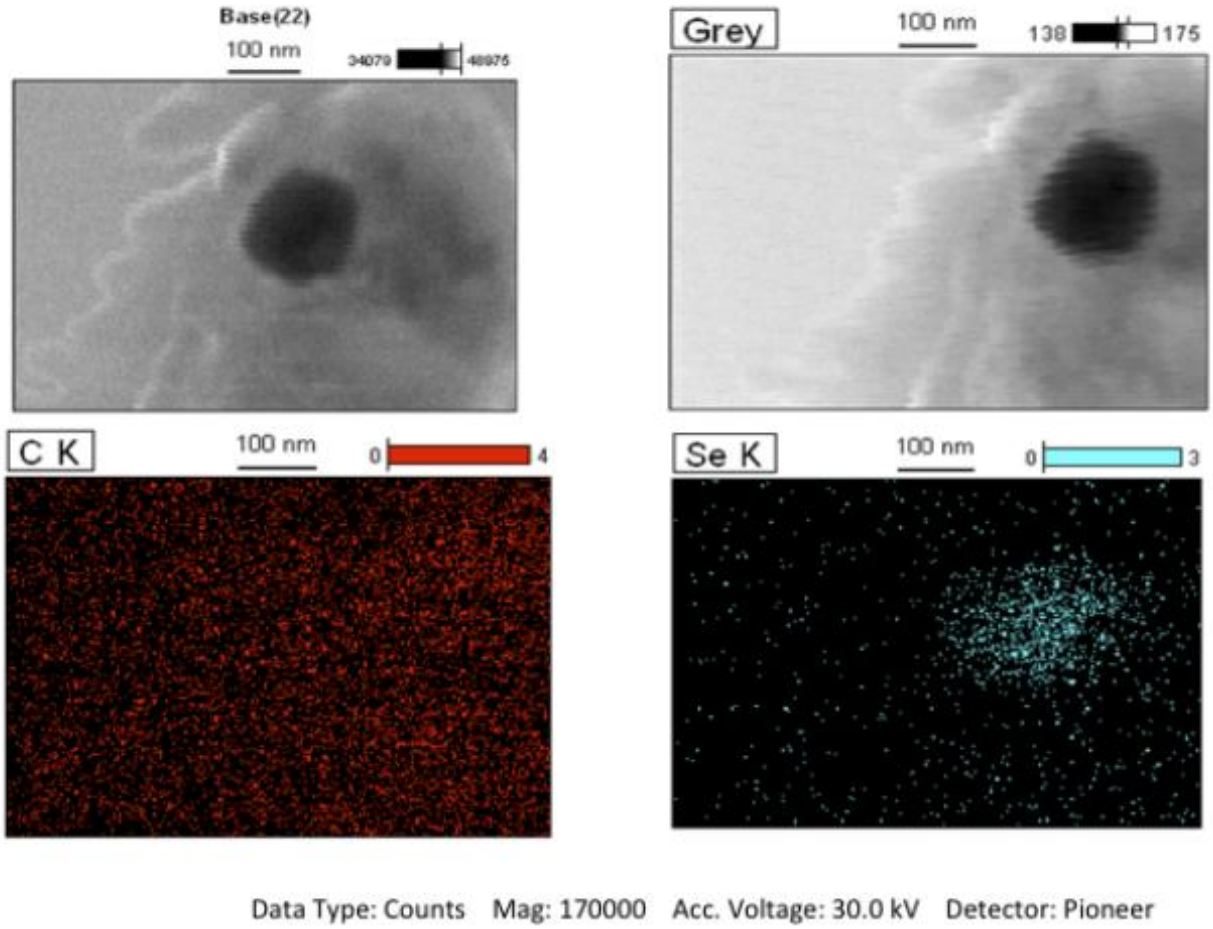

Figure 5.2.1. Raw EDS data taken indicating locations of detected energies of elements. The K edge of chlorine, selenium, and carbon dominates the EDS spectrum. We interpret these images as follows: Carbon localizes throughout the image, due to the carbon support film on which the cells are mounted. Chlorine localizes within the cell boundaries, accounting for physiological saline within the cell. Selenium localizes within the putative SeNP.

5.3 Chapter 4 Supporting Information

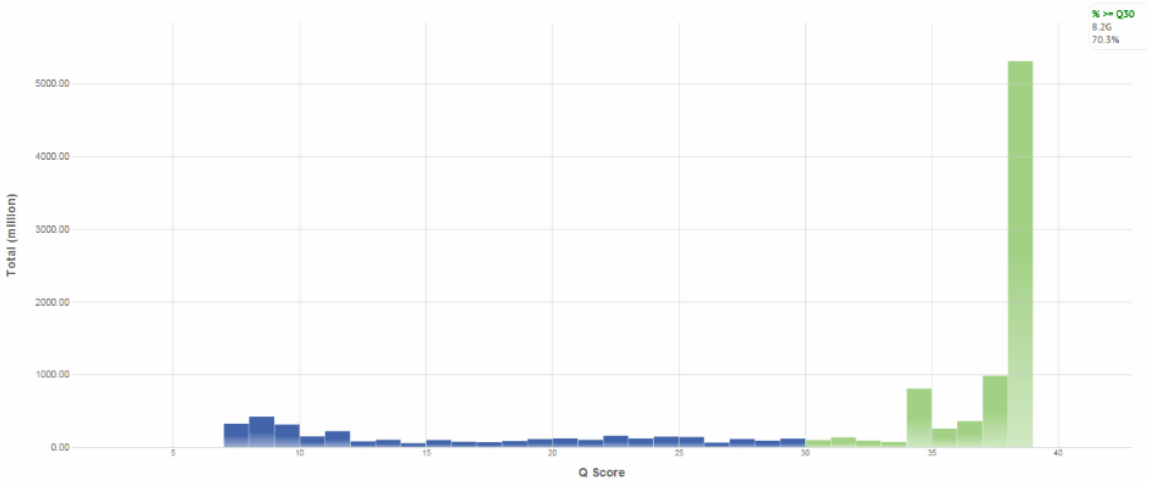

Figure 5.3.1. Phred-like quality scores (Q scores) used to measure the accuracy of the genome sequencing data. Higher Q scores indicate a smaller probability that a base is incorrectly assigned.

DNA Sequence Alignment

Alignment of Pseudo Metalloid Reductase Protein Sequence with Pseudomonas Flourescene GSHR Protein Sequence

Similarity : 442/451 (98.00 %)

```
PM MTLR      -AYDFDLYVIGAGSGGVRAARFAAGFGAKVAVAESRYLGGTCVNVGCVPKKLLVYGAHFA  59
              ||||||||||||||||||||||||||||||||||||||||||||||||||||||||||||
PF GSHR      MAYDFDLYVIGAGSGGVRAARFAAGFGAKVAVAESRYLGGTCVNVGCVPKKLLVYGAHFA  60

PM MTLR      EDFEQASGFGWNLGEANFDWATLIANKDREINRLNGIYRNLLVNSGVTLHEAHAKIVGPH  119
             |||||  ||||||||||:||||||||||||||||||||||||||||||||||||||||||
PF GSHR      EDFEQSSGFGWNLGEADFDWATLIANKDREINRLNGIYRNLLVNSGVTLHEAHAKIVGPH  120

PM MTLR      EVEVNGERFTAKNILIATGGWPQIPGIPGHEHAIGSNEAFFLKELPKRVLVVGGGYIAVE  179
             ||||||||  ||||||||||||||||  ||||||||:||:|||||||||||||||||||||
PF GSHR      EVEVNGERYTAKNILIATGGWPQIPEIPGHEHAISSNQAFFLKELPKRVLVVGGGYIAVE  180

PM MTLR      FAGIFHGLGANTTLLYRGDLFLRGFDGSVRKHLQEELTKRGLDLQFNADIARIDKQADGS  239
             |||||||||||||||||||||||||||||:||:|||||||:|||||||||||||  |||
PF GSHR      FAGIFHGLGANTTLLYRGDLFLRGFDGSVRNHLKEELTKRGMDLQFNADIARIDKQSDGS  240

PM MTLR      LKATLKDGRVLEADCVFYATGRRPMLDNLGLENIDVQLDDKGFIKVDGEYQTTEPSILAL  299
             |||||||||||||||||||||||||||||||||||||||||||||||||| :||||||||||
PF GSHR      LKATLKDGRVLEADCVFYATGRRPMLDNLGLENIDVQLDDKGFIKVDEQYQTTEPSILAL  300

PM MTLR      GDVIGRVQLTPVALAEGMAVARRLFKPEQYRPVDYKMIPTAVFSLPNIGTVGLSEEEARE  359
             |||||||||||||||||||||||||||||||||||||||||||||||||||||||||| ||||||
PF GSHR      GDVIGRVQLTPVALAEGMAVARRLFKPEQYRPVDYKMIPTAVFSLPNIGTVGLTEEEARE  360

PM MTLR      CGHEVVIFESRFRPMKLTLTDCQEKTLMKLVVDARTDKVLGCHMVGPDAGEIVQGLAIAL  419
              ||:|||:|||||||||||||||:|||||||| : |||||||||||||||||||||||||
PF GSHR      AGHDVVIYESRFRPMKLTLTDCQERTLMKLVVDGKSDKVLGCHMVGPDAGEIVQGLAIAL  420

PM MTLR      KAGATKRDFDDTIGVHPTAAEEFVTMRTPVSA  451
```

```
            ||||||||||||||||||||||||||||:|
PF GSHR     KAGATKRDFDDTIGVHPTAAEEFVTMRTPVGA  452
```

Alignment of Pseudo Metalloid Reductase Protein Sequence with E. Coli GSHR Protein Sequence

Similarity : 300/445 (67.42 %)

```
PM MTLR     AYDFDLY-VI-GAGSGGVRAARFAAGFGAKVAVAESRY-LG-GTCVNVGCVPKKLLVYGA  56
             :: | | :| | ::|:::::| |:  :  :::: :::    :::::|: :  :  ::::
EC GSHR     TKHYD-YIAIGGGSGGIASINRAAMYGQKCALIEAKELGGTCVNVGCVPKKVMWHAAQIR  59

PM MTLR     HFAEDFEQASGFGWNLGEANFDWATLIANKDREINRLNGIYRNLLVNSGVTLHEAHAKIV  116
            : : :  :::||:::::: :| ::::  :: ::  :: : ::::  :|::|:  :|::: :
EC GSHR     EAIHMYGPDYGFDTTINKFNWETLIASRTAYIDRIHTSYENVLGKNNVDVIKGFARFVDA  119

PM MTLR     GPHEVEVNGERFTAKNILIATGGWPQIPGIPGHEHAIGSNEAFFLKELPKRVLVVGGGYI  176
            : :|| :: :  ::::|    ::  : ::  :: :: ::::|:: ::: ::| ::| :
EC GSHR     KTLEVNGETITADHILIATGGRPSHPDIPGVEYGIDSDGFFALPALPERVAVVGAGYIAV  179

PM MTLR     AVEFAGIFHGLGANTTLLYRGDLFLRGFDGSVRKHLQEELTKRGLDLQFNADIARIDKQA  236
            ::  ::  :| : :::  :: :|  :::::|: :::    ::::|:   ::: :: ::
EC GSHR     ELAGVINGLGAKTHLFVRKHAPLRSFDPMISETLVEVMNAEGPQLHTNAIPKAVVKNTDG  239

PM MTLR     DGSLKATLKDGRVLEADCVFYATGRRPMLDNLGLENIDVQLDDKGFIKVDGEYQTTEPSI  296
            :: |::: ::::    ::: :  ::: : :||:  : :  :::::  :::: : :: ::
EC GSHR     SLTLELEDGRSETVDCLIWAIGREPANDNINLEAAGVKTNEKGYIVVDKYQNTNIEGIYA  299

PM MTLR     LALGDVIGRVQLTPVALAEGMAVARRLFKPEQYRPVDYKMIPTAVFSLPNIGTVGLSEEE  356
               ::: ::: :  ||   :: ::::  || ::: :::::   :: :::: : : :::
EC GSHR     VGDNTGAVELTPVAVAAGRRLSERLFNNKPDEHLDYSNIPTVVFSHPPIGTVGLTEPQAR  359

PM MTLR     ARECGHEVVIFESRFRPMKLTLTDCQEKTLMKLVVDARTDKVLGCHMVGPDAGEIVQGLA  416
            ::  :::|:   |:|  |:   |:: ::  ||||:: :::|: |:| :|::::| :||:|
EC GSHR     EQYGDDQVKVYKSSFTAMYTAVTTHRQPCRMKLVCVGSEEKIVGIHGIGFGMDEMLQGFA  419

PM MTLR     IALKAGATKRDFDDTIGVHPTAAEEFVTMRTPVSA  451
             |||:||||:|||:|  :|||||||||||
EC GSHR     VALKMGATKKDFDNTVAIHPTAAEEFVTMR-----  449
```

Alignment of Pseudo Metalloid Reductase Protein Sequence with Yeast GSHR Sequence

Similarity : 317/447 (70.92 %)

```
PM MTLR     AYDFDLYVIGAGSGGVRAARFAAGFGAKVAVAESRYLGGTCVNVGCVPKKLLVYGAHFAE  60
             :::|: ||| |||||: ||:||::|||   :| : |||||||||||||:::|  ::|:
SC GSHR     -KHYDYLVIGGGSGGVASARRAASYGAKTLLVEAKALGGTCVNVGCVPKKVMWYASDLAT  59

PM MTLR     DFEQASGFGWNLGEANFDWATLIANKDREINRLNGIYRNLLVNSGVT-LHEAHAKIVGPH  119
            ::::|: :| ::::  :: : |: |:  :: :::  |:::|::   : | |   ::|::
SC GSHR     RVSHANEYGLYQNLPLDKEH-LTFNWPEFKQKRDA-YVHRLNGIYQKNL-EKEKVDVVFG  116

PM MTLR     EVEVNGERFTAKNILIATGGWPQIPGIPGHEHAIGSNEAFFLKELPKRVLVVGGGYIAVE  179
            ::: |::::  : ::::|  ::::: |::::  :   : :::::::: ::::  : :  :
SC GSHR     WARFNKDGNVEVQKRDNTTEVYSANHILVATGGKAIFPENIPGFELGTDSDGFFRLEEQP  176

PM MTLR     FAGIFHGLGANTTLLYRGDLFLRGFDGSVRKHLQEELTKRGLDLQFNADIARIDKQADGS  239
            : ::::|:|    :| :: ::|::::  | : :::::: : : :::  |: :: :::: :
SC GSHR     KKVVVVGAGYIGIELAGVFHGLGSETHLVIRGETVLRKFDECIQNTITDHYVKEGINVHK  236

PM MTLR     LKATLKDGRVLEADCVFYATGRRPMLDNLGLENIDVQLDDKGFIKVDGEYQTTEPSILAL  299
            |:  :|: :::| |  : : ::::::|::::: :: ::::: :::: :: :: ::::: :
SC GSHR     LSKIVKVEKNVETDKLKIHMNDSKSIDDVDELIWTIGRKSHLGMGSENVGIKLNSHDQII  296
```

```
PM MTLR      GDVIGRVQLTPVALAEGMAVARRLFKPEQYRPVDYKMIPTAVFSLPNIGTVGLSEEEARE  359
SC GSHR      ADEYQNTNVPNIYSLGDVVGKVELTPVAIAAGRKLSNRLFGPEKFRNDKLDYENVPSVIF  356

PM MTLR      CGHEVVIFESRFRPMKLTLTDCQEKTLMKLVVDARTDKVLGCHMVGPDAGEIVQGLAIAL  419
SC GSHR      SHPEAGSIGISEKEAIEKYGKENIKVYNSKFTAMYYAMLSEKSPTRYKIVCAGPNEKVVG  416

PM MTLR      KAGATKRDFDDTIGVHPTAAEEFVTMRTPVSA--------------  451
SC GSHR      LHIVGDSSAEILQGFGVAIKMGATKADFDNCVAIHPTSAEELVTMR  462
```

Alignment of Pseudo Metalloid Reductase Protein Sequence with Human GSHR Protein Sequence

Similarity : 313/445 (70.34 %)

```
PM MTLR      --AYDFDLYVI--GAGSGGV--RAARFAAGFGAKVAVA-ESRYL--GGTC-VNVGCVPKK  50
HS GSHR      AVA-SYDYLVIGGGSGGLASARRAAELGARAAVVESHKLGGTCVNVGCVPKKVMWNTAVH  59

PM MTLR      LLVYGAHFAEDFEQASGFGWNLGEANFDWATLIANKDREINRLNGIYRNLLVNSGVTLHE  110
HS GSHR      SEFMHDHADYGFPSCEGKFNWRVIKEKRDAYVSRLNAIYQNNLTKSHIEIIRGHAAFTSD  119

PM MTLR      AHAKIVGPHEVEVNGERF-TAKNI-LI-AT-GGWP-QIPGIPGHEHAIGSNEAFFLK-EL  164
HS GSHR      PKPTIEVSGKKYTAPHILIATGGMPSTPHESQIPGASLGITSDGFFQLEELPGRSVIVGA  179

PM MTLR      PK-RVLVVGGGYIAVEFAGIFHGLGANTTLLYRGDLFLRGFDGSVRKHLQEELTKRGLDL  223
HS GSHR      GYIAVEMAGILSALGSKTSLMIRHDKVLRSFDSMISTNCTEELENAGVEVLKFSQVKEVK  239

PM MTLR      QFNADIARIDKQADGSLKATLKDGRVLEADCVFYATGRRPMLDNLGLENIDVQLDDKGFI  283
HS GSHR      KTLSGLEVSMVTAVPGRLPVMTMIPDVDCLLWAIGRVPNTKDLSLNKLGIQTDDKGHIIV  299

PM MTLR      KVDGEYQTTEPSILALGDVIGRVQLTPVALAEGMAVARRLFKPEQYRPVDYKMIPTAVFS  343
HS GSHR      DEFQNTNVKGIYAVGDVCGKALLTPVAIAAGRKLAHRLFEYKEDSKLDYNNIPTVVFSHP  359

PM MTLR      LPNIGTVGLSEEEARECGHEVVIFESRFRPMKLTLTDCQEKTLMKLVVDARTDKVLGCHM  403
HS GSHR      PIGTVGLTEDEAIHKYGIENVKTYSTSFTPMYHAVTKRKTKCVMKMVCANKEEKVVGIHM  419

PM MTLR      VGPDAGEIVQGLAIALKAGATKRDFDDTIGVHPTAAEEFVTMRTPVSA  451
HS GSHR      QGLGCDEMLQGFAVAVKMGATKADFDNTVAIHPTSSEELVTLR-----  462
```

Alignment of Pseudomonas Flourescene GSHR Protein Sequence with E. Coli GSHR Protein Sequence

Similarity : 304/445 (68.31 %)

```
PF GSHR      MAYDFDLY-VI-GAGSGGVRAARFAAGFGAKVAVAESRY-LG-GTCVNVGCVPKKLLVYG  56
EC GSHR      -TKHYD-YIAIGGGSGGIASINRAAMYGQKCALIEAKELGGTCVNVGCVPKKVMWHAAQI  58

PF GSHR      AHFAEDFEQSSGFGWNLGEADFDWATLIANKDREINRLNGIYRNLLVNSGVTLHEAHAKI  116
EC GSHR      REAIHMYGPDYGFDTTINKFNWETLIASRTAYIDRIHTSYENVLGKNNVDVIKGFARFVD  118

PF GSHR      VGPHEVEVNGERYTAKNILIATGGWPQIPEIPGHEHAISSNQAFFLKELPKRVLVVGGGY  176
```

```
            :: :|| :: :  ::::|    ::  : ::  :: :: ::::|:: ::: ::| ::| :
EC GSHR     AKTLEVNGETITADHILIATGGRPSHPDIPGVEYGIDSDGFFALPALPERVAVVGAGYIA  178

PF GSHR     IAVEFAGIFHGLGANTTLLYRGDLFLRGFDGSVRNHLKEELTKRGMDLQFNADIARIDKQ  236
             ::  ::  :| : :::  :: :|  :::::|: ::::   ::::::   ::: :: ::
EC GSHR     VELAGVINGLGAKTHLFVRKHAPLRSFDPMISETLVEVMNAEGPQLHTNAIPKAVVKNTD  238

PF GSHR     SDGSLKATLKDGRVLEADCVFYATGRRPMLDNLGLENIDVQLDDKGFIKVDEQYQTTEPS  296
            ::: |::: ::::    ::: :  ::: : :||:  : :  :::::  :::: : :: ::
EC GSHR     GSLTLELEDGRSETVDCLIWAIGREPANDNINLEAAGVKTNEKGYIVVDKYQNTNIEGIY  298

PF GSHR     ILALGDVIGRVQLTPVALAEGMAVARRLFKPEQYRPVDYKMIPTAVFSLPNIGTVGLTEE  356
                ::: ::: :  ||   :: ::::  || ::: :::::   :: :::: : : :::
EC GSHR     AVGDNTGAVELTPVAVAAGRRLSERLFNNKPDEHLDYSNIPTVVFSHPPIGTVGLTEPQA  358

PF GSHR     EAREAGHDVVIYESRFRPMKLTLTDCQERTLMKLVVDGKSDKVLGCHMVGPDAGEIVQGL  416
             ::  :::|: | |:|  |:   |:: ::  ||||::|:::|: |:| :|::::| :|||:
EC GSHR     REQYGDDQVKVYKSSFTAMYTAVTTHRQPCRMKLVCVGSEEKIVGIHGIGFGMDEMLQGF  418

PF GSHR     AIALKAGATKRDFDDTIGVHPTAAEEFVTMRTPVGA  452
            | |||:||||:|||:|  :||||||||||||
EC GSHR     AVALKMGATKKDFDNTVAIHPTAAEEFVTMR-----  449
```

Alignment of Pseudomonas Flourescene GSHR Protein Sequence with Yeast GSHR Sequence

Similarity : 327/445 (73.48 %)

```
PF GSHR     MAYDFDLYVI--GAGSG-GV-RAARFAAGFG-AKVAVAESRYL-GGT-C-VNVGCVPKKL  52
              :::|: ||  | |:: :: |||:: |::  : : : :: :: :|    ::: :::: :
SC GSHR     --KHYDYLVIGGGSGGVASARRAASYGAKTLLVEAKALGGTCVNVGCVPKKVMWYASDLA  58

PF GSHR     LVYGAHFAEDFEQSSGFGWNLGEADFDWATLIANKDREI-NRLNGIYRNLLVNSGVTLHE  111
            ::::::: ::::|:  ::: : : ::   ::::: :::: |::: ::  ::::::| :::
SC GSHR     TRVSHANEYGLYQNLPLDKEHLTFNWPEFKQKRDAYVHRLNGIYQKNLEKEKVDVVFGWA  118

PF GSHR     AHAKIVGPHEVEV-N-GERYTAKNI-LIA-TGGW-PQIPEIPGHEHAISSNQAFF-LKEL  165
            : :|:::: : :: |  |:| |::| ::   :   |:::::  :::::: :::: : ::
SC GSHR     RFNKDGNVEVQKRDNTTEVYSANHILVATGGKAIFPENIPGFELGTDSDGFFRLEEQPKK  178

PF GSHR     PKRVLVVGGGYIAVEFAGIFHGLGANTTLLYRGDLFLRGFDGSVRNHLKEELTKRGMDLQ  225
            :::|:::  | : :::  :: :: :   ::  : :::: :  :  :::::::  ::::|:
SC GSHR     VVVVGAGYIGIELAGVFHGLGSETHLVIRGETVLRKFDECIQNTITDHYVKEGINVHKLS  238

PF GSHR     FNADIARIDKQSDGSLKATLKDGRVLEADCVFYATGRRPMLDNLGLENIDVQLDDKGFIK  285
            : ::: ::: ::: ::::::::: ::::   ::  :::: :::: :::|: :::|  :::
SC GSHR     KIVKVEKNVETDKLKIHMNDSKSIDDVDELIWTIGRKSHLGMGSENVGIKLNSHDQIIAD  298

PF GSHR     VDEQYQTTEP-SILAL-GDVIGRVQLTPVALAEGMAVARRLFKPEQYRPVDYKMIPTAVF  343
             :::::  :: |:::: |:|:   :: :: : ::::  : :: :::: :: :: ::  ::
SC GSHR     EYQNTNVPNIYSLGDVVGKVELTPVAIAAGRKLSNRLFGPEKFRNDKLDYENVPSVIFSH  358

PF GSHR     SLPNIGTVGLTEEEAREAGHDVVIYESRFRPMKLTLTDCQERTLMKLVVDGKSDKVLGCH  403
             ::::   :::|:: :: : : ::|:|:| :|:: : : :: |::|:|::| : ||:| |
SC GSHR     PEAGSIGISEKEAIEKYGKENIKVYNSKFTAMYYAMLSEKSPTRYKIVCAGPNEKVVGLH  418

PF GSHR     MVGPDAGEIVQGLAIALKAGATKRDFDDTIGVHPTAAEEFVTMRTPVGA  452
             ||::  || ||: :|:|:||||:|||: :  ||| |||:||||
SC GSHR     IVGDSSAEILQGFGVAIKMGATKADFDNCVAIHPTSAEELVTMR-----  462
```

Alignment of Pseudomonas Flourescene GSHR Protein Sequence with Human GSHR Protein Sequence

Similarity : 315/446 (70.63 %)

```
PF GSHR      -MAYDFDLYVI--GAGSGGV--RAARFAAGFGAKVAVA-ESRYL--GGTC-VNVGCVPKK  51
HS GSHR      AVA-SYDYLVIGGGSGGLASARRAAELGARAAVVESHKLGGTCVNVGCVPKKVMWNTAVH  59

PF GSHR      LLVYGAHFAEDFEQSSGFGWNLGEADFDWATLIANKDREINRLNGIYRNLLVNSGVTLHE  111
HS GSHR      SEFMHDHADYGFPSCEGKFNWRVIKEKRDAYVSRLNAIYQNNLTKSHIEIIRGHAAFTSD  119

PF GSHR      AHAKIVGPHEVEVNGER-YTAKN-IL-IA-TG-GWP-QIPEIPGHEHAISSNQAFF-LKE  164
HS GSHR      PKPTIEVSGKKYTAPHILIATGGMPSTPHESQIPGASLGITSDGFFQLEELPGRSVIVGA  179

PF GSHR      LPKRVLVVGGGYIAVEFAGIFHGLGANTTLLYRGDLFLRGFDGSVRNHLKEELTKRGMDL  224
HS GSHR      GYIAVEMAGILSALGSKTSLMIRHDKVLRSFDSMISTNCTEELENAGVEVLKFSQVKEVK  239

PF GSHR      QFNADIARIDKQSDGSLKATLKDGRVLEADCVFYATGRRPMLDNLGLENIDVQLDDKGFI  284
HS GSHR      KTLSGLEVSMVTAVPGRLPVMTMIPDVDCLLWAIGRVPNTKDLSLNKLGIQTDDKGHIIV  299

PF GSHR      KVDEQYQTTEPSILALGDVIGRVQLTPVALAEGMAVARRLFKPEQYRPVDYKMIPTAVFS  344
HS GSHR      DEFQNTNVKGIYAVGDVCGKALLTPVAIAAGRKLAHRLFEYKEDSKLDYNNIPTVVFSHP  359

PF GSHR      LPNIGTVGLTEEEAREAGHDVVIYESRFRPMKLTLTDCQERTLMKLVVDGKSDKVLGCHM  404
HS GSHR      PIGTVGLTEDEAIHKYGIENVKTYSTSFTPMYHAVTKRKTKCVMKMVCANKEEKVVGIHM  419

PF GSHR      VGPDAGEIVQGLAIALKAGATKRDFDDTIGVHPTAAEEFVTMRTPVGA  452
HS GSHR      QGLGCDEMLQGFAVAVKMGATKADFDNTVAIHPTSSEELVTLR-----  462
```

Alignment of E. Coli GSHR Protein Sequence with Yeast GSHR Sequence

Similarity : 332/445 (74.61 %)

```
EC GSHR      TKHYDYIAIGGGSGGIASINRAAMYGQKCALIEAKELGGTCVNVGCVPKKVMW-------  53
SC GSHR      -KHYDYLVIGGGSGGVASARRAASYGAKTLLVEAKALGGTCVNVGCVPKKVMWYASDLAT  59

EC GSHR      -----HAAQIREAIHMYGPDYGFDTTINKFNWETLIASRTAYIDRIHTSYENVLGKNNVD  108
SC GSHR      RVSHANEYGLYQNLPLDKEHLTF-NWPEFKQKRDAYVHRLNGIYQKNLEKEKVD-VVFGW  117

EC GSHR      VIKGFARFVDAKTLEVN-GETITADH-ILIA-TG-GRPSHPDIP-GVEYGIDSDGFFALP  163
SC GSHR      ARFNKDGNV-EVQKRDNTTEVYSANHILVATGGKAIFPENIPGFELGTDSDGFFRLEEQP  176

EC GSHR      ALPERVAVVGAGYIAVELAGVINGLGAKTHLFVRKHAPLRSFDPMISETLVEVMNAEGPQ  223
SC GSHR      KKVVVVGAGYIGIELAGVFHGLGSETHLVIRGETVLRKFDECIQNTITDHYVKEGINVHK  236

EC GSHR      LHTNAIPKAVVKNTDGSLTLELEDGRSETVDCLIWAIGREPANDNINLEAAGVKTNEKGY  283
SC GSHR      LSKIVKVEKNVETDKLKIHMNDSKSIDDVDELIWTIGRKSHLGMGSENVGIKLNSHDQII  296

EC GSHR      IVVDKYQNTNIEGIYAVGDNTGAVELTPVAVAAGRRLSERLFNNKPDEHLDYSNIPTVVF  343
```

```
SC GSHR      ADEYQNTNVPNIYSLGDVVGKVELTPVAIAAGRKLSNRLFGPEKFRNDKLDYENVPSVIF  356

EC GSHR      SHPPIGTVGLTEPQAREQYGDDQVKVYKSSFTAMYTAVTTHRQPCRMKLVCVGSEEKIVG  403
             |||::|  |: |::| |:|||: : |||:|:|||||:|:   ::| |:|:|||:| :|||:||
SC GSHR      SHPEAGSIGISEKEAIEKYGKENIKVYNSKFTAMYYAMLSEKSPTRYKIVCAGPNEKVVG  416

EC GSHR      IHGIGFGMDEMLQGFAVALKMGATKKDFDNTVAIHPTAAEEFVTMR  449
             :| :|:::::| |||| ||:|||||| |||| |||||| |||:||||
SC GSHR      LHIVGDSSAEILQGFGVAIKMGATKADFDNCVAIHPTSAEELVTMR  462
```

Alignment of E. Coli GSHR Protein Sequence with Human GSHR Protein Sequence

Similarity : 353/447 (78.97 %)

```
EC GSHR      -TKHYDYIAIGGGSGGIASINRAAMYGQKCALIEAKELGGTCVNVGCVPKKVMW-HAAQI  58
                :|||::|||||||:||::|||  |:: |::| ::|||||||||||||||||| : |::
HS GSHR      AVASYDYLVIGGGSGGLASARRAAELGARAAVVESHKLGGTCVNVGCVPKKVMWNT-AVH  59

EC GSHR      REAIHMYGPDYGFDTTIN-KFNWETLIASRTAYIDRIHTSYENVLGKNNVDVIK-GFARF  116
             :| :::: :||||   ::  :::: :: ::  ::: :: : :| ::::    ::  :  :
HS GSHR      SE-FMHDHADYGFPSCEGKFNWRVIKEKRDAYVSRLNAIYQNNLTKSHIEIIRGHAAFTS  118

EC GSHR      VDA-KTLE-VNGETITAD-HI-LI-A-TGGRP-SHPDI-PGVEYG-IDSD--GFFALPAL  165
             :   : :: ::::|: :   : ::   |   :   ::: :  ::| :      :: ::::
HS GSHR      DPKPTIEVSGKKYTAPHILIATGGMPSTPHESQIPGASLGITSDGFFQLEELPGRSVIVG  178

EC GSHR      PERVAVVGAGYIAVELAGVINGLGAKTHLFVRKHAPLRSFDPMISETLVEVMNAEGPQLH  225
             ::  ||  || : ::: : :  ::::::|:: ::::: :::: : : :||| : : ::::
HS GSHR      AGYIAVEMAGILSALGSKTSLMIRHDKVLRSFDSMISTNCTEELENAGVEVLKFSQVKEV  238

EC GSHR      TNAIPKAVVKNTDGSLTLELEDGRSETVDCLIWAIGREPANDNINLEAAGVKTNEKGYIV  285
             :: :::  |:: : :: ::::: : ::||||:|||||:|::::::|:  |  |::||:|
HS GSHR      KKTLSGLEVSMVTAVPGRLPVMTMIPDVDCLLWAIGRVPNTKDLSLNKLGIQTDDKGHII  298

EC GSHR      VDKYQNTNIEGIYAVGDNTGAVELTPVAVAAGRRLSERLFNNKPDEHLDYSNIPTVVFSH  345
             ||  ||||::|||||||: | ::|||||  ||||:| :||| :|:|::|||:|||||||||
HS GSHR      VDEFQNTNVKGIYAVGDVCGKALLTPVAIAAGRKLAHRLFEYKEDSKLDYNNIPTVVFSH  358

EC GSHR      PPIGTVGLTEPQAREQYGDDQVKVYKSSFTAMYTAVTTHRQPCRMKLVCVGSEEKIVGIH  405
             ||||||||||::| ::||  :|| |: ||| ||:|||:::::|:||:||:::|||:||||
HS GSHR      PPIGTVGLTEDEAIHKYGIENVKTYSTSFTPMYHAVTKRKTKCVMKMVCANKEEKVVGIH  418

EC GSHR      GIGFGMDEMLQGFAVALKMGATKKDFDNTVAIHPTAAEEFVTMR  449
              :|:|:||||||||||:|||||| ||||||||||  ||:|| |
HS GSHR      MQGLGCDEMLQGFAVAVKMGATKADFDNTVAIHPTSSEELVTLR  462
```

Alignment of Yeast GSHR Sequence with Human GSHR Protein Sequence

Similarity : 344/454 (75.77 %)

```
SC GSHR      --KHYDYLVIGGGSGGVASARRAASYGAKTLLVEAKALGGTCVNVGCVPKKVMWYASDLA  58
                :|||||||||||| |||||||  ||: ::|| : |||||||||||||||||     :
HS GSHR      AVASYDYLVIGGGSGGLASARRAAELGARAAVVESHKLGGTCVNVGCVPKKVMW-----N  55

SC GSHR      TRV-S-HANEYGLYQNLPLDKEHLTFNWPEFKQKRDAYVHRLNGIYQKNLEKEKVDVVFG  116
             |:| | ::: :  | ::| : |  :|||  :|:|||||||||| |||:|| | ::::: |
HS GSHR      TAVHSEFMHDHADY-GFP-SCE-GKFNWRVIKEKRDAYVSRLNAIYQNNLTKSHIEIIRG  112

SC GSHR      WARFNKDGNVEVQKRDNTTEVYSANHILVATGGKAIF-PENI-PGFEL-GTDSD-GFFRL  172
             :|:|::|::: :::::::: :::::  :  :::: : :::   : :  : ::: ::::
HS GSHR      HAAFTSDPKPTIEVSGKKYTAPHILIATGGMPSTPHESQIPGASLGITSDGFFQLEELPG  172
```

```
SC GSHR      EEQPKKVVVVGAGYIGIELAGVFHGLGSETHLVIRGETVLRKFDECIQNTITDHYVKEGI  232
                ::::::: ::: ||: |:: :  ::: | : :: :: :: : | :::::: ::::::
HS GSHR      RSVIVGAGYIAVEMAGILSALGSKTSLMIRHDKVLRSFDSMISTNCTEELENAGVEVLKF  232

SC GSHR      NVHKLSKIVKVEKNVETDKLKIHMNDSKSIDDVDELIWTIGRKSHLGMGSENVGIKLNSH  292
             :::|::|  :: ::|  :: :: ::::   ::::  ::: :::::   :: :::::::  :
HS GSHR      SQVKEVKKTLSGLEVSMVTAVPGRLPVMTMIPDVDCLLWAIGRVPNTKDLSLNKLGIQTD  292

SC GSHR      DQIIADEYQNTNVPNIYSLGDVVGKVELTPVAIAAGRKLSNRLFGPEKFRNDKLDYENVP  352
             |   :: ::::|  :  :  :::: :  :: : |: :: :::  ::|: :::|||| |:|
HS GSHR      DKGHIIVDEFQNTNVKGIYAVGDVCGKALLTPVAIAAGRKLAHRLFEYKEDSKLDYNNIP  352

SC GSHR      SVIFSHPEAGSIGISEKEAIEKYGKENIKVYNSKFTAMYYAMLSEKSPTRYKIVCAGPNE  412
              | ||||::|  |: |:||| |||:|| | |: :||:||:|: : |   ::| |||: :|
HS GSHR      TVVFSHPPIGTVGLTEDEAIHKYGIENVKTYSTSFTPMYHAVTKRKTKCVMKMVCANKEE  412

SC GSHR      KVVGLHIVGDSSAEILQGFGVAIKMGATKADFDNCVAIHPTSAEELVTMR  462
             ||||:| :|::::| |||| || |||||||||| ||||||| |||||:|
HS GSHR      KVVGIHMQGLGCDEMLQGFAVAVKMGATKADFDNTVAIHPTSSEELVTLR  462
```

Table 5.3.1. Templates used for model generation of GRLMR with homology ranking.

Homology	PDB	Enzyme	Organism
1	4DNA	Putative Glutathione Reductase	*Sinorhizobium meliloti* 1021
2	5V36	Glutathione Reductase	*Streptococcus mutans* UA159
3	2R9Z	Glutathione Amide Reductase	*Chromatium gracile*
4	3O0H	Glutathione Reductase	*Bartonella henselsea*
5	1GEU	Glutathione Reductase (Engineered NAD Site)	*Escherichia coli*
6	6B4O	Glutathione Reductase	*Enterococcus faecalis*
7	5W1J	Thioredoxin Glutathione Reductase	*Echinococcus granulosus*
8	1TYT	Trypanothione Reductase	*Crithidia fasciculata*
9	1BWC	Glutathione Reductase	*Homo sapiens*
10	2W0H	Trypanothione Reductase	*Leishmania infantum*
11	1EBD	Dihydrolipoamide Dehydrogenase	*Geobacillus stearotherophilus*
12	2EQ8	Lipoamide Dehydrogenase	*Thermus thermophilus*
13	2V6O	Thioredoxin Glutathione Reductase	*Schistosoma mansoni*
14	1NDA	Trypanothione Reductase	*Trypanosoma cruzi*
15	1OJT	Dihyrolipoamide Dehydrogenase	*Neisseria meningitidis*
16	2EQ7	Lipoamide Dehydrogenase	*Thermus thermophilus*

17	2A8X	Lipoamide Dehydrogenase	*Mycobacterium tuberculosis*
18	1XDI	Unknown	*Mycobacterium tuberculosis*
19	5X1Y	Mercuric Reductase	*Lysinibacillus sphaericus*
20	1LVL	Lipoamide Dehydrogenase	*Pseudomonas putida*

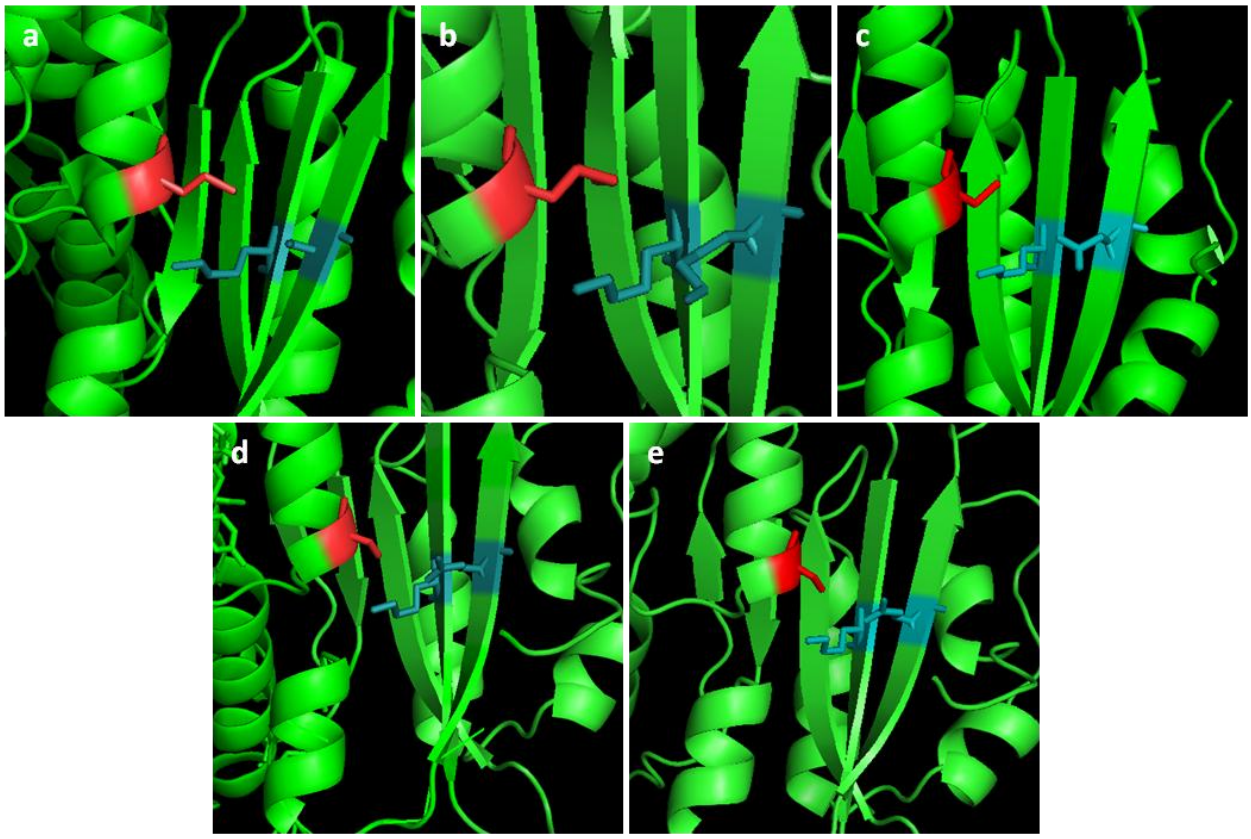

Figure 5.3.2. Product binding pocket for various GSHR's with key residues highlighted. a: *H. sapiens* (Red- Methionine, Right Teal- Serine, Left Teal- Lysine) b: *E. Coli* (Red- Methionine, Right Teal- Lysine, Left Teal- Lysine) c: *S. Cervisiae* (Red- Cysteine, Right Teal- Asparagine, Left Teal- Lysine) d: *P. fluorescines* (Red- Serine, Right Teal- Glutamic Acid, Left Teal- Lysine) e: GRLMR (Red- Serine, Right Teal- Glutamic Acid, Left Teal- Lysine).

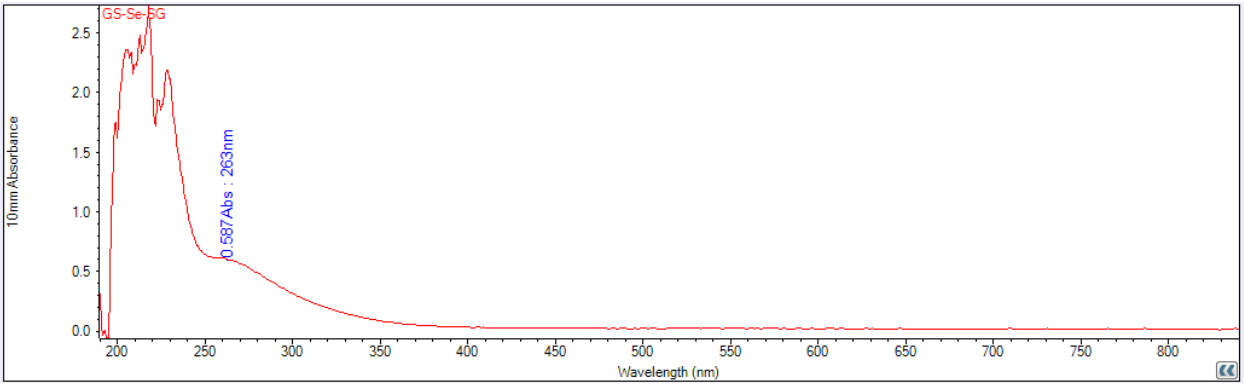

Figure 5.3.3. GS-Se-SG EV-Vis Spectra

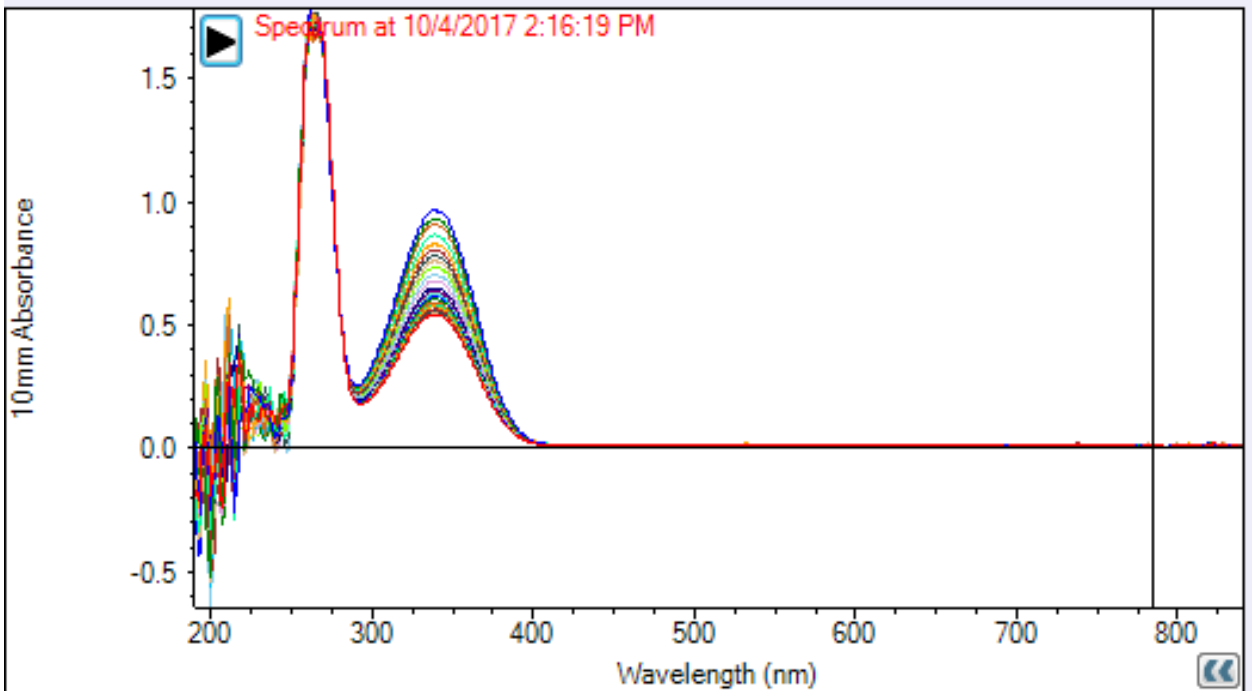

Figure 5.3.4. NADPH peak depletion (340nm) during a GSSG enzyme reduction assay.

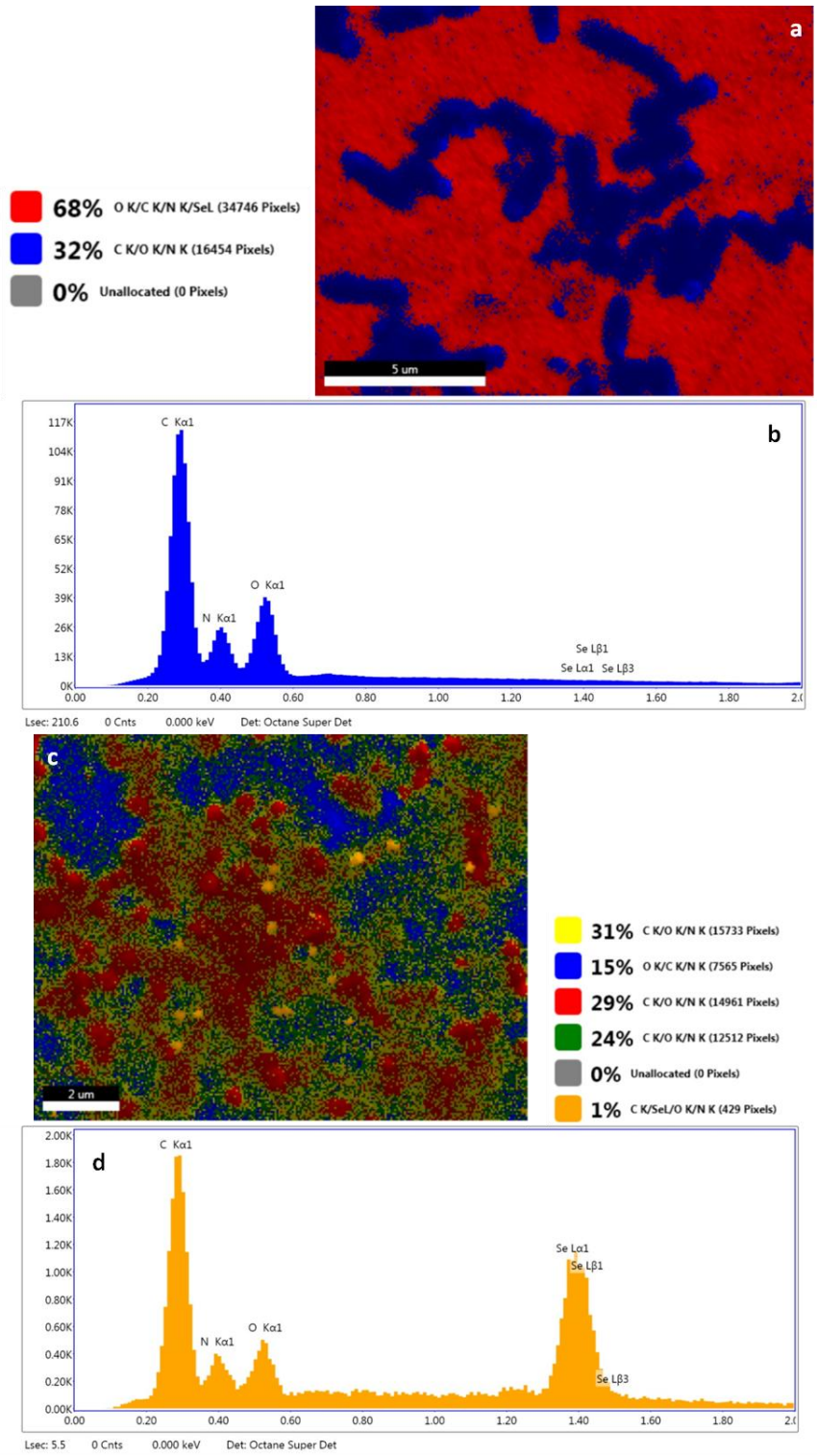

Figure 5.3.5 SEM/EDS overlay of cells exposed to 5mM selenite for 3 hours. a: BL21 *E. Coli* with a GFP reporter plasmid. b: Reporter plasmid cells EDS spectra associated with cells. c: BL21 *E. Coli* containing the GRLMR gene. d: EDS spectra of particles associated with the GRLMR cells.

REFERENCES

1. Kowalski, A.E. *et al*. *Nanoscale.* **2016,** *8*, 12693-12696.

2. Studier, F.W. *Protein Expr. Purif.* **2005,** *41*, 207–234.

3. Stezeryanskii, E., Vyunov, O., Omelchuk, A. *J. Sol. Chem.* **2015,** *44*, 1749-1755.

4. Drier, T., Compel, W., Wong, A., Ackerson, C. *J. Phys. Chem. C.* **2016,** *120*, 28288-28294.

5. Heinecke, C.L. *et al. J. Am. Chem. Soc.* **2012,** *134*, 13316–13322.

6. Gao, C., Zhang, Q., Zhenda, L., Yin, Y. *J. Am. Chem. Soc.* **2011,** *133*, 19706-19709.

7. Zhai, Y., *et. al. Nat. Mater.* **2016,** *15*, 889-895.

8. Huang, J., *et al. Optik.* **2016,** *127*, 10343-10347

9. Zou, R., *et al. Col. Surf. A. Physicochem. Eng. Aspects.* **2010,** *372*, 177-181.

10. Drier, T., Ackerson, C. *Angew. Chem. Int. Ed. Engl.* **2015,** *54*, 9429-9252.

11. Kang, B. *Methods Cell Biol.* **2010,** *96*, 259.

12. Juers, D.H. & Ruffin, J. *J. Appl. Cryst.* **2014,** *47*, 2105-2108.

13. Hunter, W. J. & Manter, D. K. *Curr. Microbiol.* **2008,** *57*, 83-88.

14. Galloway, J.M. & Staniland, S. S. *J. Mater. Chem.* **2012,** *22*, 12423-12434.

15. McDonald, K. L. & Webb, R. I. *Journal of Microscopy.* **2011,** *243*, 227-233.

16. Mastronarde, D. N. *J. Struct. Biol.* **2005,** *152*, 36-51.

17. Kremer, J. R., Mastronarde, D. N., McIntosh, J. R. *J. Struct. Biol.* **1996,** *116*, 71-76.

18. Hunter, W. J. *Curr. Microbiol.* **2014,** *69*, 69-74.

19. Saveliev, S. V., *et. al. Anal. Chem.* **2013,** *85*, 907-914.